Charge carriers in semiconductors:
Loose, confined, trapped

Charge carriers in semiconductors:
Loose, confined, trapped

ACADEMISCH PROEFSCHRIFT

ter verkrijging van de graad van doctor
aan de Universiteit van Amsterdam
op gezag van de Rector Magnificus
prof. dr. D. C. van den Boom
ten overstaan van een door het college voor promoties
ingestelde commissie,
in het openbaar te verdedigen in de Agnietenkapel
op vrijdag 29 juni 2012, te 16:00 uur

door

Ronald Ulbricht

geboren te Löbau, Duitsland

PROMOTIECOMMISSIE

promotor: prof. dr. M. Bonn
overige leden: prof. dr. H. J. Bakker
prof. dr. D. Vanmaekelbergh
prof. dr. T. Gregorkiewicz
prof. dr. P. U. Jepsen
dr. R.U.A. Khan

Faculteit der Natuurwetenschappen, Wiskunde en Informatica

ISBN **9789077209639**

The work described in this thesis was performed at the FOM Institute AMOLF, Science Park 104, 1098 XG Amsterdam, The Netherlands. This work is part of the research programme of the *Stichting Fundamenteel Onderzoek der Materie* (FOM), which is financially supported by the *Nederlandse Organisatie voor Wetenschappelijk Onderzoek* (NWO). Part of this work has been financially supported by the European Union - Marie Curie program (MEST-CT-2005-021000).

PUBLICATIONS COVERED IN THIS THESIS

R. Ulbricht, E. Hendry, J. Shan, T. F. Heinz and M. Bonn. Carrier dynamics in semiconductors studied with time-resolved terahertz spectroscopy. *Reviews of Modern Physics* 83(2): 543, 2011.

R. Ulbricht, S. T. van der Post, J. P. Goss, P. R. Briddon, R. Jones, R. U. A. Khan and M. Bonn. Single substitutional nitrogen defects revealed as electron acceptor states in diamond using ultrafast spectroscopy. *Phys. Rev. B* 84(16), 2011.

R. Ulbricht, R. Kurstjens and M. Bonn. Assessing charge carrier trapping in silicon nanowires using picosecond conductivity measurements. *Nano Letters (accepted)*.

R. Ulbricht, J. J. H. Pijpers, E. Groeneveld, R. Koole, C. M. Donega, D. Vanmaekelbergh, C. Delerue, G. Allan and M. Bonn. Loosening quantum confinement: Observation of real conductivity in semiconductor nanoparticles smaller than the Bohr radius. *Submitted*.

R. Ulbricht, R. Kurstjens, G. Grzela, J. Gomez Rivas and M. Bonn. Anisotropic absorption coefficients of silicon nanowire arrays. *In preparation*.

OTHER PUBLICATIONS

J. J. H. Pijpers, R. Ulbricht, K. J. Tielrooij, A. Osherov, Y. Golan, C. Delerue, G. Allan, and M. Bonn. Assessment of carrier-multiplication efficiency in bulk PbSe and PbS. *Nature Physics* 5(11), 811, 2009.

A. Berrier, R. Ulbricht, M. Bonn, and J. G. Rivas. Ultrafast active control of localized surface plasmon resonances in silicon bowtie antennas. *Optics Express* 18(22), 23226, 2010.

J. J. H. Pijpers, R. Ulbricht, S. Derossi, J. N. H. Reek, and M. Bonn. Picosecond Electron Injection Dynamics in Dye-Sensitized Oxides in the Presence of Electrolyte. *J. Phys. Chem. C* 115(5), 2578, 2011.

A. Berrier, P. Albella, M. A. Poyli, R. Ulbricht, M. Bonn, J. Aizpurua, and J. G. Rivas. Detection of deep-subwavelength dielectric layers at terahertz frequencies using semiconductor plasmonic resonators. *Optics Express* 20(5), 5052, 2012

Contents

1

Terahertz spectroscopy on semiconductors

Time-resolved terahertz spectroscopy is the main measurement technique used in this thesis. This introductory chapter will treat its application to semiconducting materials. It starts with a general overview of experimental methods to generate and detect terahertz radiation, including a description of the specific setups that are in use in our laboratory. It is followed by a section that covers analytical procedures to extract the terahertz spectra from samples employing common material geometries. The last section introduces characteristic terahertz responses of certain material systems and their physical interpretations, seasoned with selected references to previous works.

1.1 Introduction

Charge carriers in semiconductors provide the basis for a variety of important technologies, including computers, semiconductor lasers and light emitting devices. The continuing wish to reduce the physical size of next-generation electronic devices requires increasingly smaller building blocks in electronics. Nanostructures with sizes well below 100 nm, such as semiconductor nanocrystals and nanowires, provide such building blocks. Hence, it is apparent that there is both a technological and fundamental interest in the properties of charge carriers in both bulk and nanostructured materials.

Charge carriers can have very different properties in semiconductors and semiconductor nanostructures, depending on morphology, temperature and material properties such as the crystal structure, bandgap, dielectric function and electron-phonon coupling strength. In a bulk material with high dielectric function, but moderate electron-phonon coupling, charge carriers are efficiently screened from one another, and electrons and holes will be present as free carriers and relatively mobile. For materials with strong electron-phonon coupling, these carrier-lattice interactions will lead to the formation of polarons, carriers that are dressed with local lattice deformations. Polarons have a reduced mobility due to their increased effective mass. For materials with reduced dielectric function, screening is relatively weak and bound electron-hole pairs, excitons, may be formed, which can be thermally dissociated at elevated temperatures.

Regarding the role of morphology of the material on the nature of the charge carriers, one can distinguish several regimes. Consider a material for which in the bulk electrons are present as free carriers. For sufficiently small nanostructures, i.e. of dimension R appreciably smaller than the exciton Bohr radius, strong confinement of carriers occurs. In this limit, the effective bandgap of the material is increased due to the confinement energy and discrete instead of continuous intraband energy levels are present.

The common characteristic of charge carriers, which may be present in any of the different forms described above, is that they all exhibit a distinct response in the low-frequency range of the electromagnetic spectrum: Exciton binding energies - and exciton transitions, for both bulk and nanostructured materials, are typically in the meV range and are optically active; The response of mobile carriers and polarons is dictated by carrier-phonon interactions leading to randomization of the carrier momentum typically occurring on (sub-)picosecond time scales, giving rise to dispersion in the dielectric response on meV energy scales. The dielectric response in the same energy range is modified for carriers which undergo a different type of transport (hopping transport or transport in non-crystalline semiconductors). The ability to probe charge carriers in the meV energy or, equivalently, terahertz frequency range, therefore allows their detailed characterization through the distinct spectral signatures in the terahertz range [206, 107, 67]. THz spectroscopy constitutes a contact-free probe of the frequency-dependent conductivity, which is determined by key parameters such as the carrier density and mobility.

THz time-domain spectroscopy (THz TDS) makes use of sub-picosecond pulses of freely propagating electromagnetic radiation in the terahertz range. THz radiation (1 THz = 10^{12} Hz) is characterized by sub-mm wavelengths (300 μm for 1 THz in vacuum), low photon energies (33.3 cm^{-1} or 4.2 meV at 1 THz), corresponding to less-than-thermal energies at room temperature (1 THz corresponds to 48 K). THz pulses are readily generated by frequency down-conversion of femtosecond optical pulses to the THz range and detected coherently in the time-domain (see next Section). This brings some important advantages compared to traditional far-infrared cw spectroscopy techniques that were commonly used before (see, e.g. [13, 96]. By sampling the instantaneous THz field within a very short time window using visible laser pulses, THz TDS allows for a relatively simple experimental setup by not having to use liquid-helium cooled bolometers for detection. Moreover, it is insensitive to the blackbody radiation of the environment and can yield very high signal-to-noise ratio measurements [67].

Initially, the available frequency spectrum that could be generated and detected in the time domain was limited to a few THz [66]. Advances in the development of broadband ultrafast lasers and in the fabrication of new nonlinear optical materials have pushed this limit into the mid-infrared [83, 215, 101] and recently into the near-infrared, reaching frequencies beyond 100 THz ($\lambda = 3\mu m$) [182]. This chapter will be limited to THz time-domain spectroscopy using ultrafast lasers generating THz pulses - as opposed to continuous wave far-infrared spectroscopy using (FT-) IR spectrometers and THz sources from accelerators such as free-electron lasers. It also excludes works that have investigated THz radiation emitted from materials to study charge carrier and lattice dynamics [99, 32, 4].

One particular advantage of all-optical generation and detection of THz pulses, is the possibility to combine the approach with a time-synchronized femtosecond excitation pulse. Pulsed, time-domain THz spectroscopy thus not only allows for the characterization of charge carriers under steady-state conditions, but is also ideally suited for non-equilibrium measurements: using a time-resolved THz spectroscopy setup, an optical pulse can be used to create charge carriers and the subsequent evolution of charge carriers can be monitored on the femtosecond timescale (see, e.g. [6, 10, 180, 44]). In this way, one has direct access to the timescales and mechanisms of carrier cooling, trapping and recombination, as well as the dynamics of formation of quasiparticles such as excitons and polarons. This attribute permits THz spectroscopy to circumvent many of the constraints of conventional transport measurement techniques. Accordingly, much progress has been made in the past two decades in understanding the physics of elementary electronic excitations, owing to the development of sources and detectors of coherent THz radiation.

In the remainder of this Chapter, I will first describe theoretical foundation and experimental approaches related to generation and detection of THz radiation, and describe several THz time-domain spectroscopy setups. Then follows a section on signal analysis, i.e. describing how the carrier conductivity response can be extracted from the data, and how this compares to conventional transient photo-conductivity measurements. Finally, the typically observed THz responses of charge carriers in different semiconductor systems (bulk, confined) will be discussed.

1.2 Experimental methods

In this Section we describe the most common THz emitters and detectors. We limit the scope primarily to pulsed table-top sources and detectors that are based on femtosecond lasers and allow electric field-resolved measurements. Therefore, THz sources such as synchrotrons [209, 210], free-electron lasers [149], quantum cascade lasers [47, 178] and gas lasers and THz detectors such as bolometers and pyroelectric detectors are left out. Details about these sources and detectors can be found in earlier papers [19, 212]. In Sect. 1.2.1 and 1.2.2 we describe the generation and detection of THz electromagnetic transients based on either photoconductivity or optical nonlinearity of a medium. We then describe how to combine the generation and detection capabilities for the THz time-domain spectroscopy (Sect. 1.2.3) and the analysis methods that can be used to extract properties of material of interest in the THz spectral regime (Sect. 1.3). The basics of THz time-domain spectroscopy have been introduced in several review papers [66, 134, 217].

1.2.1 Generation

Photoconductivity and nonlinear optical processes are the two major techniques that have been utilized to generate THz electromagnetic transients from femtosecond lasers. A description of each of these methods, a comparison of the characteristics of the THz emission derived from these techniques, and a discussion of approaches for the generation of high-power THz radiation are included in this Section.

Generation of THz radiation by photoconductivity

THz generation based on photoconductivity is a resonant process in which a femtosecond optical pulse is absorbed through inter-band transitions in a semiconductor to produce charge carriers. These carriers are subsequently accelerated in either an externally applied DC electric field or a built-in electric field in the depletion or accumulation region of the semiconductor. A transient current is thus formed which in turn emits a THz electromagnetic transient that can propagate either on a transmission line or in free space [190].

In the far field the emitted THz electric field is proportional to the first time derivative of the transient current. The current transient is limited by the duration of the optical excitation pulse and the carrier scattering time, as well as the recombination lifetime of the semiconductor and the time that it takes the carriers to drift out of the active emitter area. Therefore, commonly used semiconductors for THz generation are defect-rich to reduce the fall time of the transient current. Examples include low-temperature grown or ion-implanted GaAs and silicon [184, 140, 126, 142]. Following the pioneering work of Auston, Grischkowsky and their coworkers, researchers have optimized ultrafast photoconductive switches in the past two decades to permit generation and field-resolved detection of electromagnetic transients up to ~ 5 THz [66, 5]. Such a bandwidth, while impressive, actually reflects the finite response time of photoconductive materials rather than the ideal bandwidth that could be obtained from current state-of-the-art modelocked laser pulses. For instance, a 10-fs transform-limited optical pulse (with a bandwidth of ~ 50 THz), should in principle permit generation and detection of electromagnetic transients up to ~ 50 THz. However, the comparatively slow response of the carriers in available photoconductive media significantly degrades the high-frequency performance. In contrast, optical rectification, as described in the next Section, can potentially generate THz emission with a bandwidth limited only by the duration of the optical excitation pulse. Under the assumption of perfect phase matching and a second-order nonlinearity of the emitter independent of frequencies in the region of interest, the emitted THz electric field in the far field is proportional to the second time derivative of the nonlinear polarization which follows the intensity envelope of the excitation pulse.

With respect to the strength of the THz emission, a linear dependence of the THz electric field on the DC bias [174, 29] has been observed. At low excitation fluence, the THz field also varies linearly with fluence; however, high excitation fluence often leads to saturation of the THz emission. There are two main reasons for saturation: (i) the resultant high charge densities effectively screen the bias electric field; and (ii) the electric field of the emitted radiation acts back and further decreases the net bias field [11, 111]. Photoconductive antennas and coplanar transmission lines with a small gap (10's of microns) are often used with a femtosecond oscillator source that delivers optical pulses of energy on the order of 10^{-9} Joule/pulse. A bias electric field of ~ 10^6 V/m can be applied and a typical THz pulse energy of ~ 10^{-13} J (and of peak power of 10^{-5} W) can be achieved. With an amplified femtosecond laser source that delivers pulses of energy on the order of 10^{-3} J/pulse, to avoid saturation, large aperture structures (~ mm gap size) or bare semiconductor wafers are often used. THz emission with a peak electric field up to 150 kV/cm, corresponding to an energy of 10^{-7} J/pulse and a peak power of 10^5 W has been reported [221]. Details can be found in earlier reviews [24, 177].

Generation of THz radiation based on nonlinear optical processes

An alternative method to generate THz radiation is to rely on nonresonant nonlinear optical processes such as optical rectification. Optical rectification is a second-order nonlinear process in which a DC or low-frequency polarization is generated when an intense laser beam propagates through a non-centro-symmetric crystal. It can be viewed as difference-frequency generation between the different frequency components contained within the bandwidth of an optical excitation pulse. In contrast to photoconductivity, it is a nonresonant process and can therefore withstand higher excitation fluences and, very importantly, generate THz emission with a bandwidth limited only by that of the optical excitation pulse.

In choosing appropriate nonlinear crystals for THz generation, several factors need to be considered: (For more details see [174])

- The achievable THz bandwidth is always fundamentally limited by the bandwidth of the laser excitation pulse. As an example, a Fourier-transform limited 100 fs pulse at 800 nm wavelength is characterized by a width of 10 nm which translates to a maximum THz bandwidth of about 5 THz.
- The material should possess a large nonlinear susceptibility combined with a high damage threshold.
- The material should be transparent throughout the desired frequency range, both in the terahertz and optical regime. Unfortunately most of the commonly used inorganic crystals exhibit phonon modes between 5-10 THz.

- For efficient nonlinear processes, the phase-matching condition has to be fulfilled. For optical rectification this requires that the group velocity of the excitation pulse matches the phase velocity of all frequency components of the emitted THz pulse [152]. For instance, for an optical excitation pulse centered at 800 nm (1.55 eV), ZnTe and GaP with an optical gap around 2.3 eV have a coherence length exceeding a mm for THz frequencies up to 2.2 THz [152].

Based on the above requirements, standard choices for nonlinear crystals for optical rectification using a Ti:sapphire laser are: ZnTe for the 0-3 THz range, GaP for 2-7 THz, and GaSe for 8-40 THz [83, 215, 101]. There have also been considerable efforts in the development of organic materials for optical rectification. Examples include DAST [106], MBANP crystals, and dye-doped polymers [224]. Organic materials often possess larger nonlinearities than inorganic materials, but may exhibit relatively low damage threshold or a lack of photo-stability.

Plasmas have recently been recognized as another attractive nonlinear medium for THz generation. The lack of absorbing phonon modes in plasma permits the generation of broadband radiation without spectral gaps. Spectral components up to 75 THz have been observed and center frequencies up to 30 THz have been predicted for an excitation pulse of 50 fs duration [112]. Plasmas have also been shown to generate intense THz radiation, with energies exceeding $> 5\mu$J per pulse [112]. In these experiments a focused fundamental pulse at 800 nm is mixed with its second harmonic at 400 nm in a gas [27]. The fundamental beam ionizes the gas in its focus, which then acts as the nonlinear medium. Several groups have worked on understanding and optimizing this process. Researchers have examined the dependence of the THz emission on the parameters such as the phase and polarization of the optical excitation [218, 82], the optical pulse duration [7], the external DC bias [199], and the type of gas [23, 136]. However, the underlying microscopic mechanism of the process is still a subject of debate [199, 105].

1.2.2 Detection

Like the generation process, detection of THz electromagnetic transients based on a femtosecond laser can be achieved by either photoconductive or nonlinear optical methods [20]. The working principle of a photoconductive antenna detector is similar to the emitter case, but now the bias is delivered by the THz pulse: when the optical probe pulse and a THz pulse simultaneously interact with the switch, the former produces charge carriers and the latter drives them to form a current between two contacts. The electric field (including both its amplitude and sign) associated with the THz radiation at the instant of overlap with the optical probe pulse can thus be determined from the THz-induced photo-current. To obtain the entire waveform of the THz electromagnetic transient one simply needs to apply a sampling technique, by varying the time delay between the THz and the optical probe pulses [187, 20].

Another method of detection of THz electromagnetic transients is to employ the electro-optic (EO) effect. The linear EO effect (also known as the Pockels effect) produces a birefringence in materials with inversion symmetry upon application of a bias electric field [214, 151]. In this case the electric field associated with the THz radiation acts as the bias field. The induced birefringence then causes a rotation of the polarization of the probe optical beam, which is measured from the optical power transmitted through the EO crystal surrounded by two crossed polarizers. To obtain the entire waveform a sampling scheme can be used just as for photoconductive detection. Because the same mechanism is involved in both generation and detection, identical materials can be used for emitters and detectors. A more comprehensive review of both methods of THz detection, with a detailed description of the underlying physics, can be found in [174].

Below we note a few key properties of the EO detection method of the THz radiation.

- Multichannel detectors can be easily incorporated into the detection scheme for either spatial imaging of the THz radiation or detection of the THz electric-field waveform in a single laser shot. The latter can be achieved by translating the time dependence into spectral dependence using a chirped optical probe beam [93], into spatial dependence in a non-collinear geometry of the THz and optical beams [186], or through other methods [219, 113, 108].
- The transmitted optical probe power through an EO crystal between two crossed polarizers varies with the phase shift caused by the birefringence in the system as $\sim sin^2\left(\frac{\varphi+\varphi_0}{2}\right)$. Here φ is the field-induced phase shift, which is linearly proportional to the THz electric field and φ_0 is a field-independent constant phase shift, the origin of which is discussed below. Such a relationship can be linearized around the constant phase φ_0 if $\varphi_0 \gg \varphi$. A phase shift of $\varphi_0 = \pi/4$ is introduced to obtain the greatest absolute modulation in the probe beam intensity for a given THz field strength [151, 214]; and a near-zero phase shift is introduced for measurements that benefit from a higher modulation depth of the probe beam [94, 186]. In cubic materials such as ZnTe and GaP (with no birefringence ideally) the former can be achieved by making use of a quarter wave plate and the latter by relying on the residual birefringence in the crystals (for instance, due to stress). However, in the shot noise limit both approaches yield a similar signal-to-noise ratio [94].
- One major advantage of the EO detection method is its time resolution, which is, in principle, limited only by the duration of the optical probe pulse. To achieve such ideal time resolution, crystals with good phase-matching properties and thin crystals are often employed. Zhang [68], Leitenstorfer [83], and their coworkers have demonstrated a detection bandwidth > 30 THz using free-space EO sampling in thin inorganic semiconductor crystals such as ZnTe, GaP, and GaSe. Cao *et al.* [21] have done similarly with poled polymers. By combining a thin GaSe emitter (90 μm) and a thin ZnTe detector (10 μm) Huber and coworkers [83] have been able to obtain THz pulses shorter than 50 fs (bandwidth ~ 40 THz) based on a 10-fs laser. The highest spectral components that have been demonstrated using electro-optical sampling to date exceed 135 THz

[181].

1.2.3 THz time-domain spectroscopy setups

The basic techniques for THz generation and detection have been outlined above from the point of view of the fundamental processes of photoconductivity and optical nonlinearity. In this Section we introduce a typical experimental setup for performing THz Time-Domain spectroscopy (TDS). A schematic representation of a typical THz TD spectrometer is illustrated in Fig. 1.1. It consists of a modelocked laser, a THz emitter and detector, and elements to couple and propagate THz radiation from the emitter to the detector. The modelocked laser provides a train of femtosecond optical pulses that are divided into two arms. One laser pulse is used to excite the emitter (either a photoconductor or a second-order nonlinear crystal). The second pulse, introduced at a defined time by an optical delay line, is used to detect the generated THz radiation in the detector (either a photoconductive switch or an electro-optic crystal).

In the experimental setup, the modelocked laser is often a Ti:sapphire laser that typically delivers pulses of less than 100 fs duration at a wavelength near 800 nm. An

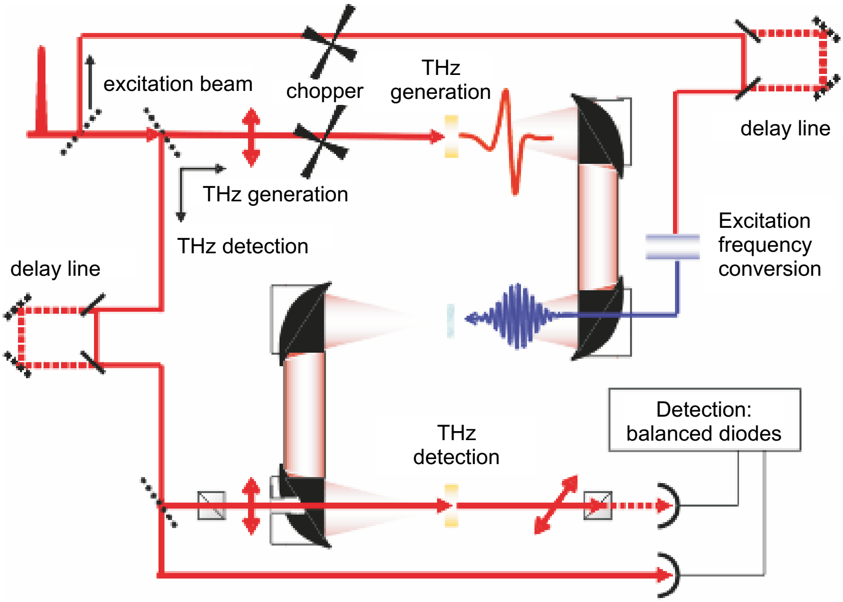

Figure 1.1: Schematic representation of an optical pump - THz probe experimental setup. A train of ultrashort laser pulses enters the setup from the upper left corner, and is split into three: the excitation beam, and two beams for the generation and detection of THz pulses. A mechanical chopper is placed in either the excitation or generation beam, depending on the type of experiment. In the balanced detection scheme, the THz field-induced rotation of the polarization of the detection pulse is measured as indicated. Two optical delay lines are used to control the delay times between the three pulses.

important characteristic of the laser system is its stability both in power and pointing direction because the technique relies on separate sample and reference measurements to determine the sample properties. For certain applications, such as ultrabroadband THz spectroscopy, the stability of the duration of the optical pulse also plays a key role in the system performance. Recently, modelocked fiber lasers based Er/Yt-doped glass [50] have emerged as attractive sources for compact THz-TDS setups [182]. Many of the emitters and detectors discussed in previous sections are optimized for operation with Ti:sapphire lasers at a wavelength of 800 nm, rather than at the 1550 nm wavelength of the modelocked fiber lasers. However, progress has been reported in the development of emitters and detectors suitable for these new fiber laser sources [164, 22]. These compact systems are expected to play an increasingly important role in the future of THz spectroscopy.

A critical element in the THz-TDS system is the efficient coupling between the emitter and detector, which is of particular importance for photoconductive switch-based THz systems. Lenses of silicon or other high index materials are often attached to the emitter and detector for efficient coupling. In addition, parabolic mirrors are used to guide the THz radiation in free space from the emitter to the detector. Two configurations are commonly used in THz spectrometers: a confocal system consisting of a pair of parabolic mirrors that has a frequency dependent beam waist at the midpoint and the emitter and detector in the focal planes; and a system consisting of two pairs of parabolic mirrors arranged to have the emitter, detector and the midpoint in the confocal planes. The latter is often used in THz imaging and optical pump-THz probe systems. To reduce absorption of the THz radiation by water vapor the spectrometer is often purged with dry air or nitrogen gas. More details about the THz-TDS systems can be found in [24, 134, 10].

The THz-TDS system can be easily converted into an optical pump-THz probe setup by introducing an optical pump pulse. The pump pulse is usually derived from the same laser, as shown in Fig. 1.1. The optical pump and the THz probe spatially overlap at the sample. The time delay between the two pulses can be varied by adjusting an optical delay line.

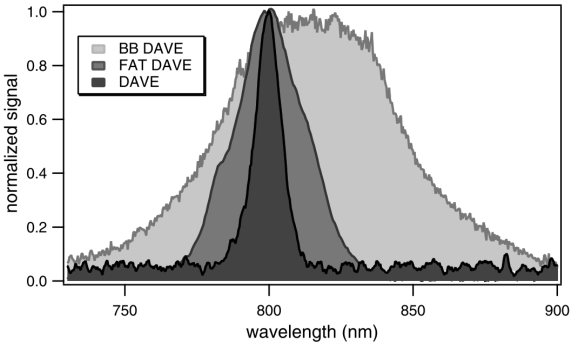

Figure 1.2: Spectra of the output pulses of the three different Ti:Sapphire lasers employed for THz spectroscopy in the group: BB DAVE (modelocked, cavity-dumped, 70nm bandwidth, sub-20 fs), FAT DAVE (amplified, 30nm bandwidth, 35 fs), DAVE (amplified, 10nm bandwidth, 100 fs).

Our group employs three different pulsed Ti:Sapphire lasers to drive time-resolved THz setups: DAVE, FAT DAVE and BB DAVE. The latter two setups were built during the course of this thesis. All three lasers differ in the emitted pulse duration and thus in the bandwidth. The respective spectra of the delivered 800 nm pulses are plotted in Fig. 1.2.

DAVE is the "workhorse" of the group, driven by a 1W, 100 fs, amplified system running at a repetition rate of 1 kHz (Coherent Legend, seeded by Vitesse and pumped by Evolution). For the generation and detection of THz pulses ZnTe crystals are used. The produced THz time-domain trace and its according Fourier-transformation is shown in the upper panel of Fig. 1.3. The to-be-measured signal from the balanced diodes is either acquired using a lock-in amplifier or a boxcar integrator and then sent to the measurement computer. The fundamental pump wavelength of 800nm can be converted by using BBO crystals to generate the 2nd (=400nm) or 3rd (=266nm) harmonic.

FAT DAVE is similar to the DAVE setup in terms of layout, probe spectrum and data acquisition. It is however driven by two synchronized amplified laser systems (Spectra Physics Spitfire Ace, seeded by Mai Tai and pumped by Empower), with each of them running at 1 kHz, delivering 35 fs pulses at 4W output power. The output of the first laser is used to generate and detect the THz probe pulse, whereas the second one delivers the output for the pump path. Using an optical parametric amplifier (OPA), its output wavelength can be tuned between the mid-infrared and the ultra-violet, permitting studies of systems where more specific excitation energies are required. The advantage of having two separate but synchronized lasers for excitation and THz probe, respectively, is that the time delay between pump and probe can be as long as 1 ms, and thus much longer than the common 1 ns maximum achieved using a mechanical delay stage. This allows to monitor, for instance, recombination processes occurring on such long timescales.

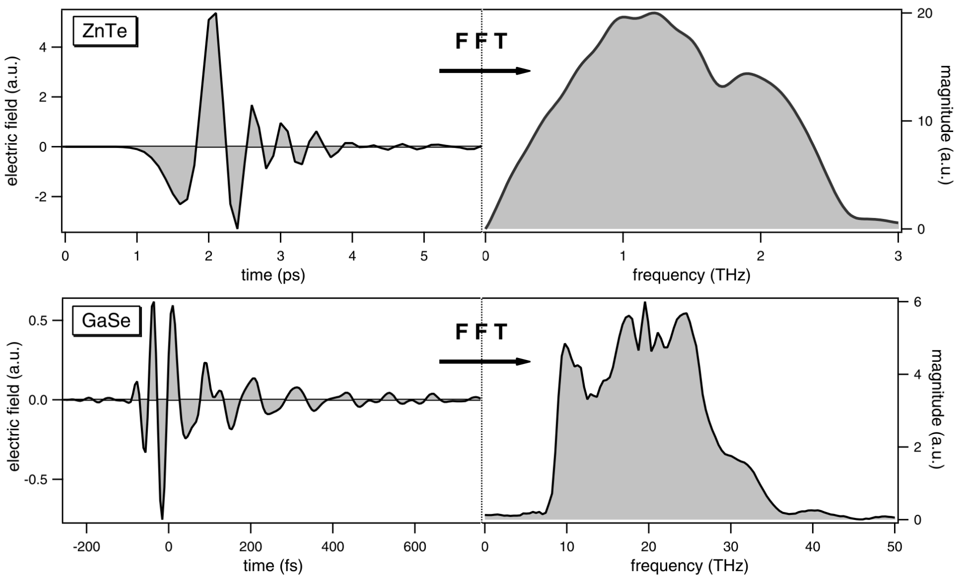

Figure 1.3: Electric fields of the probe radiation (left side) created in our laboratories and their respective spectra (right side); upper panel: ZnTe generation and detection; lower panel: GaSe generation and detection.

The BB DAVE setup sets itself apart from the other two in that its output bandwidth is large enough to create a probe spectrum that lies in the mid-infrared, generated and detected with GaSe crystals (see Fig. 1.3, lower panel), and in that it is not driven by an amplified laser. Rather, a modelocked Ti:Sapphire oscillator (Coherent Mantis) with an attached cavity-dump unit (APE PulseSwitch), is used. The cavity-dumper extends the cavity of the oscillator, thereby decreasing the intrinsic repetition rate from 76 MHz to 54 MHz. The cavity-dumper serves two main purposes: the repetition rate can be varied continuously from MHz to kHz rates. Lower repetition rates are necessary for the study of materials with long recombination times, such as indirect bandgap semiconductors. At the same time, the pulse energy increases when the repetition rate is lowered, saturating at around 35nJ for rates at and below 1 MHz.[1] This value is about a factor five larger than the pulse energy of a similar oscillator running at its intrinsic repetition rate - an obvious benefit for pump-probe experiments. We thus operate the laser at 1 MHz or below, if necessary.

---

[1] The pulse energy saturates at 1 MHz because the system approaches the fluorescence lifetime of the Ti:Sapphire crystal (~ 3μs), which prohibits further amplification.

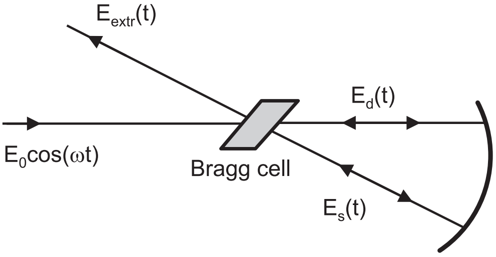

Figure 1.4: Schematic of the double-pass cavity dumper that allows to continuously change the repetition rate of the modelocked laser that drives the BB DAVE setup. Adapted from the manual.

The cavity-dumper is based on the acousto-optic effect where part of the laser pulse is diffracted out of the cavity upon passing a fused silica crystal (the Bragg cell) in which the refractive index is modulated periodically (grating) by a traveling acoustic wave. This acoustic wave is launched in the Bragg cell through the application of an electric RF signal with a frequency of 380 MHz and a maximum power of 16.5W to a piezoelectric transducer cemented to the Bragg cell. A particular feature is that the pulse is diffracted out twice and not only once (double-pass cavity-dump), as shown schematically in Fig. 1.4. This allows to obtain high dumping efficiencies of up to 60%, making it at the same time however very sensitive to precise alignment since the two outcoupled pulses have to interfere constructively.

In the first pass, the cavity pulse $E(t) = E_0\cos(\omega t)$ (with ω being the laser carrier frequency) propagates through the Bragg cell, where part of it ($E_s(t)$) is diffracted with an efficiency η and the remaining, depleted, pulse transmitted ($E_d(t)$). During the second pass, $E_d(t)$ is diffracted, too, and the total extracted ("dumped") pulse is given by

$$E_{extr} = \sqrt{\eta - 1}\sqrt{\eta}E_0\left[\cos(\omega t + \Omega t + \Phi) + \cos(\omega t - \Omega t - \Phi)\right]$$

where Ω is the applied radio frequency (380 MHz) and Φ its phase.

The laser output is sent into a grating compressor (Coherent CPC), where a pre-chirp can be applied to the pulse in order to compensate for dispersive optics in the setup. The drawback is that 20% of the pulse energy is lost.

In the setup, respectively 5% of the output power are split off for the generation and detection of the probe radiation. The remainder (~ 23nJ) is used as the excitation pulse which can also be frequency-doubled to 400nm using a BBO crystal. The available pulse energy may at first glance seem low for pump-probe experiments in comparison to the hundreds-of-μJ output that is on hand in the other setups. The focus of the probe beam is however orders of magnitude smaller (FWHM ~ 50 μm) due to its lower wavelength. The beam size area of the excitation beam can thus be reduced by about a factor 1000 as compared to the other setups, which moves the resulting pump fluences to a usable range.

The type of delay stage for the electro-optic sampling process is different from the ones employed in the other setups. Instead of using a translation stage with stepper motor that remains fixed at a certain delay position during the course of the signal averaging time (commonly hundreds of milliseconds to seconds), the retroreflector that is used to bounce back and delay the beam is mounted on a frictionless spring bearing (APE ScanDelay). The reflector can be driven in a sinusoidal back-and-forth motion with frequencies up to 20 Hz. The maximum amplitude of this motion is equivalent to a time delay of 15 ps, and thus long enough to cover the whole probe electric field trace. The advantage of using this "shaker" is on the one hand an improvement in the signal-to-noise ratio, for it reduces long-term noise below the oscillation frequency, and on the other hand the provision of real-time THz spectra, which is beneficial for alignment purposes and rapid evaluation of the measured signal.

The signal from the balanced diodes is acquired for every single laser shot, and thus with a rate of up to 1 MHz, using a suitably fast DAQ card (National Instruments NI 6124). In addition to the diode signal, the current position of the retroreflector (which is passed on from its control unit in form of a voltage) is recorded at the same time, as well as the parity of the chopper that is modulating the excitation beam (i.e. whether the beam had been blocked or not). All acquired data is binned and post-processed in a suitable manner by the acquisition software.

1.3 Extracting the THz response

The THz-TDS systems described in the previous section are capable of generating and detecting the electromagnetic transients on the femtosecond time scale. To use these capabilities to characterize material properties in the THz spectral regime, a measurement of the THz electric-field waveform is first obtained without the sample in place [$E_{ref}(t)$] and then with the sample in place [$E(t)$], either in a reflection or transmission geometry [66]. Below we describe how to extract the material properties as reflected in the complex dielectric function (or equivalently the complex refractive index or conductivity) from the measurements.

1.3.1 Obtaining the complex dielectric function

The linear response of material can be described by its complex dielectric function $\epsilon(\nu)$ as a function of the frequency ν. The complex dielectric function is directly related to the complex refractive index $n(\nu)$ by $\epsilon(\nu) = n^2(\nu)$, and to the optical conductivity $\sigma(\nu)$ by $\sigma(\nu) = -2\pi i\nu\epsilon_0(\epsilon(\nu)-1)$, where ϵ_0 is the vacuum permittivity. The goal of a THz-TDS experiment is usually to extract this material response. In this Section, we discuss the general procedure for doing so.

The material response can be extracted through the Fourier transforms of the measured electric-field waveforms for the sample $E(\nu)$ and the reference $E_{ref}(\nu)$. The transmission $t(\nu)$ or reflection $r(\nu)$ of the electric field $(= E(\nu)/E_{ref}(\nu))$ can be related to the parameters of the sample. In the general case of a multilayered planar system of N layers, a transfer matrix analysis can be applied [53]. For simplicity, we assume the permeability of the materials to be one. The characteristic matrix for normal incidence at m-th layer of thickness d_m and dielectric function ϵ_m, is given by

$$z_m(\epsilon_m,\nu) = \begin{bmatrix} \cos(\beta_m) & -\frac{i}{\sqrt{\epsilon_m}}\sin(\beta_m) \\ -\frac{i}{\sqrt{\epsilon_m}}\sin(\beta_m) & \cos(\beta_m) \end{bmatrix}, \tag{1.1}$$

where $\beta_m = \frac{2\pi\nu d_m\sqrt{\epsilon_m}}{c}$ is the phase delay associated with propagation inside the m-th layer and c is the speed of light in vacuum. The characteristic matrix of the entire multilayer system is given by the product of individual layer matrices $z = z_N z_{N-1}...z_1$. The transmission and reflection coefficient of the system are determined by the matrix elements (i, j = 1,2) of the characteristic matrix of the entire system z:

$$r(\epsilon_1,\epsilon_2,..,\epsilon_N,d_1,d_2,..,d_N,\nu) = \frac{(z_{11}+z_{12})-(z_{21}+z_{22})}{(z_{11}+z_{12})+(z_{21}+z_{22})}$$

$$t(\epsilon_1,\epsilon_2,..,\epsilon_N,d_1,d_2,..,d_N,\nu) = \frac{2}{(z_{11}+z_{12})+(z_{21}+z_{22})}$$

In case of a slab of homogeneous material of thickness d and dielectric function $\epsilon_2(\nu)$ with media 1 and 3 on its two sides, a common experimental geometry, one retrieves the following more familiar expression for the transmission coefficient:

$$t(\epsilon_2,\nu) = \frac{E(\nu)}{E_{inc}(\nu)} = \frac{t_{12}t_{23}e^{i\beta_2}}{1+r_{12}r_{23}e^{i2\beta_2}} \tag{1.2}$$

Here $t_{ij} = \frac{2\sqrt{\epsilon_i}}{\sqrt{\epsilon_i}+\sqrt{\epsilon_j}}$ and $r_{ij} = \frac{\sqrt{\epsilon_i}-\sqrt{\epsilon_j}}{\sqrt{\epsilon_i}+\sqrt{\epsilon_j}}$ are the Fresnel transmission and reflection coefficients for normal incidence to an interface from medium i to j and $E_{inc}(\nu)$ is the incident field. The task is then to solve Eq.1.2 using experimentally determined $E(\nu)$ and $E_{inc}(\nu)$ and knowledge of the sample thickness to obtain $\epsilon_2(\nu)$. Generally, this will involve numerical calculations: Eq. 1.2 can either be solved using an iterative approach or piecewise in frequency to minimize phase and amplitude errors [40].

In the limit of a thin film sample of thickness $d \ll \lambda_{\mathrm{THz}}$ (where λ_{THz} is the wavelength of THz radiation), an analytical solution for the film dielectric function $\epsilon(\nu)$ is possible. Here we take the THz transmission through the film on a substrate as $E(\nu)$ and the THz radiation transmitted through the bare substrate as $E_{ref}(\nu)$. One can carry out a Taylor expansion of the exponential terms in Eq. 1.2 to obtain

$$\frac{E(\nu)}{E_{ref}(\nu)} = \frac{1+i\beta}{1+\frac{i2\pi\nu d}{c}\left(1+\frac{(\sqrt{\epsilon}-1)(\sqrt{\epsilon_{sub}}-\sqrt{\epsilon})}{1+\sqrt{\epsilon_{sub}}}\right)}, \tag{1.3}$$

where ϵ_{sub} is the substrate dielectric function. Eq. 1.3 can be readily solved analytically to obtain $\epsilon(\nu)$.

We note that in deriving the characteristic matrix described in Eq. 1.1, we assume that the THz beam can be represented as a superposition of plane waves of frequency ν

propagating along a fixed direction (normal to the sample in this case) and the beam shape is not altered by the sample. These assumptions are usually valid. In case of significant diffraction, the spatial profile of the THz pulse needs to be measured and a spatial Fourier transform needs to be used in addition to the temporal Fourier transform above.

The measurement technique and the analysis method described here are very general. They can be applied to material systems ranging from dielectrics to semiconductors to metals, in gas, liquid, and solid forms. They can be applied to a homogeneous sample or a composite. In the next Section 1.3.2 we describe how to extract the dielectric properties of constituents of a composite based on the effective medium theory (EMT). The THz-TDS technique and the analysis method described above, however, have restrictions. We list some of the major ones below.

- The dynamic range (ratio of the peak electric field to the minimum detectable field) of THz-TDS is typically large. For photoconductive antenna-based systems, dynamic ranges over 10,000 have been achieved. However, the precision of the measurements is usually limited by the laser noise, which is typically 0.1 - 1%. This in turn places a minimum limit on the thickness of a sample for which the complex dielectric function can be reliably inferred (typically $\left|\sqrt{\epsilon}\right| \frac{2\pi\nu}{c} d > 10^{-2}$). To measure samples with a weak effect on the THz radiation, modulation techniques are often required. For instance, the sample can be moved in and out of the beam, with the difference between the signal with and without the sample, $E(t)$ - $E_{ref}(t)$, being detected by a phase-sensitive detector. More details can be found in [92, 141, 17].
- Because the analysis of THz measurements involves a Fourier transform of the electric-field waveforms, the bandwidth of the measurement is numerically limited by the Nyquist frequency, $(2\Delta t)^{-1}$, where Δt is the time step of the delay line. Typically Δt is chosen so that the Nyquist frequency is two or three times the physical bandwidth of the system.
- The spectral resolution, $\Delta\nu$, of the THz-TDS is determined by the duration of the measured waveforms. For a fixed step size Δt and N data points acquired, the resolution is given by $\Delta\nu = (2N\Delta t)^{-1}$. For instance, for a 100-ps measurement scan, this corresponds to a spectral resolution of ~ 5 GHz. Such a resolution is usually not an issue for solids or liquids that have broad resonances, but the linewidths of gases are often limited by the instrumental spectral resolution.

1.3.2 Inhomogeneous materials

Above in Sect. 1.3.1 we considered homogeneous media. The analysis is also applicable to inhomogeneous materials with inhomogeneities on a length scale much smaller than the wavelength of the THz radiation. These systems include nanocomposites and nanoporous materials. An effective dielectric function $\epsilon(\nu)$ can be extracted from the THz measurements. In order to obtain the properties of the constituents, an effective medium theory (EMT) is usually applied.

There are many EMT's in the literature [25]. Maxwell-Garnett (MG) [59] and Bruggemann [18] are the two most widely used ones. For particles made of a material of dielectric function ϵ_p embedded in a medium of dielectric function ϵ_m the effective dielectric function of the composite ϵ is the solution of the following self-consistent equations:

$$\text{MG: } \frac{\epsilon - \epsilon_m}{\epsilon + \kappa\epsilon_m} = f\frac{\epsilon_p - \epsilon_m}{\epsilon_p + \kappa\epsilon_m} \tag{1.4}$$

$$\text{Bruggemann: } f\frac{\epsilon_p - \epsilon}{\epsilon_p + \kappa\epsilon} = (f-1)\frac{\epsilon_m - \epsilon}{\epsilon_m + \kappa\epsilon} \tag{1.5}$$

Here f is the filling factor in volume and κ is the geometric factor related to depolarization ($\kappa = 2$ for spheres) [59]. In contrast to the Bruggemann approximation, in MG EMT the role of the particles and their surroundings is not symmetric and is applicable only for dilute composites. The general consensus is that Bruggemann formula is more appropriate for composites consisting of two or more components at high filling factors. However, it is well known that the Bruggemann effective medium theory does not reproduce some important material properties, such as plasmon resonances in percolated conductors [175].

1.3.3 Analysis of photoinduced changes in the dielectric function

Now we turn our discussion to the analysis of typical optical pump/THz probe measurements. In these experiments the electric-field waveform $E(t)$ of THz pulses transmitted through an unexcited sample and the pump-induced change in the THz waveform, $\Delta E(t)$, are recorded. The latter is done by using a lock-in technique with modulation of the optical pump beam for each fixed delay time τ between the optical pump and THz probe pulse. In such experiments, we are interested in retrieving the photoinduced change $\Delta\epsilon(\nu)$ in the complex dielectric function $\epsilon(\nu)$ as a function of the frequency ν. This can be achieved using the Fourier transform of the two waveforms $E(\nu)$ and $\Delta E(\nu)$ following a similar procedure as in Sect. 1.3.1, where here we have:

$$\frac{\Delta E(\nu)}{E(\nu)} = \frac{t(\epsilon + \Delta\epsilon, \nu) - t(\epsilon, \nu)}{t(\epsilon, \nu)}$$

Note that, for now, we consider the simple case of a quasi-static limit, in which the photo-induced change in the material properties changes, after photo-excitation, on a much longer time scale than the THz pulse duration. In other words, the properties of the sample do not change during the ~1 ps duration of the THz pulse. Such a quasi-static condition is satisfied in a material with a long carrier lifetime and

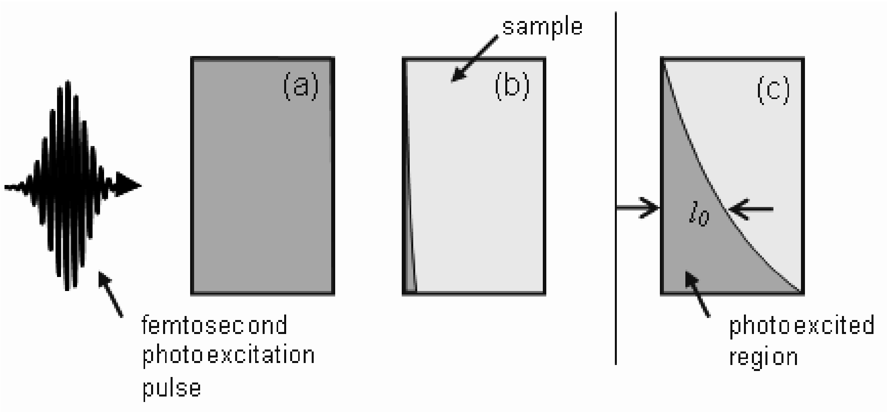

Figure 1.5: Schematic of typical sample excitations achieved in an optical pump - THz probe experiment. Experiments with homogeneous excitation (a) and interfacial excitation (b) can be treated analytically.

probed several picoseconds after pump excitation when the fast hot carrier effects have abated.

We first consider the analysis for a homogeneously excited slab of material in vacuum of thickness d (Fig. 1.5(a)) In the limit of a weak perturbation to the THz response, a linear relation between the pump-induced response and the ratio of the Fourier transform of the waveforms can be found, ignoring multiple reflections [121]:

$$\Delta\epsilon(\nu) = 2\epsilon(\nu)\left[i\sqrt{\epsilon(\nu)}\frac{2\pi\nu d}{c} - \frac{\sqrt{\epsilon(\nu)}-1}{\sqrt{\epsilon(\nu)}+1}\right]^{-1}\frac{\Delta E(\nu)}{E(\nu)} \tag{1.6}$$

This expression includes propagation of the THz probe through the sample, as well as interfacial reflection losses at the boundary of the sample.

A useful approximation can also be applied when only a very thin region near the surface of a sample is excited (Fig. 1.5(b)). This situation occurs when the pump light is strongly absorbed by a material, such as for above-band-gap photoexcitation of a semiconductor. It is convenient to approximate the excited region by a homogeneous region of width l_0, the penetration depth of the optical excitation in the sample. If the excitation density is sufficiently small, the phase accumulated by a THz wave propagating through the excited region will be small (i.e., $\sqrt{(\epsilon+\Delta\epsilon)}2\pi\nu l_0/c \ll 1$). The exponential terms in the transmission function of the photoexcited region given by Eq. 1.6 can again be approximated by Taylor expansions. We thus obtain the following expression for the average change in the dielectric function inside the photoexcited region:

$$\Delta\epsilon_{av}(\nu) = -i\frac{c\sqrt{\epsilon(\nu)}}{\pi\nu l_0}\frac{\Delta E(\nu)}{E(\nu)} \tag{1.7}$$

Note that Eq. 1.7 follows directly from Eq. 1.6 under the neglect of the reflection contribution, which is not altered by photoexcitation for this case. Equation 1.7 applies to a broad range of THz pump-probe experiments where the condition of $\sqrt{(\epsilon + \Delta\epsilon)}2\pi\nu l_0/c \ll 1$ is fulfilled (see e.g. [73, 129]).

The analysis, however, is complicated when the penetration depth, l_0, of the optical excitation in the material of interest is comparable to the wavelength of THz radiation. A numerical analysis is then required in which we divide the sample into many thin, homogeneous slabs, with different excitation densities. Similarly problematic is the effect of inhomogeneous excitation along the direction perpendicular to the propagation direction of the THz probe: finite difference time domain (FDTD) simulations are required [114].

The discussion above applies to quasi-static changes in the material response. When the change in the material response occurs on a time scale comparable to or shorter than that of than the THz pulse, one can no longer use the method described above for data analysis. This regime is typically encountered when probing immediately after optical excitation or in systems with very fast carrier recombination times. In these cases a complete two-dimensional scan of the pump-induced THz electric-field waveforms $\Delta E(t, \tau)$ at each optical pump-THz delay time τ must be considered within an overall model of the material response, since the time-dependent frequency-domain material response function discussed above has no general physical meaning. In the limit of weak material response to the pump beam, the measurement can be considered as a particular form of four-wave mixing. More details can be found in [155].

1.3.4 Comparison to conventional transient photo-conductivity

Optical pump-THz probe spectroscopy has emerged as a powerful technique for probing charge transport in a variety of homogeneous and inhomogeneous materials. It is therefore useful to compare this technique with the conventional transient photo-conductivity measurements, such as time-of-flight method [144, 133, 124, 14]. In these measurements a transient current induced by a static electric field is measured as a function of time after photoexcitation by a short optical pulse. In this Section, we briefly discuss the similarities and differences between these different experimental techniques.

In conventional transient photoconductivity measurements, the temporal evolution of the photo-induced current is determined by two factors: the density of mobile charge carriers induced by the photoexcitation and their response to the static external electric field. In Fig. 1.6 (a) we illustrate a simple time dependence of the transient current. Here the response of the photoexcited electrons is assumed to follow the Drude model with a scattering rate γ_0 and the population of the conduction electrons is described by a step function at time zero. This is representative of photoexcitaion in a bulk crystalline semiconductor by an ultrafast laser pulse. The transient current, calculated according to [75], is seen to rise exponentially with a time constant determined by the electron scattering rate. Thus, the time evolution of the

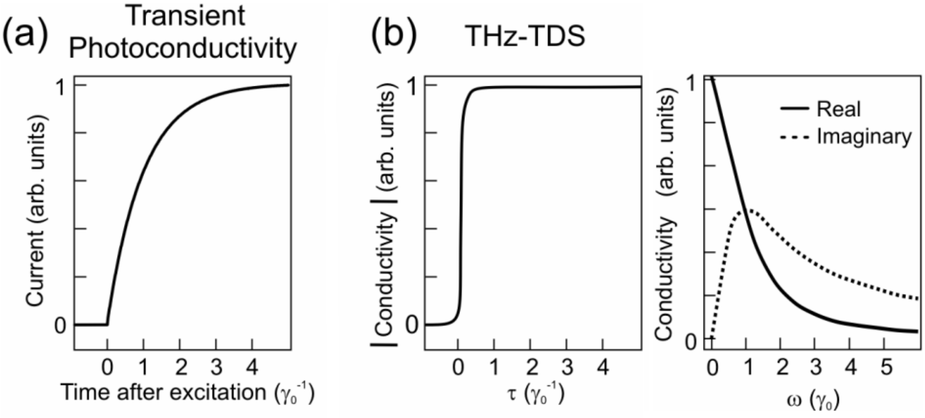

Figure 1.6: Time dependence of signals in a (a) transient photoconductivity measurement and (b) THz-TDS measurement, both for a Drude electron gas undergoing a step increase in density at time zero.

current has a signature of the type of photospecies, and the transport mechanisms and population dynamics in the material of study. A more complicated time dependence of photoconductivity is expected in cases where charge localization/hopping transport mechanisms [124, 14, 179], excitonic effects [144, 133], or population dynamics [163] are important.

In a typical optical pump-THz probe experiment, an optical pump pulse creates an excitation in a sample, which is probed with a picosecond THz pulse at a time τ after the excitation. In this case, one probes the time dependent conductivity of a material using a *transient* field $E(t)$ rather than a static one. Generally this is a two-dimensional detection of the THz probe electric field at time (t) and time (τ) after the photoexcitation. It is more straightforward to present this information in terms of a time and frequency-dependent conductivity $\sigma(\omega, \tau)$, i.e. a *frequency* dependent conductivity which depends parametrically on time τ after photoexcitation. If $\sigma(\omega, \tau)$ changes fairly slowly with time during the THz probe pulse (typically $\sim$ 1 ps), one can define a quasi-steady-state conductivity $\sigma(\omega)$ (see previous Section) that reflects *only* the dielectric response of the material (Fig. 1.6). The population dynamics is generally revealed independently of the dependence on τ as shown in figure 1.6(b)). This is one of the major differences between THz-TDS measurements and conventional photoconductivity measurements: for the latter, both the response of the photoexcited species and their time dependent populations manifest themselves in the transient current as a *function of time after photoexcitation*. It should be noted that the general case, where $\sigma(\omega, \tau)$ varies on a timescale that is shorter than the THz pulse duration, such a simple separation does not apply and the temporal evolution of the THz fields may be quite complex [161, 155, 156, 154, 114, 75], as different temporal segments of the THz pulses probe different sample properties.

The pulsed nature of the THz electric field in a THz-TDS measurement also has implications regarding the length scales over which conductivity is probed. For example, a simple estimate of the thermal velocity of an electron at room temperature (~ 10^5 m/s) indicates that, in the ~ 1 ps duration of a THz cycle, the motion of charges is probed only on a length scale of < 100 nm. Owing to the short time- and length scales over which the THz conductivity is determined, the THz conductivity is relatively insensitive to defect-related effects that impede carrier motion over large distances. As such, charge mobilities inferred from THz measurements therefore usually represent intrinsic, upper limits for electron transport [76].

Furthermore, the ability of THz TDS to take conductivity "snapshots" on such short timescales is particularly useful for the determination of the mobility in systems that possess a high density of trap states or fast electron-hole recombination channels, for instance. Chapter 2 presents measurements on type Ib diamond that possessed high densities of single substitutional nitrogen defects on the order of hundred parts-per-million. Electrons excited from these donor states into the conduction band showed fast recombination times of about ten picoseconds, which corresponds to electron diffusion lengths below $1\,\mu\mathrm{m}$. Traditional photoconductivity or time-of-flight measurements require much larger charge collection distances and would thus be unsuitable for such materials. Using THz TDS, it was possible to infer the electron mobility and recombination time and its dependence on defect concentration and temperature.

1.4 THz responses of charge carriers

In this section, we illustrate the capabilities and achievements of THz spectroscopy in characterizing certain charge carrier properties. In a simplified, classical picture, the response of charge carriers to the THz probe spectrum is in the first place determined by the THz-field-induced drift of the carriers and how additional correlations such as Coulomb forces between carriers and interactions with the lattice affect their motion. Additional restoring forces such as potential barriers or space charges can further have an influence. Last but not least, quantum phenomena can play a role, like the appearance of discrete energy levels following Bohr's hydrogen model in the case of exciton formation or the particle-in-a-box problem for quantum confinement.

1.4.1 Typical responses

Drude response

In bulk solids, the THz response of free carriers can often be described by a Drude response function, irrespective of whether the carriers originate from dopants or photoexcitation. The Drude formula can be derived from several descriptions of charge motion within a solid, including the semiclassical Boltzmann transport equation and the Kubo-Greenwood analysis [81, 127]. The model, as discussed below, involves just a single relaxation parameter. Despite its simplicity, it has been verified for charge transport over a spectral range from MHz to the optical frequencies [38] in various materials.

Heuristically, the Drude response can be derived from a simple semiclassical model of charge transport. In this picture, the charges are accelerated under the external electric field $E(t)$ according to the equation of motion:

$$\frac{d^2\mathbf{r}}{dt^2} + \gamma\frac{d\mathbf{r}}{dt} = -\frac{e}{m}\mathbf{E}(t), \tag{1.8}$$

where $\mathbf{r}$ is the ensemble average of the displacement of the charge carriers, γ denotes the damping rate or scattering rate, e is the electronic charge, and m is the effective mass of the charge carrier. For a given carrier density N the dielectric response function ϵ_D to an alternating external electric field at angular frequency $\omega(= 2\pi\nu)$ can be solved from Eq. 1.8. This yields the well-known Drude response:

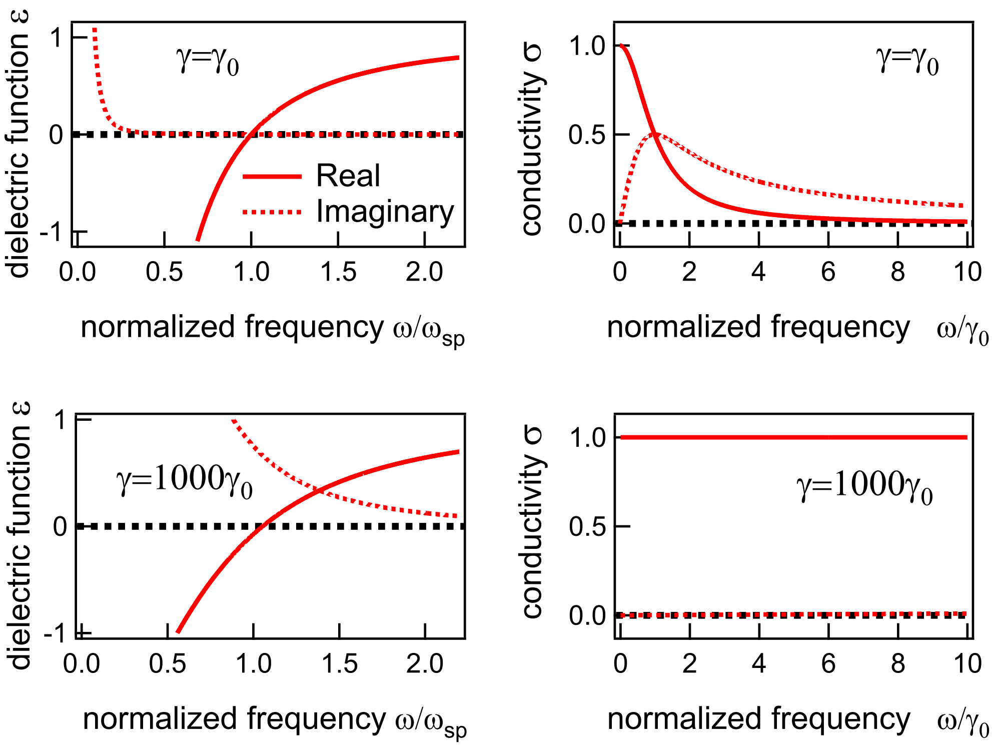

Figure 1.7: Drude response for two regimes of scattering rates relative to the probe frequency window. Upper row: complex dielectric function and conductivity for a relatively low scattering rate γ; Lower row: the same for a very high scattering rate. All solid (dotted) lines indicate real (imaginary) part of the response. Black dotted lines indicate zero point. γ_0 is a frequency unit. The frequency axes of the conductivity plots are normalized for γ_0 while for the dielectric functions they are normalized for the screened plasma frequency ω_{sp} and ϵ_∞ is set to 1.

$$\epsilon_{\mathrm{D}} = \epsilon_\infty - \frac{\omega_p^2}{\omega^2 + i\gamma\omega}$$

where ϵ_∞ is the background dielectric constant.

The Drude response is characterized by a Lorentzian resonance centered at zero frequency with a linewidth γ, which is the charge carrier scattering rate; the inverse of the scattering time τ. The amplitude of the dielectric response is determined by the plasma frequency ω_p, defined as:

$$\omega_p^2 = \frac{Ne^2}{\epsilon_0 m}$$

with N being the charge density and ϵ_0 the permittivity of free space. The real part of ϵ_{D} crosses the zero point at the screened plasma frequency $\omega_{sp} = \omega_p/\sqrt{\epsilon_\infty}$. By plotting the inverse of the dielectric response $1/\epsilon_{\mathrm{D}}$, also known as the dielectric loss function, we find a peak centered at ω_{sp}.

We can also write the Drude response in terms of the complex conductivity of the material

$$\sigma_{\mathrm{D}} = \frac{\sigma_{\mathrm{DC}}}{1 - i\omega\tau}, \tag{1.9}$$

Here the parameter $\sigma_{\mathrm{DC}} = Ne^2\tau/m$ gives the value of the DC conductivity of the material within the Drude model.

Depending on the relative value of the scattering rate and the position and width of the THz frequency window, the observed Drude response will vary. Figure 1.7 shows the predicted dielectric function and complex conductivity for the case of a scattering rate within the THz frequency window and for a far higher scattering rate. When the scattering rate is within the THz probe window, both the real and imaginary parts of the response are finite and dispersive. In this case, we can determine both of the parameters in the Drude model, i.e., the plasma frequency and the scattering rate. If the carrier mass is known, this analysis then provides the carrier concentration N from the plasma frequency and the carrier mobility $\mu = e/m\gamma$ from the scattering rate. When the scattering rate far exceeds the upper limit of the available THz frequency range, then the analysis can only yield the DC conductivity σ_{DC}. In this limit, the real part of the conductivity is finite, while the imaginary part is negligible. This corresponds to a purely imaginary (i.e. dissipative) dielectric function, with a trivial $1/\omega$ frequency dependence. For this case, one consequently cannot independently determine the carrier concentration and scattering time. In many experiments involving photogenerated carriers, the excitation conditions provide information on the carrier concentration. The THz data within the Drude model are then seen to provide the carrier mobility (or scattering rate, assuming existing knowledge of the carrier effective mass).

Charge carriers in many semiconductors exhibit scattering times of a few hundred femtoseconds, corresponding to linewidths of the Drude peak of around 1 THz. Such a response is therefore readily characterized by THz pulses generated with either photoconductive antennas or ZnTe crystals, which allow one to determine the real and imaginary components of the dielectric response over a broad spectral window exceeding 1 THz. Hence, when the Drude model is applicable, THz spectroscopy can be used to simultaneously characterize the two key parameters associated with electrical conductivity, the plasma frequency and carrier scattering rate. Values for the carrier mobility μ and the charge concentration N then follow immediately if the effective mass of the carriers is known.

Lorentzian oscillator

In addition to the free-carrier response described above, a second distinct type of THz response frequently observed is that with a resonance at a finite frequency. The THz spectral regime covers many fundamental excitations including rotations, vibrations and low-lying electronic transitions in molecules and collective modes in condensed matter such as phonons, plasma, magnons and energy gaps associated with superconductivity [6, 103] as well as intra-excitonic transitions for excitons [115, 122]. A response with a resonance at finite frequencies, as will be shown in the remainder of this review, also occurs for a number of other situations, including effective medium type response [59, 196, 25], plasmon-type response [160], Drude-Smith response [189] and response associated with 'dispersive' transport [41].

Here we present the simplest description of response at a finite frequency, the Lorentz oscillator (given by the scattering rate). This is a direct generalization of the Drude model including a response at a finite frequency and follows from the generalization of Eq. 1.8 to include a restoring force. The dielectric function thus can be described by the following expression:

$$\epsilon = \epsilon_\infty + \frac{A}{\omega_0^2 - \omega^2 - i\omega\gamma}, \tag{1.10}$$

where A is the amplitude, ω_0 denotes the resonance frequency, and γ defines the width of the resonance. Fig. 1.8 illustrates the corresponding response as measured over a finite spectral range for different parameters. Applications of this treatment will be discussed below.

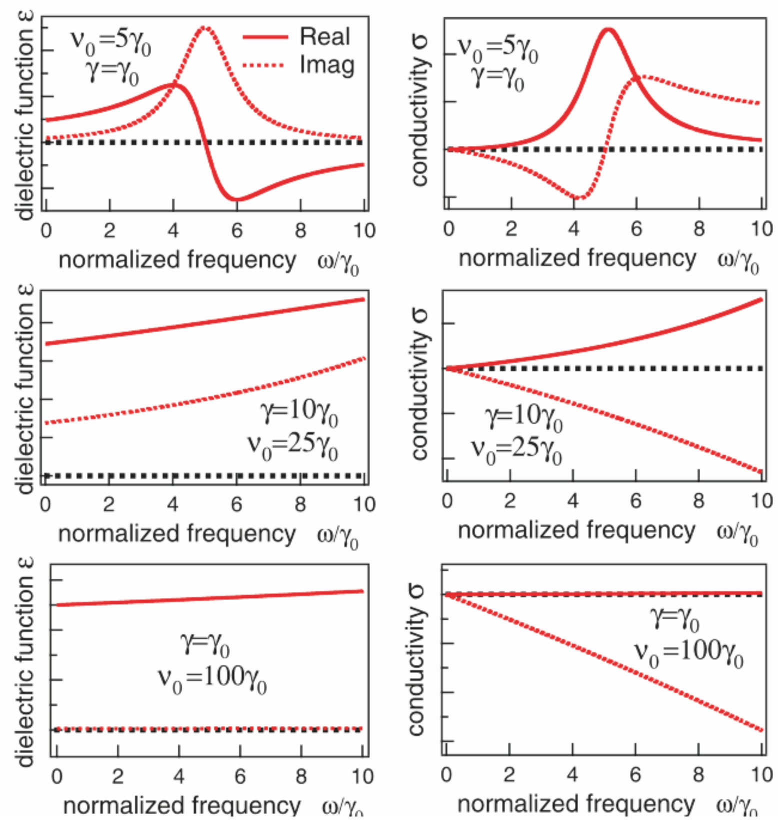

Figure 1.8: Resonant response with different linewidths and resonance frequencies relative to the probe frequency window. Upper row: complex dielectric response and conductivity for fully resonant response; middle row: the low-frequency side of the resonance; lower row: completely off-resonant response. All solid (dotted) lines indicate real (imaginary) part of the response. Black dotted lines indicate zero point. γ_0 is a frequency unit. All frequency axes are normalized for γ_0. The dielectric response has been displaced by $-\epsilon_\infty$ for clarity.

1.4.2 Bulk semiconductors

Free carriers

THz-TDS allows one to measure both the amplitude and phase (or, equivalently, both the real and imaginary parts) of the material response over a wide range of frequencies. In semiconductors where charge carriers are free to move in the conduction or valence band, the complex THz response data can often be described by the Drude model. The two key conduction parameters, the plasma frequency and scattering rate, [8, 78, 74] can then be determined by simultaneously fitting both the real and imaginary part of the frequency dependence of the conductivity.

This ability of THz spectroscopy to independently determine both scattering rates and plasma frequencies has proven particularly useful in recent work that assessed the efficiency of impact ionization processes in the low-bandgap semiconductors PbS and PbSe [170]. Impact ionization refers to a mechanism in which a photon possessing an energy of several times the bandgap is able to convert its excess energy into the generation of more than one electron-hole pair. The terahertz response was measured following optical excitation at photon energies ranging from the infrared (close to bandgap) to the ultraviolet. By verifying the uniformity of the scattering rate for all pump wavelengths and fluences, one is assured that the plasma frequency, and hence the signal amplitude, is directly proportional to the charge carrier density. The number density of absorbed excitation photons can be determined separately. Combining this quantity with the photogenerated charge carrier density inferred from terahertz measurements, one can directly determine the efficiency of impact ionization, measured in electron-hole pairs per photon. The results indicated that the impact ionization efficiency is rather low (it takes a photon energy of $\sim 7E_{gap}$ to produce two, rather than one, electron-hole pairs). However, compared to the efficiency of this process in quantum dots (QDs), the impact ionization efficiency is larger in bulk materials than in QDs *for a given photon energy*. This is in contrast to previous expectations that quantum confinement would lead to an enhancement of impact ionization.

In an older publication, a similar study had been undertaken on PbS [188], based on device measurements. The results showed a lower impact ionization efficiency. Contrary to the THz measurements, device measurements to determine impact ionization efficiencies rely on photocurrent measurements [16], which require charges to move over large distances on long timescales. As a result, recombination losses such as Auger recombination and trapping at surface defects can introduce uncertainties in the assessment of inherent carrier multiplication efficiencies in devices. In THz studies, the carrier density is determined picoseconds after photo-excitation, thus excluding the influence of all but the fastest trapping and recombination processes.

Although the Drude model has been successfully applied in many instances where the frequency dependent conduction was determined, there are several examples in which a description of the electron response requires more refined models.

For instance, the conductivity of n-type and p-type doped silicon samples at low charge densities deviates significantly from the Drude form in the THz spectral range. The data can, however, be fit by the Cole-Davidson model [88, 89]:

$$\sigma = \frac{\sigma_{DC}}{(1 - i\omega\tau)^{\beta}} \tag{1.11}$$

where the parameter $\beta \neq 1$ describes the deviation from the Drude behavior and can be considered a measure of the departure from a carrier response characterized by a single scattering time. For low doping densities the data could be described with $\beta \approx 0.8$. Only at charge densities above 10^{17}cm^{-3}, a fit with $\beta = 1$ was obtained, hence recovering the Drude model.

A second example where Drude should be handled with care is for very high charge densities. In these regimes scattering events between electrons and holes can no longer be neglected, and the scattering time and hence the mobility decrease with increasing charge density. This effect is most pronounced in materials with a small (real) dielectric constant ϵ' since charge carriers are less effectively screened from each other. For instance in silicon (small ϵ') a hundredfold higher charge density from 10^{21} to 10^{23} m^{-3} leads to a reduction of the scattering time by roughly the same amount, while in titanium dioxide (large ϵ') the same increase has barely any effect on τ [74]. We note that, even when electron-hole interactions become important, the dispersion of the conductivity may still appear Drude-like; the Drude parameters will be modified, however.

Another limitation in the applicability of the Drude model can be found in the limit of very strong electron-phonon interactions. For relatively weak electron-phonon interactions, one can consider electrons to exhibit their band mass, but to scatter by emission of absorption of a phonon. As the electron-phonon interaction becomes strong, it becomes appropriate to consider a local deformation of the lattice around a charge carrier. The free electron approximation basically assumes a rigid lattice. In reality the electric field exerted by a charge carrier displaces the lattice ions in its vicinity, forming a polarization field around it. The charge carrier and its accompanying lattice deformation result in the formation of a quasiparticle, the polaron [34, 120]. The degree of coupling scales with the lattice polarizability and is measured by the Fröhlich constant α, which characterizes the electron-phonon coupling energy in terms of the phonon energy [52]. The potential well created by the polarization field hinders the movement of the polaron since it has to "drag" the field along: the charge carrier is dressed with phonons. This results in an increased effective mass of the carriers, termed polaron mass. For sufficiently weak coupling ($\alpha \ll 6$) the wavefunction of the carrier remains extended (large polaron) and coupling merely increases the polaron mass, but leaves its transport Drude-like in nature, as THz-TDS measurements on sapphire have shown [185]. For $\alpha \gg 6$ the potential well is deep enough to localize the carrier wave function, i.e., trap the charge (small polaron formation). In this limit transport can only occur via tunneling or hopping and the conductivity is not expected to follow Drude behavior.

Hence, charge carrier transport can in principle be divided into two idealized cases: coherent, band-like transport in delocalized states when intersite coupling is large and incoherent hopping transport from one localized state to another, characterized by low intersite coupling. In addition to different types of response (Drude-like vs. non-Drude like), a second way to distinguish the two types of response is through the temperature dependence of the charge carrier mobility. While the mobility is generally thermally activated for hopping processes, i.e. it increases with temperature, it generally decreases with temperature in bandlike transport due to increased carrier scattering with phonons at elevated temperatures. In many complex materials this distinction might be an oversimplification since several types of charge transport mechanisms can occur on different time and length scales in a single material. This is particularly true for organic semiconductors where one often has to distinguish between intramolecular and intermolecular transport, both of which are strongly influenced by the sample morphology.

Excitons

Electrons and holes created after photoexcitation across the bandgap are not necessarily fully decoupled from each other. The attractive Coulomb force between them may lead to the formation of excitons, i.e. bound electron-hole pairs, particularly at low temperatures and for low-dielectric materials, in which screening of the charges is relatively inefficient. The binding energy associated with excitons lies generally in the 1 - 100 meV range. Akin to the Bohr hydrogen model, intra-excitonic transitions are formed, which are typically a fraction of the binding energy [122, 116, 120]. The low-energy structure of the exciton is thus similar to the one found in strongly confined quantum dots, which is sketched in Fig. 1.11.

The existence of excitons in a semiconductor has important implications on its electric properties. While an electric field acting on free charge carriers is capable of inducing a preferential drift and hence can produce an electric current, bound electron-hole pairs are merely displaced and no net force can be exerted. In a solar cell, for instance, this implies that photogenerated electron-hole pairs that are excitonic in nature are effectively bound and cannot contribute to the photocurrent. The identification and characterization of excitonic populations is therefore of practical importance.

Excitons may have signatures in the optical spectrum as sharp lines that are red-shifted from the electronic bandgap by their binding energy. Photoluminescence and absorption measurements of these peaks have traditionally provided the means to identify excitons. Their quantitative and unambiguous assessment is however not straightforward. Due to momentum conservation luminescence can only be observed from excitons with a total momentum close to zero, especially in the case of small exciton-phonon coupling. So-called "dark" excitons with a forbidden dipole-moment for interband transitions are commonly not accessible with visible or near-IR probes either, apart from more sophisticated techniques such as two-photon excitation spectroscopy [207]. An additional complication may be noted from recent calculations and experiments, which have shown that emission from the alleged exciton resonance can originate from an unbound electron-hole plasma as well [117, 54].

A direct way to monitor excitons that does not rely on probing interband transitions is therefore desirable. THz spectroscopy can detect excitons, both through resonant interactions with internal exciton transitions, or through a non-resonant interaction, i.e. through the polarizability associated with the electron and hole wave functions of the exciton. The first case would result in a response akin to the one depicted in the upper panel of Fig. 1.8, whereas the latter one would be reminiscent of the lower panel in the same figure. Observations of both cases, including the dynamics of condensation and ionization of excitons, have been reported [100, 72, 102, 198].

1.4.3 Confined semiconductors

The ability to characterize electrical properties in a noncontact fashion with sub-picosecond temporal resolution is necessary in the field of nanoscale electronics and optoelectronics, where it is very challenging, if not impossible, to use conventional probes. In this section, we distinguish two types of nanostructured semiconductors: those where electrons and holes are present as free charge carriers, albeit impeded in their movement, and those where quantum confinement effects dominate the response of the carriers. The former class of materials are relatively large semiconductor structures with sizes of several nm to $\mu\mathrm{m}$, such as sintered oxide particles. The latter includes quantum wells, quantum dots and graphitic nanostructures.

Structures without quantum confinement: localization and plasmons

Pure crystalline semiconductors with high charge carrier mobilities constitute the main ingredient for most microelectronic devices. Such high degrees of crystallinity and purity are however often not desired or feasible due to cost considerations: low-cost thin films of amorphous silicon find, for instance, widespread use in thin-film transistors in the backplane of liquid-crystal displays. In solar cells, amorphous silicon can be processed as cost-saving thin-films, because, owing to its direct bandgap, it exhibits a larger absorption as compared to its crystalline counterpart with indirect bandgap. Porous oxide nanoparticles form the main constituent in Grätzel-type solar cells [162]. Also, short lifetimes of optically excited charge carriers due to high defect concentrations can be beneficial in certain optoelectronic devices.

It is therefore apparent that "real-life" electronic materials can be found in varying compositions and structural appearances. Ultimately, their electronic properties on the nanometer scale, to which THz spectroscopy is particularly sensitive, depend on the degree to which delocalized "ideal" charge transport is disrupted and charge carriers become localized. In the terahertz probe window the combined response of delocalized and localized charge carriers can lead to intricate spectra. Chapter 3, for instance, deals with THz measurements on free-standing silicon nanowires on a silicon substrate where the measured conductivity is comprised of a mix of delocalized carriers in the substrate and charge carriers in the nanowires whose conductivity response is altered due to the reduced material dimensions. The interpretation in terms of a meaningful microscopic charge transport picture remains challenging. In this section we shall introduce how these effects emerge and how they affect the THz response.

The study of the effects of disorder on conductivity has a rich scientific history. Generally, there are two regimes of interest: in the "weak" localization, electron motion is still considered diffusive, but electron wave interference caused by coherence after scattering from defects, introduces small deviations from the Drude conductivity. Such effects, first considered by Abrahams *et al.* [1], generally only occur at low temperatures in conducting materials. "Strong" localization [3] occurs when the degree of randomness of the impurities or defects is sufficiently large to significantly slow down diffusion. A large number of conductivity models have been developed to describe effects due to strong localization. The most well known of these are the variable range hopping model introduced by Mott [145, 146], which describes thermally assisted hopping between localized electron sites, and phonon-assisted tunneling of electrons [2], both of which are valid when electrons hop or tunnel a distance greater than the average impurity separation. The Drude - Smith model [189], because of its very general applicability, is a common choice for describing localization effects in THz measurements. The Drude-Smith expression for the frequency dependent conductivity reads:

$$\sigma(\omega) = \frac{\omega_p \tau}{1 - i\omega\tau} \left[1 + \sum_{j=1} \frac{c_j}{(1 - i\omega\tau)^j} \right] \tag{1.12}$$

This model was, among others [139], developed to describe material systems in which long-range transport is suppressed by disorder. It lifts the constraint of the Drude model that charge carriers scatter isotropically, i.e. that their momentum randomizes completely. Instead, charge carriers are allowed to scatter in preferential directions by introducing a persistence of velocity parameter c which can have a value between 0 and -1. It is implemented for every scattering event j in the series term in the bracket of equation 1.12. A key assumption of the model is that the persistence of velocity is retained for only one collision, i.e. only the first scattering event $j = 1$ is considered. Despite this crude approximation, this simple empirical model works remarkably well. It can reproduce the signatures characteristic for charge carrier localization. Fig. 1.9 (a) and Fig. 1.9 (b) show the real and imaginary parts, respectively, of the Drude-Smith response for varying values of c. $c = 0$ yields the common Drude response. A more negative c-value increasingly depresses DC conductivity and shifts the oscillator strength to higher frequencies. For $c = -1$, the DC conductivity vanishes completely and the conductivity maximum occurs at $\omega\tau$=1. The disappearance of the DC conductivity is intuitive, for the introduction of complete carrier localization in that case prohibits long-range transport. The Drude-

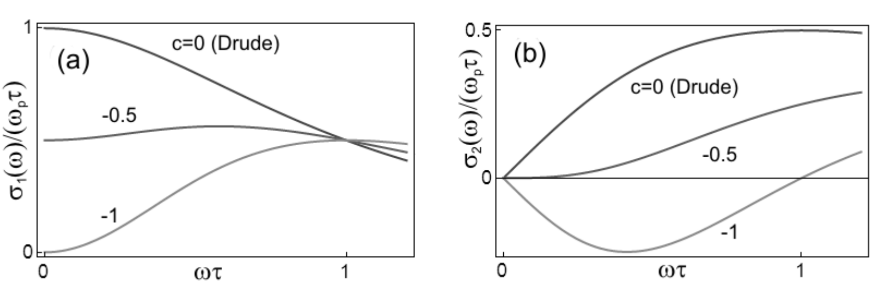

Figure 1.9: Real part (a) and imaginary part (b) of conductivities delivered by the Drude-Smith model for various values of c - both versus frequencies normalized to $\omega\tau$.

Smith model is applied in chapter 4 to describe the THz conductivity in large colloidal nanoparticles

One must note one caveat when describing the THz conductivity in nanocrystalline materials which are described by a spatially varying conductivity. Such inhomogeneous materials must be treated differently from those that contain large numbers of microscopic local defects, such as impurities or grain boundaries, which are evaluated using scattering theories [196]. This is because a far-field THz measurement reflects an averaged conductivity of a spatially varying material and one has to link the *local* conductivity in nanocrystalline materials to the *average* conductivity obtained by far-field THz measurements. In other words, it is not only the change in local dielectric response that determines the overall dielectric response, but also the contrast in the dielectric response between the material of interest and its surroundings for the unexcited system. To make the connection between the local, spatially varying conductivities and averaged conductivities measured in the far-field, requires an effective medium theory, such as those proposed by Maxwell-Garnett [59] and Bruggemann [18]. The problem of relating the far-field response to the local conductivity is however abated when the dielectric response of the nanomaterial and the surroundings are identical.

Another cause for the modification of the THz response of inhomogeneous semiconductors is related to the excitation of plasmons. Bulk plasmons are quantized, longitudinal oscillations of charge which occur in a plasma near the plasma frequency ω_p. In a homogeneous, 3-dimensional material, one cannot couple optically to plasmon modes with a transverse electric field of a plane wave light source, and plasmon modes manifest themselves as nodes, rather than resonances, in the bulk dielectric function of a conductor [118]. Surface plasmons, first predicted by Ritchie in the 1950s [176], are plasmons which are confined to interfaces between conductors and dielectrics. As is the case for bulk plasmons, surface plasmons at a flat metallic interface cannot be excited by plane wave light, because the wavevector of the plasmons is always larger than the wavevector of the incident light. This momentum mismatch can be overcome by scattering effects on rough surfaces [125], for which coupling to surface plasmons occurs. Similarly, in inhomogeneous conducting materials one can couple to local plasmon oscillations. Semiconductors, on the other hand, exhibit significantly lower plasma frequencies than metals [84, 85], so that one can expect coupling to THz plasmon oscillations in structured semiconductors. Such plasmon oscillations produce resonances in the effective dielectric function, similar to those expected from carrier localization effects. However, the physical origin of a plasmon resonance is very different from the single particle, localization effects described in the previous paragraphs: plasmon resonance is a many-body effect, and results in a coherent oscillation of all the conducting electrons.

To illustrate the origins of plasmon resonance, we briefly refer to the work of Nienhuys *et al.* [160], who measured THz photoconductivities of isolated silicon microspheres embedded in a polyvinylpyrrolidone (PVP) matrix. These particles were fabricated by simply grinding a silicon wafer to a powder with particle sizes between

1 and 30 μm. Since the particles were completely isolated the system lacked any pathway for long-range charge transport. It is therefore not surprising that the photoconductivities did not follow the Drude law and vanished for probe frequencies approaching zero. Notably, the spectra featured a resonance whose center frequency shifted to higher values, proportionally to the square root of the charge carrier density. One should note that the Drude-Smith model cannot account for this behavior - its resonance frequency is solely defined by the scattering time. In addition, this model would not make sense physically: given that the particle dimensions are in the micrometer range and thus much larger than the charge carrier diffusion length on picosecond time scales, the relative amount of carriers that backscatter from the surface is negligible. A hopping model is also not appropriate: *intra*particle transport is still expected to be bulk-like and *inter*particle transport - or transfer into the PVP matrix - is practically impossible. It is therefore clear that these transport models, which describe localization of single particles in an inhomogeneous material, cannot account for the behavior observed in silicon microspheres.

To understand the response it is instructive to recall that the terahertz probe acts as an oscillating electric field that displaces electrons and holes in opposite directions. Due to the restricted size of the particles, charges will accumulate at the particle boundaries and form a space charge layer at the surface. The resulting dipole moment acts as an additional force on the motion of charge carriers (depolarization field) and has thus to be included as a restoring force in the differential equation of the damped harmonic oscillator that we have introduced in section 1.4.1 to derive the Drude model. The solution gives a conductivity σ_{pl} which is essentially represented by the Drude model whose resonance frequency has shifted from zero to higher frequencies, reproducing the behavior observed by Nienhuys *et al.*:

$$\sigma_{pl} = \frac{\omega_p \tau_D}{1 - i\omega\tau_D\left(1 - s\frac{\omega_p^2}{\omega^2}\right)} \tag{1.13}$$

s denotes a scaling factor that shifts the resonance frequency depending on the particle shape [2] (in the case of spherical particles as considered here, s=1/3) and the dielectric constant of the particle and the surrounding medium (which were neglected in this study). One should note that Eq. 1.13 is a Lorentzian resonance (introduced in Section 1.4.1, Eq. 1.10), defined in terms of conductivity, with a resonant frequency $\omega_0 = \omega_p\sqrt{s}$. Hence, the resonance frequency scales with the plasma frequency ω_p and hence with the square root of the charge carrier density, in accordance with the measured conductivities. The plasmon model for spherical particles as considered above gives the same resonance condition (i.e. $\omega_0 = \omega_p\sqrt{s}$) as is obtained by inserting the Drude conductivity (Eq. 1.9) into Maxwell-Garnet effective-medium theory (Eq. 1.4) in the limits $\omega\tau \gg 1/\tau_D, \epsilon_m = \epsilon = 1$ and the filling fraction $f \to 0$, [73]. This is because Maxwell-Garnet effective-medium theory is derived from the Clausius-Mosotti relation [51], and therefore takes into account the local depolarization field

---

[2] For metal nanoparticles that exhibit plasmon frequencies in the visible this dependence can be nicely seen as a variation of the particle color with particle shape [150].

due to surrounding charge carriers. Indeed, it is well known that, in contrast to the Bruggemann's approximation, Maxwell-Garnet effective-medium theory reproduces plasmon resonance at optical frequencies in islandized metals [175]. Strictly speaking, Maxwell-Garnet effective-medium theory is correct only to first order expansion in f [193], and therefore gives exact results in the limit $f \to 0$. Despite this limitation, there is convincing evidence [60] suggesting that Maxwell-Garnet theory may also satisfactorily reproduce plasmon resonances observed at optical frequencies in porous/granular metals, and has been shown to produce meaningful results [65] even for materials described by $f \sim 0.5$.

In addition to the observation of plasmon resonance in isolated silicon particles described above, there have been several studies where plasmon resonance has been observed in semiconductor nanowires [166, 165, 195]. For a general review of charge carrier dynamics in semiconductor nanowires, see [171]. The diameter of most nanowire semiconductors fabricated today is larger than the exciton Bohr radius and electronic quantum confinement effects are thus not observed. Their response in the terahertz region is thus expected to be of plasmonic nature as well.

Chapter 3 of this thesis deals with a two-component material system comprised of free-standing silicon nanowires on a silicon substrate. The measured total THz conductivity of photogenerated charges is comprised of a mix of Drude response from charge carriers in the substrate and a Lorentzian-oscillator-type response from charge carriers in the nanowires. The THz conductivity of both is distinct and their discrimination thus possible and was used to identify carrier diffusion from the nanowires into the substrate.

Since plasmon resonance and carrier localization in inhomogeneous semiconductors can both result in conductivity resonances in the THz frequency region, it is often difficult to determine the physical origin of any resonance behavior in these materials. To illustrate this point we summarize below two works published in recent years which investigated the THz response of nanoporous TiO_2 films [203, 73]. These studies illustrated how one can interpret THz measurements on the same system in different ways.

First published was the work by Turner *et al.* [203], who studied the THz photoconductivity of a porous material composed from sintered TiO_2 nanoparticles (25 nm radius). The TiO_2 matrix was sensitized with photo-activated dye molecules, from which carriers were injected into the TiO_2 matrix. The photoconductivity, measured at 77K, exhibited a clear resonance in the THz spectrum. The authors interpreted this response as a localization effect, fitting their frequency dependent conductivity using the Drude-Smith model [189]. This fit yielded a mobility for the porous material of 1.5 cm^2/Vs, compared to the bulk value for TiO_2 of 56 cm^2/Vs.

A later work on a similar system by Hendry *et al.* [73] also measured the THz photoconductivity of sintered, 25 nm TiO_2 nanoparticles. There were, however, a number of subtle differences from the original experiments by Turner *et al.* Firstly, in order to remove effects due to injection, carriers were introduced by directly photoexciting an unsensitized TiO_2 with both 266 nm and 400 nm light. This means that both electrons and holes were excited in the material. By comparing directly the photoconductivity of the nanoporous material with that measured for a homogeneous TiO_2 single crystal [78] the authors were able to determine that the THz mobility of electrons in the porous sample was ~10^{-2} cm^2/Vs at 77K. The contribution from the holes was negligible due to the very large effective mass of holes in TiO_2. On increasing the temperature of the sample to 300K, a reduction in conductivity of only a factor of two (compared to a change of almost two orders of magnitude in the bulk TiO_2 material) was observed. More notably, the authors also observed a conductivity resonance in the THz conductivity of the nanoporous material. By varying the excitation intensity, the authors observed that the resonance frequency depended on carrier density, which is a strong indication of a plasmon resonance. The authors therefore employed Maxwell-Garnet effective-medium to describe the observed plasmon resonance. This model also explained the relative insensitivity of the THz conductivity to temperature, since the plasmon resonance frequency is determined only by the carrier density, and not the scattering rate.

While both Turner *et al.* and Hendry *et al.* observed similar resonances in their THz conductivity spectra of nanoporous TiO_2, two different explanations for the physical origin of the response were given: as an intra-particle, single carrier response governed by boundary scattering on the one hand, and as a Drude response buried in an effective medium on the other hand, resulting in a plasmon resonance. This illustrates how THz conductivities ought to be evaluated with care, as one essentially has to distinguish how local, single carrier properties (Drude, hopping, backscattering) and local field/many-body contributions (dielectric screening, depolarization fields) affect the overall, far field response. A proper understanding of both the local intraparticle behavior and local field effects due to inhomogeneities in the dielectric response are thus imperative.

To address the issue of local conductivity, Nemec *et al.* published several articles in which Monte-Carlo simulations were performed to calculate the conductivities of charge carriers of simplified model systems such as spherical particles of varying sizes and more realistic ones, e.g. nanoporous oxides [157, 159, 158]. Only a few parameters entered the simulation: the particle dimension d, the thermal velocity v_{th} and the carrier momentum scattering time τ (and hence the mean free path $l_f = v_{th}\tau$). The parameter p_r denotes the probability that upon scattering with the particle boundary a charge carrier is reflected back into the particle (p_r is thus akin to the c-parameter in the Drude-Smith model). The degree of localization was expressed as the parameter α, defined as the ratio between the mean free path and the particle dimension. The authors concluded that the shape of the conductivities only depend on α and p_r for simple spherical particles.

It was further shown that the aforementioned Drude-Smith model bears a good resemblance to the calculated spectra and can thus be used as a reasonable approximation to describe THz responses of simple material systems. Monte-Carlo simulations however allow including more realistic microscopic boundary conditions such as electric field gradients or potential barriers that influence charge transport locally - something the purely phenomenological Drude-Smith model is not capable of. Nevertheless, the spectra calculated by Monte-Carlo simulations still represent *local*, single-carrier properties of the material. In order to obtain the effective response of the whole system one would still have to either incorporate carrier-carrier interactions into the calculation (or alternatively apply an appropriate effective-medium theory). One can still consider, in a very general manner, the effects that carrier-carrier interactions would have: for a nanoporous material in which the interparticle transport is inefficient (i.e. one which exhibits a localized, single particle conductivity resonance), carrier-carrier interactions would introduce an additional restoring force for carriers near the interface, pulling them towards the center of the particle. Such a restorative effect would shift the spectral weight of the low-frequency, localized resonance, to higher frequencies (see section 1.4.1). This means that on increasing the strength of carrier-carrier interactions (by increasing the carrier density) one can expect to observe the evolution from a localized resonance to plasmon resonance in the same material. This problem of resolving plasmon resonance from localization effects is obviously not restricted to TiO_2 but can also occur in other nanostructured materials that possess domain dimensions comparable to the carrier mean free path.

Structures with quantum confinement

The previous section dealt with nanostructured semiconductors in which the typical dimension of the carrier de Broglie wavelength remained small compared to the physical dimensions of the semiconductor nanostructures. The effects of quantum confinement take place when the size of a system or structure approaches the de Broglie wavelength of the charge carriers (electrons or holes) in one, two, or all three dimensions. Such a structure is referred to as a quantum well (QW), quantum wire or nanowire, and quantum dot (QD), respectively. The electronic and optical properties of these structures deviate substantially from those of their bulk counterparts [69]. Typically, this quantum confinement leads to discrete energy states of carriers (in analogy to a quantum mechanical particle in a box) and, depending on the confinement dimensionality, to various other effects like change in bandgap energy or exciton binding energy [71, 56, 30]. This behavior will affect the THz response; inversely, the THz response can be used to characterize confined charge carriers. Here,

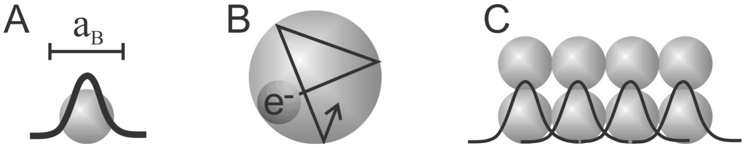

Figure 1.10: Different regimes of charge carriers in Quantum Dot (assemblies): (A) in the limit of strong confinement, the QD radius is smaller than the exciton Bohr radius and strong confinement occurs. (B) for weak confinement, charge carriers can move within the confined space of the nanocrystal. (C) for QD assemblies, electronic coupling between adjacent quantum dots (owing to the finite overlap of charge carrier wavefunctions) allows for finite electrical conductivity over macroscopic distances.

we will only elaborate on 0D nanostructures, i.e. quantum dots, since Chapter 4 deals with such. It is however noted that a large number of publications have reported on THz measurements on other types of quantum confined nanostructures such as quantum wells, carbon nanotubes and graphene [205].

Quantum dots (QDs) are semiconductors with charge carriers confined in all three dimensions [69, 42]. In QDs the electron and hole energy states become discrete due to the 3D spatial confinement. As a result, QDs have optical responses very different from the bulk material from which they are made. What is more, the QD optical response is tunable: by varying their size (and therefore degree of electronic confinement) the band gaps of QDs can be modified and tuned to cover the entire visible to near-infrared spectral range [211]. As such, they are promising materials for a variety of electro-optic applications, such as LEDs and photovoltaic devices. Knowledge of the processes immediately following photo-excitation is therefore essential, and there has been much interest recently in exciton dynamics in QDs ([119] and references therein), especially in exciton decay, exciton cooling, multi-exciton dynamics, and the possible formation of multi-excitons by carrier multiplication.

Many studies of carrier dynamics in semiconductor quantum dots have been performed using ultrafast optical spectroscopy [119]. Most of these studies, typically based on transient absorption or time-resolved fluorescence, have focused on interband transitions in the optical range. The observed optical dynamics in the visible are dictated by both electron and hole dynamics. Infrared transient absorption measurements have been used to study specifically electron dynamics by probing electron intraband transitions. As will be shown in the following, THz spectroscopy has proven to be a very fruitful approach for the study of exciton and carrier dynamics in quantum dots and quantum dot assemblies.

In quantum dots, the spacing of the discrete electron and hole energy levels is strongly dependent on the size of the quantum dot. The two relevant length scales of the problem are the QD radius R and the exciton Bohr radius a_B that is the natural physical separation in a bulk crystal between an electron in the conduction band and its corresponding hole in the valence band. Strong confinement in small QDs ($R < a_B$, see Fig. 1.10 (a)) results in high confinement energies and relatively large energy spacing between the levels, while larger QDs have more closely spaced energy levels. For even larger QDs ($R \gg a_B$, see Fig. 1.10 (b)), the confinement is weak, and charge carriers can move within the boundaries of the QD volume. For assemblies of quantum dots, the electron/hole wavefunctions between different QDs can couple, and energy and charge transfer can occur within the system (Fig. 1.10 (c)). For the latter case, THz-TDS is very sensitive to the degree of electronic coupling between the quantum dots. Strong coupling will allow electrons or holes to "hop" between QDs, giving rise to a real component of the complex conductivity (or equivalently an imaginary component of the permittivity/susceptibility) even at frequencies below the intraband transitions of isolated QDs. Such a component would be absent in isolated particles in the strong confinement regime.

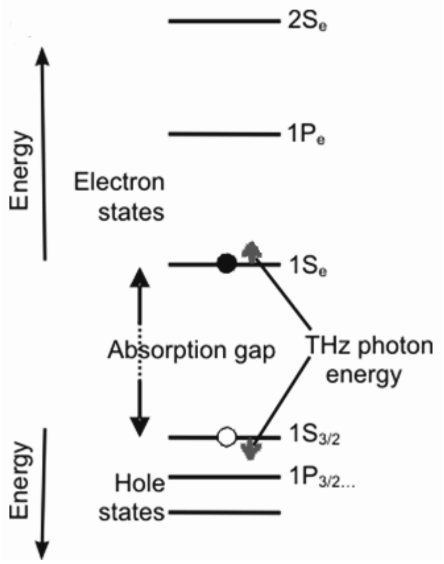

Figure 1.11: (a) Energy level scheme for a QD in the limit of strong confinement. All transitions occur at energies exceeding that of the low-frequency THz spectrometer (smallest arrows). As a result, the excitonic transitions are interrogated off-resonantly.

In the limit of strong confinement, the energy level spacing depends on the degree of confinement, but also on the band masses of the electrons and holes: a rule of thumb is that the heavier the quasi-particle the more closely spaced the energy levels. In quantum dots made of II-VI materials such as CdSe, the hole band mass is several times that of the electron, so that the valence electronic levels are more closely spaced than the electron levels (see Fig. 1.11 (a)).

THz spectroscopy was first used to investigate the nature and dynamics of photoexcitations in semiconductor quantum dots by Beard *et al.* [9], for colloidal CdSe quantum dots of various sizes. The authors note that for NPs in the strong confinement regime ($<$ 5 nm diameter), the photoinduced change in the THz dielectric function is purely real (finite imaginary conductivity; zero real conductivity) and the magnitude increases with the fourth power of the particle radius.

The origin of such a response (purely real dielectric response of photo-excited QDs) was subsequently revealed by Wang *et al.* [208] and [28]. These authors argue that for QDs with strong confinement, both electrons and holes occupy discrete energy levels separated by at least tens of meV [42], i.e. energies significantly larger than the photon energies used to probe the levels (1 THz = 4 meV) - see Fig. 1.11 (a). This means that THz photons with energy below the intraband transitions interact non-resonantly with electrons and holes. The non-resonant nature of the interaction dictates that no absorption of THz light can occur, which explains the experimental observation of a photoinduced change in the THz dielectric function that is purely real (imaginary conductivity). The amount of photoinduced increase in the dielectric response can be directly related to the polarizability (α) of the exciton.

In a QD, the energy levels of electrons and holes scale with the quantum dot radius R as $\propto R^{-2}$, while the Coulomb interaction scales as $\propto R^{-1}$. In the limit of strong confinement, i.e. small R, the confinement energies far exceed the Coulomb interactions and the electron and hole comprising an exciton are therefore largely uncorrelated [42]. Consequently, one can treat the exciton polarizability as the sum of separate contributions from the electron and the hole. The polarizability is a measure of the extent to which the electron and hole wavefunctions are deformed in an applied electric field. This deformation requires mixing of higher lying states, and occurs more readily when these states are energetically close by. Owing to smaller energy-level spacing, the hole therefore dominates the polarizability at frequencies below the intraband transition energies, giving rise to a real and spectrally flat susceptibility (or dielectric constant, see Fig. 1.8, lower panel). Typically, the magnitude of the hole polarizability is around $10^4\,\text{Å}^3$, scaling approximately as $\alpha \propto R^4$. A more detailed analysis, taking into account the non-parabolicity of the electronic bands and the electron-hole interaction, yields $\alpha \propto R^{3.6}$. Subsequent studies on PbSe quantum dots [28] revealed that similar conclusions can be drawn for PbSe QD systems. However, the THz response is no longer dominated by the holes due to the comparable band masses of electron and hole and corresponding similar level spacing for conduction and valence states in lead salts.

Chapter 4 of this thesis deals with an extensive study on the transition between the strong confinement, characterized by the abscence of THz absorption, and the intermediate confinement, where THz absorption is observed, in isolated colloidal CdTe nanoparticles. Backed up by tight-binding calculations which take into account electron-hole correlations and the band structure, we were able to follow this transition.

2

Electron recombination dynamics in nitrogen-doped diamond

We report on the carrier dynamics and recombination pathways of photogenerated electrons in type Ib synthetic diamond using ultrafast spectroscopic techniques. Samples with controlled amounts of nitrogen defects were grown using the high-pressure high-temperature (HPHT) method. Electrons were excited from single substitutional nitrogen defects into the conduction band via an ultrashort pulse from a frequency-doubled Ti-sapphire laser. Using time-resolved terahertz time-domain spectroscopy, we determined the mobility of the photoexcited electrons and monitored their recombination dynamics, at temperatures ranging from cryogenic temperatures to room temperature. The electron mobility was observed to be limited by scattering with neutral nitrogen impurity defects (N_s^0). Electrons were observed to predominantly recombine into neutral nitrogen states rather than their original ionized nitrogen defects, thereby creating negatively charged nitrogen states (N_s^-). The creation of N_s^- states is confirmed experimentally by tracking the localized vibrational modes (LVM) of nitrogen defects during the electron recombination process using visible pump-infrared probe transient spectroscopy. We observe a transient infrared absorption feature at 1349 cm^{-1} that can be assigned to the LVM of N_s^-. Density functional calculations are carried out to determine the LVMs of nitrogen in various charge states, and we find a $\sim 10\mathrm{cm}^{-1}$ upward shift of the mode on passing from N_s^0 to N_s^-, in agreement with experimental observations.

2.1 Introduction

Diamond is a versatile material that shows exceptional promise in a range of optical, quantum optical, and electronic applications [197, 201, 213, 86]. There are two main methods by which synthetic diamond may be grown: high-pressure high-temperature (HPHT) synthesis and chemical vapor deposition (CVD). In both cases, the dominant impurity in diamond is single substitutional nitrogen (N_s), which is known to act as a deep donor approximately 1.7 eV below the conduction band [80].

The optoelectronic transitions associated with the Ns defect have important implications for several potential applications of diamond. First, N_s defects act as electron traps, thereby significantly limiting the performance of diamond-based devices that may potentially be used as detectors or for high-power electronics. Understanding the influence of traps on relevant figures of merit of charge carriers such as their mobility and lifetime is thus important. Second, the negatively charged nitrogen vacancy defect (NV^-) is currently being intensively studied for spintronics [12, 87]. The existence of this defect is dependent on electrons being donated from single nitrogen to neutral nitrogen vacancy (NV) defects. One of the most significant issues with NV^- centers as stable quantum emitters is the phenomenon of "blinking" which may be a result of instability in the charge state of the NV defect. Previous theoretical studies [97] have suggested that N_s may act not only as an electron donor, which is intuitive given its valency, but also as an acceptor. If so, this would have important implications, for example, to compensate phosphorus donors, which may be incorporated into CVD synthetic diamond to produce n-type devices [123] and potentially also to convert NV^- centers back to their neutral state. However, there has been no experimental evidence for the electron-accepting property of N_s so far, i.e., for the possibility that N_s defects become negatively charged. This is likely due to the challenge of detecting this state spectroscopically; it is presumably unstable and thus short lived. Time-resolved techniques that are able to probe electron and defect-charge dynamics on ultrafast time scales can potentially offer a means to achieve this goal.

In this study, we report on the transport properties and picosecond time scale relaxation dynamics of electrons excited from N_s defects into the conduction band in HPHT-grown type Ib diamond. The investigated samples contain a controlled concentration of N_s defects of the order of hundreds of parts per million and negligible amounts of other unintentional dopants. Using time-resolved terahertz spectroscopy, we measure the mobility of the donor-excited electrons and the time scale of their back-recombination from the conduction band as a function of N_s concentration, ionized impurity density, and temperature. The recombination dynamics show a clear dependence on the neutral rather than the ionized impurity concentration, suggesting that electrons do not only relax back into the photoionized defects but also into neutral N_s states. This strongly suggests that N_s can act as an acceptor state, forming negatively charged N_s defects (N_s^-). The presence of this remarkable relaxation channel is confirmed by independent measurements on the same diamond samples using time-resolved infrared spectroscopy with which we probe the localized vibrational modes (LVM) of defects within diamond. Here, the appearance of negatively charged nitrogen defects following optical excitation manifests itself through a transient IR absorption feature of the LVM at 1349 cm^{-1}. Density functional theory calculations confirm this assignment.

2.2 Methods

Standard high-pressure high-temperature (HPHT) grown type Ib synthetic diamond samples were investigated in this study. As-grown HPHT synthetic diamond material from three different growth runs was processed into thin plates of dimensions of approximately 5x5x0.5 mm, using laser sawing and polishing. Each plate possessed a main face corresponding to the {100} surface. For all of these samples, the central region of the main face corresponded to the {100} growth sector, and only this sector was probed in the experiments reported here.

By performing room temperature UV-visible absorption measurements on these samples and comparing the resulting absorption spectra to that of a diamond sample with a known neutral single substitutional nitrogen (N_s^0) concentration [31], it was possible to determine the N_s^0 concentration of the central growth sectors. We investigated three samples with concentrations of 100, 150, and 300 (±10) ppm, respectively. The central {100} growth sectors are expected to possess negligible concentrations of other defects, besides single nitrogen.

Time-resolved terahertz time-domain spectroscopy as a probe of charge carrier dynamics has been described extensively in the literature [90, 205]. The setup used for this experiment utilizes an amplified Ti:Sapphire laser operating at a repetition rate of 1 kHz, delivering pulses with a duration of 150 fs and an energy of 1 mJ at a wavelength of 800 nm. Ninety percent of the output energy is split off and used as the excitation pulse by frequency doubling it to a wavelength of 400 nm (3.1 eV) with a Beta barium borate (BBO) crystal. The remaining output is used to generate and detect terahertz radiation. The terahertz radiation is generated via optical rectification in a 1-mm-thick ZnTe crystal and detected via electro-optic sampling in a second ZnTe crystal of the same dimensions [151]. A cryostat (Oxford Instruments, Optistat AC-V12) is used to cool the sample to temperatures down to 10 K. The generated terahertz probe spectrum covers a broad frequency range spanning from 0.3 to 2 THz. One particular feature of the electro-optic detection method is that it works in the time domain, i.e., it records the time-dependent electric field of the terahertz probe pulse, rather than the time-integrated intensity. As opposed to most conventional spectrometers based on intensity measurement, this implies that not only the absorption spectrum of the sample can be detected. Also changes in the phase can be resolved over the whole pulse bandwidth. As a result, not only the absorption but also the refractive index changes of the investigated material can be inferred, i.e., the complete complex refractive index. By modulating the excitation beam with an optical chopper and recording the difference signal using a lock-in amplifier, we determine the excitation-pulse-induced terahertz response, i.e., the change of the complex index of refraction of diamond due to the presence of photoexcited charge carriers.

The setup for the visible pump-infrared probe measurements is driven by another amplified Ti:Sapphire laser system. It delivers pulses with durations of 50 fs and energies of 3 mJ. Thirty percent of the output is split off and frequency doubled in a BBO crystal to photoexcite the sample with light at a wavelength of 400 nm (3.1 eV). The remaining output is used to drive an optical parametric amplifier (OPA), after which the midinfrared probe light is generated by difference frequency mixing of the signal and idler beams from the OPA in a $AgGaS_2$ crystal. The probe pulse is centered at a frequency of 1340 cm^{-1} (=165 meV) and has a bandwidth of 350 cm^{-1} (=40 meV). After transmission through the sample, the probe pulse is spectrally dispersed using an Oriel MS260i grating spectrometer and detected using a 32-channel Mercury-Cadmium-Telluride (MCT) detector array.

For the calculations of the LVM, we use a spin-density functional package, as implemented in AIMPRO [98, 172] with both local density [167] and generalized gradient [168] approximations (LDA and GGA). Point defects are modeled using a supercell approach, where individual defects are approximated by a crystal of well-spaced defects. In order to estimate the impact of the periodic boundary conditions on the derived quantities, we have used simple cubic supercells of side length $3a_0$ and $4a_0$, containing 216 and 512 host atoms, respectively. The wave function basis consists of atom-centered Gaussians [63]. The charge density is Fourier transformed using plane waves with a cutoff of 350 Ry, yielding well-converged total energies. Core electrons are included through norm-conserving pseudopotentials [70].

Within the LDA and GGA approaches, the lattice constant and bulk modulus of bulk diamond are reproduced well in comparison to experiment. In the LDA (GGA) a_0 is underestimated (overestimated) by $\sim 1\%$ (0.2%), and B_0 is overestimated (underestimated) by 6% (0.5%). The calculated direct and indirect band gaps agree with published plane-wave values [135], and the basic methodology has been tested on many defects in diamond [61] and other materials.

In all cases we sample the Brillouin zone using the Monkhorst-Pack scheme [143], a 2x2x2 for the 216 atom cells, and a Γ-point approximation for the 512 atom cell. These correspond to sampling densities of 0.025 and 0.085 points per $Å^{-3}$, respectively. For the simulation of vibrational modes, the second derivative of the total energy with respect to displacement of the atoms is obtained using a finite difference approximation using the analytic forces. A quasiharmonic dynamical matrix is then built in the usual way, and diagonalization yields vibrational frequencies. For each supercell size, the frequencies have been obtained (a) under the constraint that the lattice constant is that of the corresponding defect-free supercell and (b) where a zero pressure boundary condition has been applied so that the lattice constant is freely varied to minimize the total energy.

2.3 Results and discussion

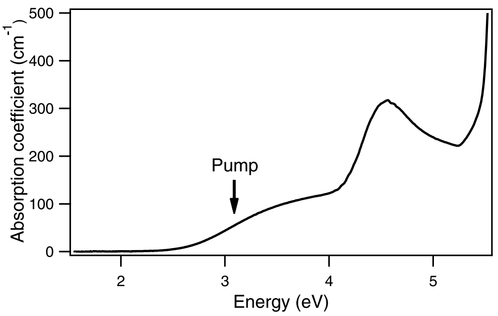

Figure 2.1: shows the absorption spectrum of the 100-ppm sample. The excitation energy of 3.1 eV is indicated with an arrow.

The absorption spectrum of the 100-ppm sample is shown in Fig. 2.1. The origin of the absorption peak at 4.5 eV (270 nm) is still under debate. One possible mechanism, as will be discussed further down, relates it to a transition between the valence band and the $\mathrm{N_s^-}$ defect state whose existence is shown in this work [97].

In all of the pump-probe spectroscopy measurements that are presented in the following, electrons are excited from neutral nitrogen ($\mathrm{N_s^0}$) states into the conduction band by pump pulses with photon energies of 3.1 eV (400-nm wavelength, indicated with an arrow in 2.1), as was shown in Ref. [80]. This creates hot electrons with initial excess energies of around 1.4 eV that subsequently relax to the bottom of the conduction band within less than 2 ps. All spectra presented here have been recorded after that point.

In the following, we express the complex index of refraction of the excited electrons measured by our terahertz spectrometer in terms of the complex conductivity. The complex index of refraction $\hat{n}$ of a material is related to the complex dielectric function $\hat{\epsilon}$ via $\hat{\epsilon} = \hat{n}^2$, The complex conductivity $\hat{\sigma}$ of the photoexcited electrons can then be derived through $\hat{\sigma} = -i\omega\epsilon_0(\hat{\epsilon} - \hat{\epsilon}_\infty)$, where ω is the angular frequency, ϵ_0 the free-space permittivity, $\hat{\epsilon}$ the dielectric constant of the photoexcited diamond, and $\hat{\epsilon}_\infty$ the dielectric constant of the unexcited diamond. In the actual terahertz mea-

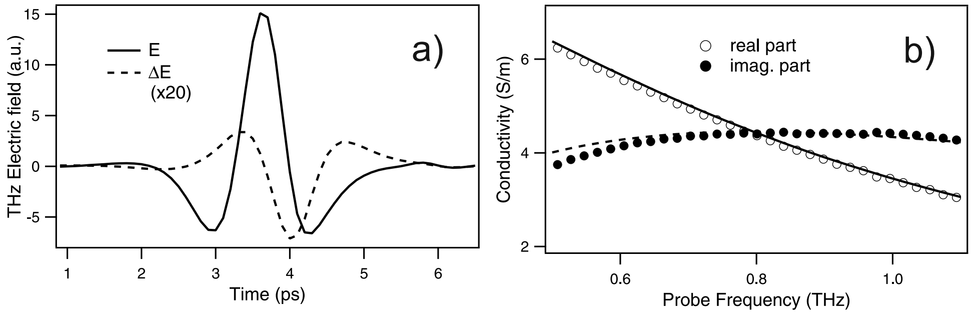

Figure 2.2: a) shows the recorded terahertz field E transmitted through the unexcited diamond sample at 200 K (solid line) and the photomodulated terahertz field ΔE (dashed line) in the time domain; b) shows the extracted complex photoconductivity in the frequency domain (circles) and the obtained fit to the Drude model that yields an electron scattering time of 200 fs (solid and dashed lines). The measurements were taken at a pump-probe delay of 2 ps.

surement, both the transmission of the terahertz probe through the unexcited sample $E(t)$ and the pump-induced transmission change $\Delta E(t)$ are recorded in the time domain, as shown in Fig. 2.2 a).

The ratio $\Delta E(t)/E(t)$ is then used to extract the complex conductivity $\hat{\sigma}(\omega)$ following the procedure described in Ref. [75]. We determined the terahertz conductivities of all three samples at different temperatures between 10 K and room temperature immediately after all electrons had relaxed to the bottom of the conduction band. Excitation fluences were chosen such that the density of the excited electron plasma was on the order of 10^{14}cm^{-3}. The conductivity spectra were fitted by the Drude model [39] - a Lorentzian oscillator centered at zero frequency:

$$\hat{\sigma}(\omega) = \frac{Ne^2\tau/m^*}{1 - i\omega\tau} \tag{2.1}$$

Here, N denotes the photoexcited electron density, e the unity electron charge, m^* the electron effective mass (taken to be 0.36 m_e, where me denotes the electron rest mass [153]), and τ the electron scattering time. The linewidth of this Drude resonance is defined by the scattering rate $1/\tau$. Figure 2.2 b) shows an exemplary Drude fit for the photoconductivity measured at 200 K, yielding a scattering time of 200 fs, which showed no significant dependence on the pump-probe delay time. It is evident from the comparison of the data with the fit in Fig. 2.2 b) that two adjustable parameters (density N and scattering rate $1/\tau$) are sufficient to accurately describe the frequency-dependent photoconductivity.

Figure 2.3 shows the extracted electron scattering times for all three diamond samples at various temperatures and their corresponding mobility values μ, related to the scattering time through $\mu = e\tau/m^*$. The excited electron density is determined by the excitation photon flux and the absorption cross section at 400 nm. The optical properties have been verified not to change significantly with varying temperature; the photon flux was kept equal for all measurements to achieve a photoexcited electron density of $3{*}10^{14}\text{cm}^{-3}$. Hence the electron density does not vary for the measurements shown in Fig. 2.3. It is further evident that as free electrons are generated through ionization of single nitrogen atoms, the density of resulting ionized, positively charged, nitrogen states (N_s^+) is

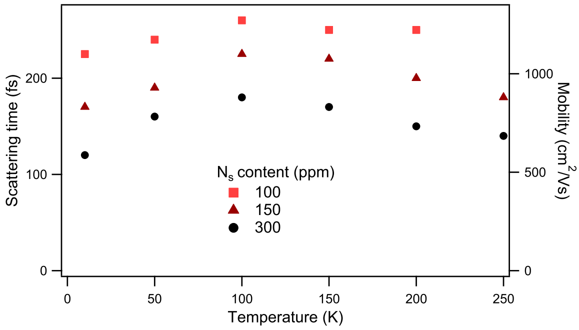

Figure 2.3: Temperature dependence of the electron scattering time τ (left axis) and mobility μ (right axis) for all three measured diamond samples possessing different concentrations of single substitutional nitrogen defects. All the data was taken at fixed photoexcited carrier density of $3 * 10^{14}\text{cm}^{-3}$ at a delay time of 2 ps after photoinjection of carriers.

equally constant. From Fig. 2.3 it is observed that the electron mobility is only weakly dependent on temperature for all three samples, with values around 1000 cm^2/Vs. More precisely, it increases by approximately 30% when the temperature is raised from 10 to 100 K, from where it decreases again by the same amount upon further increasing the temperature to 250 K. This temperature dependence of the mobility is distinctly different from the one commonly observed in high-purity diamond. In high-purity diamond, the electron mobility decreases continuously with increasing temperature. Hall measurements [173], time-of-flight [153], photoconductivity [86], and light-induced transient grating experiments [138] on such diamond samples have shown that the electron mobility follows a $T^{-3/2}$ dependence below room temperature, which is characteristic for acoustic-phonon scattering, reaching values up to several thousand cm^2/Vs at cryogenic temperatures. In doped type Ib diamond, however, other scattering mechanisms are likely to make a contribution in addition to phonon scattering, namely scattering with neutral and photoionized (positively charged) nitrogen defects. Figure 2.3 reveals that a higher N_s^0 defect concentration indeed reduces the total mobility over all temperatures measured. Because the excited electron density and thus the density of ionized impurities in these measurements were kept constant between the samples by adjusting the excitation fluence, this result suggests that the scattering contribution from neutral nitrogen defects is substantial. This is not surprising: although the scattering cross section of charged impurities is generally orders of magnitude larger than neutral ones [55], according to the excitation fluences used in our measurements, only about 1 out of 10^5 nitrogen defects is ionized. Hence the vast majority of nitrogen defects are still neutral, contributing substantially to carrier scattering. The temperature dependence of the mobility supports this picture: the simplest model to describe scattering by neutral impurities predicts that the mobility is temperature independent [46], as largely borne out by the experimental results. We note that similar behavior has been observed previously in a boron-doped diamond [202]. The contribution from scattering off ionized impurities becomes evident in our measurements at higher excitation densities (data not shown). It remains rather limited, however: an increase of the electron density by more than an order of magnitude, from $1 * 10^{14} cm^{-3}$ to $2 * 10^{15} cm^{-3}$, resulted in a reduction of the mobility by only 20%. Approaching room temperature, the scattering rate by acoustical phonons becomes comparable to defect scattering, i.e., acoustical phonon scattering is increasingly likely to contribute to the total scattering rate. This would explain the observed mobility decrease at temperatures above 100 K.

To conclude this section, our findings qualitatively suggest that the electron mobility in a N-doped diamond is predominantly limited by scattering from N_s^0 defects, with additional contributions from N_s^+ defects and acoustical phonons that become more dominant at larger N_s^+ densities and higher temperatures, respectively.

In the following, we focus on the dynamics of recombination of the photoexcited electrons from the conduction band. A discussion about the physical mechanism will follow at a later stage of this report. In order to investigate the electron recombination, we monitor the decay of the real part of the conductivity at a fixed probe frequency as a function of pump-probe delay t_{pump}. According to the Drude model, the real conductivity scales with $\mathrm{Re}(\hat{\sigma}, t_{pump}) \sim N(t_{pump})\tau$. We experimentally verified that τ does not change significantly during the recombination process by taking terahertz conductivity spectra during the relaxation process and extracting the scattering time from them. Hence, $\mathrm{Re}(\hat{\sigma}, t_{pump}) \sim N(t_{pump})$, and we can use the real conductivity as a direct probe of the time-dependent electron density.

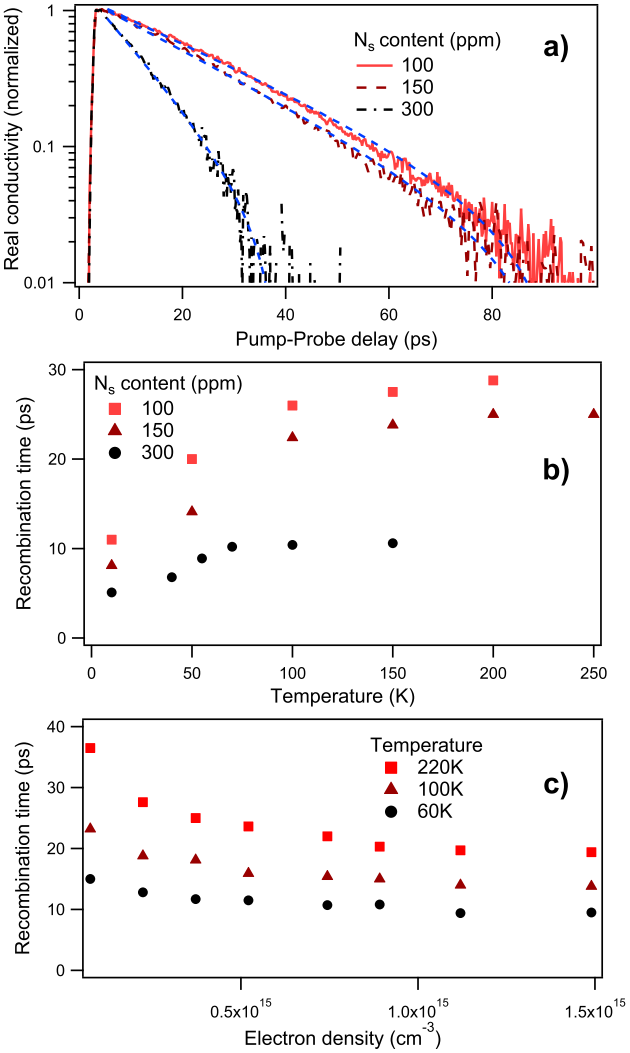

Figure 2.4: Electron recombination dynamics as measured by terahertz spectroscopy; (a) logarithmic plot of the temporal evolution of the normalized terahertz real conductivity (proportional to the free electron density) at room temperature for three diamond samples with different N_s concentrations; the slopes of the decays (obtained from single exponential fits shown as dotted lines), proportional to the recombination rate $1/\tau_r$, show a strong dependence on N_s concentration; (b) shows the temperature dependence of the extracted recombination times τ_r for all three samples (data for both graphs was recorded at fixed photoexcited carrier density of $3 * 10^{14}\mathrm{cm}^{-3}$); and (c) the dependence of τ_r on the photoexcited electron density for the sample with N_s concentration of 150 ppm at temperatures 60, 100, and 220 K.

Figure 2.4 a) shows the time dependence of the real part of the conductivity, reflecting the variation of electron density in time, for all three samples at room temperature. The photogenerated electron density, and thus the photogenerated N_s^+ density, was kept constant at a value of $3 * 10^{14} \mathrm{cm}^{-3}$. All dynamics show a modest speed-up of the decay with increasing pump-probe delay time, but the dynamics can be approximated very well by single exponential decay,which can be recognized as a linear slope in the logarithmic plot shown in Fig. 2.4 a). Electrons relax from the conduction band on a time scale of several tens of picoseconds, with a recombination time τ_r that decreases for higher N_s defect concentrations. We note that another study on type Ib diamond using a light-induced transient grating technique has recently found similar relaxation behavior related to single substitutional nitrogen [137]. The authors observed nonexponential recombination dynamics on time scales of several hundred picoseconds. However, they were using excitation pulses at a wavelength of 213 nm, which creates electrons and holes through interband excitation, which complicates the dynamics. We like to stress that the 400-nm excitation pulse employed here only excites electrons from N_s defects. Figure 2.4 b) summarizes the τ_r data for all three samples at various measured temperatures. τ_r increases with increasing temperature until it levels off at 150. 200 K. A model describing the temperature dependence of the recombination kinetics in terms of the temperature-dependent scattering rate and thermal velocity will be presented below. Remarkably, τ_r is almost inversely proportional to the N_s concentration, particularly at high temperatures: a three times larger N_s concentration reduces τ_r by a factor of 2.5 above 150 K. Since the N_s^+ density due to photoexcitation from defect states is equal for the different samples, the observed inverse proportionality between N_s and τ_r strongly suggests that most electrons relax into N_s^0 states rather than their original N_s^+ states. That would imply that negatively charged nitrogen states (N_s^-) are formed. Akin to the scattering cross section, the capture cross section of a positively charged defect is generally larger than its neutral state value [130], but again, the presence of a vast majority of N_s^0 defects would be dominant in this case. Consequently, similar to the mobility behavior discussed above, the influence of N_s^+ states becomes more pronounced at higher N_s^+ densities, i.e., higher incident fluences, also resulting in higher electron densities. Figure 2.4 c) shows the dependence of τ_r on the electron (i.e., N_s^+) density in the 150-ppm sample for three different temperatures. As expected, the relaxation time decreases with increasing electron density. Assuming a 1:1 ratio for the N_s^+: electron density, N_s^+ states are increasingly able to scavenge electrons at higher densities. However, this effect is again weaker than the dependence on the N_s^0 concentration. As can be seen from Fig. 2.4 c), a 15-fold increase of the N_s^+ density results in a decrease of τ_r by only 30 to 40%. The recombination dynamics display single exponential behavior in all cases.

To test the hypothesis that electrons mainly recombine at neutral nitrogen defects, we made use of the fact that single substitutional nitrogen defects exhibit LVM, which give rise to sharp absorption lines in the infrared part of the electromagnetic spectrum. Additionally, the spectral position of the vibrational mode depends on the charge state of the defect.

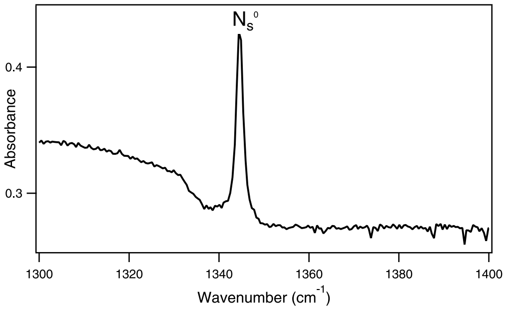

Figure 2.5: FTIR spectrum of the 300-ppm type Ib diamond sample showing an absorption peak at 1344 cm^{-1}, which is due to the LVM of N_s^0 defects.

Figure 2.5 shows a Fourier transform infrared (FTIR) spectrum of one of the investigated samples. A sharp absorption peak can be seen at 1344 cm^{-1} that is characteristic for N_s^0 defects [132]. The broad background on the lower wave number side of the spectrum is also N_s^0 related (i.e., its intensity scales with the N_s^0 resonant feature). It has been shown that N_s^+ states exhibit an absorption peak at 1332 cm^{-1} [132]. Spectral signatures of negatively charged single substitutional nitrogen states have not been observed so far. By monitoring the temporal evolution of the IR spectrum after photoexcitation, it was possible to observe time-dependent absorption changes of the vibrational modes.

Figure 2.6 a) shows the pump-induced transmission changes T/T_0 of the IR spectrum measured on the 300-ppm sample from the point of photoexcitation up to a pump-probe delay of 30 ps, with an excitation photon flux resulting in an electron density of $4 * 10^{15}\mathrm{cm}^{-3}$. In the ratio T/T_0, T is the transmission through the excited sample and T_0 the transmission through the unexcited sample. Thus, $T/T_0 < 1$ indicates pump-induced absorption and $T/T_0 > 1$ pump-induced bleaching. The broad absorption feature shown in Fig. 2.6 a) originates from the high-frequency tail of the Drude response of the excited electrons. It vanishes on a time scale that is comparable with the charge carrier decay time in the terahertz measurements. On top of this broad absorption, a variety of absorption and bleach features are visible. These features are not sample related but are artifacts due to the presence of water vapor in the setup. The vibrational modes of free water exhibit several sharp absorption resonances at the spectral positions of these features. The absorption signatures from the water vapor that the probe pulse acquires during propagation interfere with the broad charge carrier response, resulting in the observed absorption and bleach effects around these resonances. This phenomenon is somewhat reminiscent of the Fano effect [48].

Even though the measurement chamber had been flushed with nitrogen in order to reduce the humidity to close to zero, this effect could not be removed completely. Because the anticipated transient signals are on the order of 1/1000 and less and thus much smaller than the artifacts, we cannot draw any conclusions from this short-time data set regarding the presence of (charged) nitrogen sites.

Fortunately, the artifacts disappear when the background, due to the electron Drude response, vanishes, i.e., all electrons have relaxed from the conduction band. Figure 2.6 b) shows the temporal evolution of the IR signal over the wave number range investigated from a pump-probe delay of 100 ps to 1100 ps. Two main pump-induced absorption peaks are visible. One of these is at 1332 cm^{-1} and has been attributed to

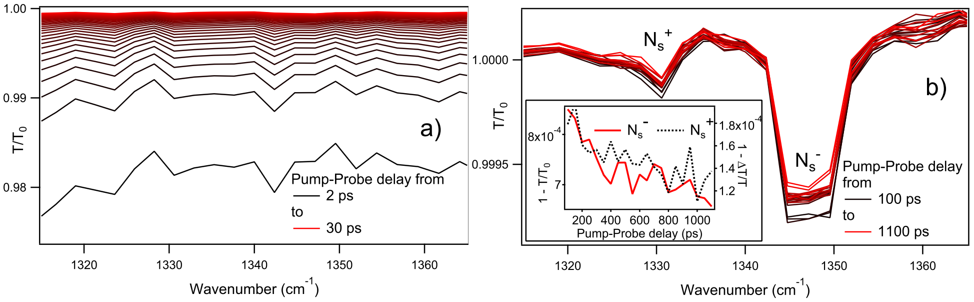

Figure 2.6: Transient IR measurements in the spectral region of the LVM of N_s: a) during electron recombination for pump-probe delays from 2 ps to 30 ps; b) after all electrons have recombined, for pump-probe delays between 100 ps and 1100 ps. The two visible peaks are assigned to the LVM of N_s^+ (left, centered at $1332\,cm^{-1}$) and N_s^- (right, centered at $1349\,cm^{-1}$). The inset shows the decay of the amplitude of both peaks in the same time frame.

the N_s^+ defect [132]. This is as expected if neutral nitrogen acts as a charge acceptor, as therefore not all photoelectrons in the conduction band would then recombine with photoionized nitrogen defects. Hence some nitrogen defects will remain positively charged. The results are therefore consistent with the assumption that a proportion of the photoelectrons have recombined with N_s^0 rather than N_s^+ defects. Looking at the figure, we also observe a second, more prominent transient IR peak at $(1349 \pm 0.5)cm^{-1}$. Our analysis suggests that this feature is the LVM of the created N_s^- states. In principle one would also anticipate to observe in Fig. 2.6 b), in addition to the LVMs from the N_s^+ and N_s^- states, a bleaching response of the N_s^0 peak because these states are now depopulated as compared to the equilibrium case. However, its absorption cross section is seven times smaller than the N_s^+ peak, and this bleaching effect is thus invisible in the experiment [132].

In order to provide theoretical support to our hypothesis that the observed transient absorption peak at $1349\ cm^{-1}$ is indeed a LVM of N_s^- , we carried out density functional calculations of the local vibrational modes of N_s in various charge states.

Some of us have previously shown that, although the positively charged substitutional nitrogen defect N_s^+ is a tetrahedral center, N_s^0 is a trigonal center with one unique N-C bond elongated by about 30% [97, 15]. The resulting shortening of the unique carbon back bonds leads to a local vibrational mode at $1344\ cm^{-1}$, which is insensitive to the nuclear mass of nitrogen in agreement with experiment [26]. However, there is a change in lattice parameter arising from the high concentrations of nitrogen in the lattice, and this has a pronounced effect on the local mode frequency [62]. Here we compare the calculated shift in the vibrational mode of N_s^- relative to that of N_s^0 by taking into account this change in lattice parameter. That is, we calculate the blueshift in the LVM resulting from negatively charging the N_s^0 defect.

In all cases, we find that there is a local mode above the one-phonon maximum, which is doubly degenerate, and therefore transforms as E in the C_{3v} point group. The calculated blueshift in frequency with change of charge state for the three cell sizes and boundary conditions are listed in Table I. For the negative charge state, the impact upon the lattice constant is greater than that for the neutral charge state so that the boundary condition has a larger impact upon the relative frequencies in the smaller unit cell than in the larger.

Although there is scatter in the relative location of the N_s^- mode to that of the neutral charge state, the average shifts for the LDA and GGA calculations are around 13 and 10 cm^{-1}, respectively. Noting that the experimental value for the local mode of N_s^0 is 1344 cm^{-1}, this places an estimate for the local mode of N_s^- around $1354-1357 cm^{-1}$, about $5-8 cm^{-1}$ larger than the experimentally determined value of 1349 cm^{-1}. It is evident, however, that these calculations qualitatively confirm the 1349 cm^{-1} resonance as being due to the N_s^- defect.

The question presents itself how, after an electron is captured by a neutral N_s^0 defect, the resulting N_s^- defect population returns to equilibrium, i.e., how N_s defects return to their neutral charge state and on what time scales this occurs. In the inset of Fig. 2.6 b), we plot the temporal evolution of the N_s^+ and N_s^- peak values, $1-T/T_0$, over the course of one nanosecond after photoexcitation. Although there is significant scatter in the data, the peak amplitudes of the two resonances are observed to decrease over this time scale. These data points were corrected for broad offsets in order to avoid the introduction of artificial trends. Spectral data points adjacent to the absorption peaks did not show a temporal decay of T/T_0 but stayed constant as expected, again confirming that the decay of the two peak decays is real. Although the poor signal-to-noise ratio of the data prevents a reliable quantitative evaluation, one can estimate a decay time by order of magnitude. Both peaks are reduced by the same amount to about three quarters of the original intensity within the measurement time. Assuming exponential decay kinetics, this corresponds to a recombination time of ~4 ns. Thus, we can assume that within ten nanoseconds, the peaks have vanished, which would correspond to an emission rate of approximately $10^8 s^{-1}$.

One conceivable mechanism for an N_s^- defect to lose its excess electron is by thermal excitation of its additional electron into the conduction band and the subsequent capture of that electron into an N_s^+ defect. The rate of this process would give an indication of the ionization energy of the N_s^- states and should increase with temperature. For that reason we performed a second set of measurements using identical parameters but with the sample at 450 K. No discernible difference was observed as compared to the room temperature case: no increase in the decay rate could be identified. However, the measured rate increase might be small and not be resolvable due to noise. In order to be distinguishable, the emission rate should at least double. This sets an upper limit for the energetic trap depth of the defect: the emission rate e_n is proportional to $e_n \sim \exp(\Delta E/k_B T)$, where ΔE is the energy gap of the defect from the conduction band, i.e., its ionization energy and k_B is the Boltzmann constant. From this it follows that the rate increase from 300 to 450 K is less than twofold when ΔE is only 50 meV or less. Thus, thermal ionization can only be responsible for charge neutralization if the N_s^- defect is shallow with a ΔE of less than 50 meV.

The existence of an acceptor level less than 50 meV from the conduction band is however at variance with earlier work [97], which suggested the N_s^- defect was responsible for the ~4.5 eV (270 nm) optical absorption band [see Fig. 2.1] commonly observed in type Ib diamond, the transition occurring from the valence band to the defect state. Given the 5.5-eV band gap, this would lead to an acceptor level around 1 eV below the conduction band. Either this assignment is wrong, and an alternative mechanism is involved in the 270-nm band, or other recombination mechanisms, e.g., Auger processes, are taking place, which lead to a temperature-independent recombination time. Concluding, with the currently available data, we cannot draw any definitive conclusion about the mechanism that compensates the excess charges.

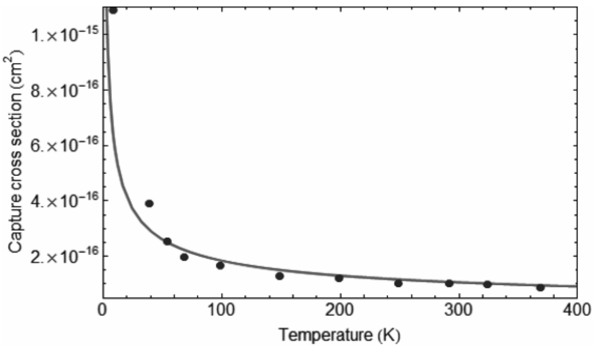

Figure 2.7: Measured temperature dependence of the capture cross section for the recombination of electrons into N_s^0 defect states (dots). The solid line represents the fit to the MPE model described in the text.

The presented data suggest that most electrons recombine with neutral N_s defects at low excitation densities. One can thus obtain a measure of the charge carrier capture cross section σ of the N_s^0 defect and its temperature dependence by relating the N_s defect concentration to the recombination time measured in the terahertz experiments:

$$\sigma = \frac{1}{N_s v \tau_r} \tag{2.2}$$

Here, N_s denotes the concentration of single substitutional nitrogen, v the thermal electron velocity (given by $v = (3k_BT/m^*)^{1/2}$) and τ_r the recombination time. The obtained capture cross sections for all three investigated samples closely resemble each other. For reasons of clarity, we only plot the capture cross sections of the 150-ppm sample, shown as dots in Fig. 2.7.

The variation of the deduced capture cross section with temperature gives an indication of the relaxation mechanism of carriers back to N_s^0 sites. Neutral single substitutional nitrogen defects are known to lie 1.7 eV below the conduction band [49]. One possibility for the electron to lose the 1.7-eV excess potential energy, while relaxing back to the defect is via the emission of photons. The observed picosecond time scale of the relaxation process however renders this picture unlikely: luminescence lifetimes in diamond are at least in the nanosecond range, and no luminescence has been reported so far in the anticipated energy range.

Another energy loss channel for the electron is via the emission of phonons. In principle, the relaxation to the N_s^0 ground state can take place in one step or sequentially through intermediate states. For instance, donor and acceptor dopants can possess a series of internal excited states, in analogy to the Bohr levels in a hydrogen atom. A charge carrier can then be captured fast into a high-lying excited state close to the band edge by the emission of phonons, followed by a slower internal relaxation cascade. However, the existence of such excited defect states requires the presence of a Coulombic field, i.e. the defect has to be charged. This is not the case here. We also rule out the influence of unintentional dopants that possess acceptor levels close to the conduction band and could act as intermediate steps in a relaxation cascade. These might exist, however their concentration would be several orders of magnitude lower than the N_s concentration and their amount thus too low to scavenge all excited electrons.

The longitudinal optical phonon energy of diamond is 165 meV [192]. A direct recombination process to the ground state would thus require the simultaneous emission of ten phonons. While this would seem to result in very low capture cross sections, it was shown by calculations in the 1970s that significant lattice distortions can facilitate the phonon emission [79, 131]. These first models were able to describe charge carrier recombination via multiphonon emission (MPE) with reasonably high capture cross sections.

In order to describe our data, we apply a simplified analytical MPE model as presented in Ref. [223]. This model essentially depends on three parameters: the Huang-Rhys factor S to describe the electron-phonon coupling strength of the transition, the energy E_{ph} of the phonon involved in the transition, and the energetic position E_T of the defect with respect to the conduction band. We set $E_T = 1.7$ eV, the ionization energy of N_s^0. It is reasonable to assume that primarily LO phonons are involved in the transition because their energy is larger than acoustical phonons and coupling to electrons more efficient. The solid line in Fig. 2.7 shows the fit that was obtained with $S = 10.1$. The Huang-Rhys factor S essentially quantifies the number of phonons emitted during the transition. Thus our obtained value makes physical sense since about ten LO phonons of 0.165-eV energy have to be emitted to cover the 1.7-eV energy difference. We note that in the model, E_{ph} is primarily determining the temperature dependence of the capture cross section. The simulations show that for large values of E_{ph}, as is the case for diamond (165 meV), σ is continuously decreasing with increasing temperature. For a phonon energy below 100meV, the model predicts that the capture cross section starts to increase above room temperature, and for values below 50 meV, it is increasing with temperature over the whole temperature range. The values of E_T and S mainly influence the magnitude of the carrier capture cross section and are to some degree interchangeable over certain intervals. Reasonable fits can thus be obtained for a number of combinations of E_T and S. The values we obtain are physically reasonable and provide a good description to the data.

Our findings are directly relevant for understanding and controlling the lifetime and mobility of free carriers in diamond. Particularly in defect-rich materials that possess rapid recombination channels like the type Ib diamonds investigated here, photocurrent techniques that rely on charge collection might not be fast enough. The ability of time-resolved terahertz spectroscopy to take conductivity "snapshots" at any point after photoexcitation permits the direct and unambiguous assessment of figures of merit such as the charge carrier lifetime and mobility in such systems. In the emerging field of spintronics, negatively charged nitrogen vacancy defects (NV^-) are a promising candidate for room-temperature spin manipulation. Their performance is currently restricted by luminescence blinking, which is likely caused by charge state conversion. The demonstrated capability of single substitutional nitrogen defects, which are always present in samples containing nitrogen-vacancy centers, to act as electron acceptor states may be important in explaining the blinking of NV^- centers, as electron capture by neighboring N_s^0 defects could possibly neutralize NV^- centers.

2.4 Conclusions

In conclusion, we have measured the picosecond dynamics of electrons excited from single substitutional nitrogen states into the conduction band in type Ib diamond using ultrafast pump-probe spectroscopy. Excitation densities were kept such that approximately only 1 out of 10^5 nitrogen defects were ionized. Using time-resolved terahertz spectroscopy, the electron mobility was deduced, and electrons were found to relax from the conduction band within tens of picoseconds. The results indicated that electrons in the conduction band scatter mainly from neutral nitrogen defects, showing mobilities that are largely independent of temperature. Furthermore, the recombination dynamics suggested that electrons predominantly relax from the conduction band into neutral nitrogen states rather than the original, ionized nitrogen defects (N_s^+). The application of a multiphonon emission model showed that this relaxation process is facilitated by the simultaneous emission of ten LO phonons. After all electrons have recombined, uncompensated N_s^+ and newly created N_s^- defects are present. The existence of the charged defects was confirmed by transient IR measurements. These measurements showed an absorption peak at 1332 cm^{-1} originating from the LVM of N_s^+ and a hitherto unknown absorption peak at 1349 cm^{-1} that is assigned to the LVM of N_s^- . The spectral position is in good agreement with density-functional calculations on the LVM of N_s^-. Our findings thus confirm that single substitutional nitrogen defects can act as electron acceptor states. The charged nitrogen defects are neutralized within approximately 10 ns. This relatively short lifetime may also explain why the negatively charged nitrogen defects have not been observed previously in steady-state optical measurements.

3

Time-resolved charge carrier diffusion in silicon nanowires

Free-standing semiconductor nanowires on bulk substrates are increasingly being explored as building blocks for novel optoelectronic devices such as tandem solar cells. Although carrier transport properties, such as mobility and trap densities, are essential for such applications, it has remained challenging to quantify these properties. Here, we report on a method that permits the direct, contact-free quantification of nanowire carrier diffusivity and trap densities in thin ($\sim$ 25 nm wide) silicon nanowires - without any additional processing steps such as transfer of wires onto a substrate. The approach relies on the very different Terahertz (THz) conductivity response of photo-injected carriers within the silicon nanowires from those in the silicon substrate. This allows quantifying both the picosecond dynamics and the efficiency of charge carrier transport from the silicon nanowires into the silicon substrate. Varying the excitation density allows for quantification of nanowire trap densities: for sufficiently low excitation fluences the diffusion process stalls because the majority of charge carriers become trapped at nanowire surface defects. Using a model that includes these effects, we determine both the diffusion constant and the nanowire trap density. The trap density is found to be orders of magnitude larger than the charge carrier density that would be generated by AM1.5 sunlight.

3.1 Introduction

Over the last years silicon nanowires have been explored extensively as components of solar cells in an effort to evaluate their potential for next generation, high efficiency and low cost photovoltaics [57]. Potential advantages of Si nanowires for solar cells include light trapping effects to increase light absorption [58, 194] and the possibility to engineer radial p-n junctions allowing to decouple the direction of light absorption from the direction of charge collection [109, 110, 220]. These advantages offered by the nanowire architecture reduce the requirements on the quality and the quantity of the Si that is needed. Another attractive aspect of the nanowire device architecture is that the underlying material properties are still those of bulk Si, with its high intrinsic conductivity. Hence many efforts are geared towards cheaper single junction c-Si solar cells based on nanowires. The properties of nanowires with respect to charge carrier transport are yet to be fully explored: their high surface/volume ratio raises for instance the influence of surface states. The potential use of these nanowires as absorber material for a solar cell depends critically on the quality of the Si nanowire interface, given the inherent extended interface region. The interface quality will determine the lifetime and mobility of minority carriers and hence the collection efficiency of photo-generated carriers. Furthermore, different ways exist of passivating surface states and quantifying remaining defect density is still challenging. One relevant question is whether all defects are electrically active? Their quantification is important because any device would rely on diffusive transport and the defect density would determine device performance.

To use Si nanowires to extend the limiting efficiency of solar cells, a tandem solar cell concept is necessary however. The ultimate goal of this is to surpass the Shockley-Queisser limit for single junction devices by absorbing the incoming light in a stack of materials with the right combination of bandgaps to reduce the thermalization losses to a minimum. In this device concept the nanowires would form the higher bandgap absorber material for the top cell, as schematically represented in 3.1.

Using the quantum size effects in Si nanowires allows one to synthesize a c-Si material with a tunable bandgap above that of bulk Si [109, 110, 220]. To get in the size regime where quantum size effects start playing a role, the diameter of the nanowires must be smaller than the exciton Bohr radius. For Si this radius is about 4.9 nm, which sets a very demanding technological target for the synthesis of nanowires to be used in this kind of device.

In working towards a proof-of-concept we have made use of DUV lithography and thermal oxidation to reach the type of low-diameter nanowires necessary for this kind of devices [128]. However, the potential use of these nanowires as absorber material for a solar cell depends critically on the quality of the interface between the

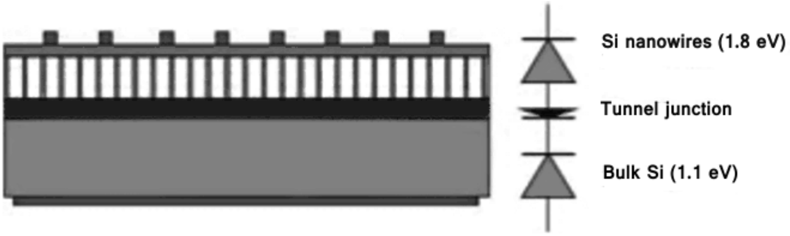

Figure 3.1: Graphical representation of an all-Si-based tandem solar cell with Si nanowires.

Si and SiO_2. Electron spin resonance (ESR) measurements have revealed the presence of a substantial inherent density of Pb_0 ($Si_3 \equiv Si\cdot$) defects (dangling bonds) at the nanowire Si/SiO_2 interfaces, most likely due to faceting and enhanced interface strain from the oxidation [95]. To quantify the effect of these inherent defects on the lifetime and mobility of charge carriers generated in the nanowires, we employ time-resolved terahertz spectroscopy to probe the behavior of photo-generated carriers on picosecond timescales.

Exciting the nanowires at oblique incidence of 45° using a femtosecond laser pulse with photon energies of 4.6 eV we generate charge carriers across the direct bandgap. The short absorption lengths at this wavelength allow for predominant excitation of the NWs, with only a small fraction of the excitation light reaching the substrate where it generates additional charge carriers. The photoexcited charge density gradient between nanowires and substrate drives diffusion of carriers from the nanowires into the substrate. As shown below, the charge carrier conductivity in the bulk substrate is many times larger than that in the wires. Thus, the time-dependent conductivity, measured on picosecond timescales using Terahertz (THz) probe pulses, allows us to follow the transport of photoexcited carriers from the wires to the bulk phase. More importantly, the number of carriers reaching the bulk phase allows us to quantify the losses associated with this transport as a result of carrier trapping at the surface of the nanowires. We model this process using a simple simulation of charge diffusion and trapping, which considers the initial photoexcited charge density gradient, transport from the wire to the bulk substrate and carrier trapping into nanowire surface defects. The data in conjunction with the model provides the carrier diffusion coefficient and the density of NW traps. Surprisingly, the latter was found to be around two orders of magnitude lower than the surface defect density as measured by ESR, depending only slightly on the type of oxide layer on the nanowire surface. Nanowires that had been exposed to nitrogen gas during annealing in order to remove surface hydrogen bonds displayed trap densities of $4.5 * 10^9 cm^{-2}$. Nanowires that had been exposed to forming gas instead of nitrogen during annealing, showed reduced trap densities of $2 * 10^9 cm^{-2}$.

3.2 Methods

Several methods exist to fabricate Si nanowires. We employ a combination of deep UV lithography and dry etching. The target dimension after dry etching is set around 40 nm and further size reduction is achieved by thermal oxidation. The material used is (100)-oriented 1-10 Ωcm p-type Cz Si wafers of 300 mm diameter. No intentional doping is introduced before dry etching. First the patterning stack is deposited on the wafer. The pillars are defined by double-patterning a mask consisting of 45 nm lines with a 90 nm pitch by deep UV lithography. The mask is rotated ~ 91° between the two exposures in order to obtain a staggered array of dots in the resist. Subsequent dry etching with different etch chemistries is performed to transfer the pattern through each of the layers of the patterning stack. The final Si etch is performed with a mixture of SF_6, CH_2F_2 and N_2/He. After the Si etch a dry in-situ strip is performed to remove residual hard mask.

Since quantum confinement for Si does not occur at the diameters obtained after dry etching, the size of the nanowires is further reduced by thermal oxidation. The Si NW core diameter is further reduced by rapid thermal oxidation at 1150 °C for 60 s in an O_2/N_2 ambient in two steps. After a first oxidation, the oxide is removed in a dry NF_3/NH_3 based chemical etch. The second oxidation step is a repetition of the first. The final size of the diameter of the nanowires can be tuned by a combination of dry etching and thermal oxidation. The nanowires used in this study had a tapered profile of 500 nm high, 36 nm diameter at the bottom and 12 nm diameter at the top (see Figure 3.2). For the SEM imaging the thermal oxide was removed by vapor HF to be able to measure the size of the c-Si cores.

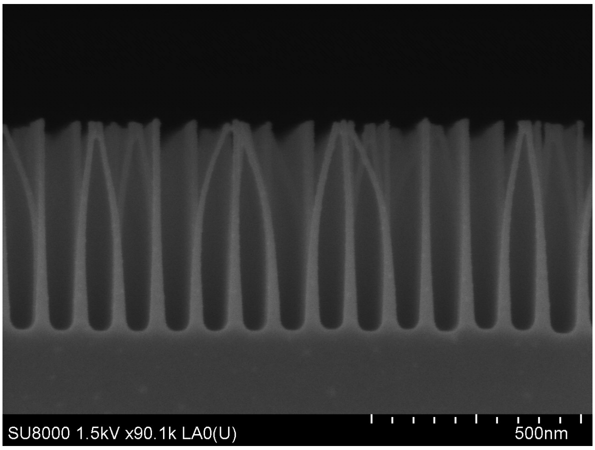

Figure 3.2: Scanning electron microscope image of the nanowires after thermal oxidation. The thermal oxide was removed by vapor HF for this SEM image but not for the terahertz spectroscopy.

The nanowires become very flexible once < 20 nm, especially when they are hit by the electron beam and charging occurs as in the image. To keep the NWs aligned and prevent bending and breaking the thermal oxide is left on the nanowires for the terahertz measurements. Additionally the inter-wire space was filled with a-SiO_2 using a cycled plasma enhanced chemical vapor deposition at 200 °C.

After the oxidation an experimental split was created by an additional passivation or de-passivation step. On the first sample (Sample 1), depassivation of dangling bonds was obtained by annealing in nitrogen at 700 °C for 30 minutes. On the second sample (Sample 2) dangling bond passivation was performed by applying a forming gas anneal (95% N_2, 5% H_2 gas) at 400 °C for 30 minutes.

The time-resolved THz setup is pumped by an amplified Ti:Sapphire laser system that delivers 800nm (1.55 eV), 100fs pulses at 3W of output power and a repetition rate of 1 kHz. Light pulses at 266nm (4.6 eV), generated by frequency-tripling the fundamental (1.55 eV) using two 1mm thick BBO crystals, is used to photo-inject carriers into the silicon nanowires. The polarization of the 266 nm beam could be rotated using a half-wave plate. Single-cycle THz pulses are subsequently used to measure the frequency-dependent conductivity with sub-picosecond time resolution. The generation and detection of the THz probe is accomplished by nonlinear optical rectification and electro-optic detection, respectively, using the 800 nm pulses in two 1mm thick ZnTe crystals [205]. The charge density dynamics were measured by probing the excitation-modulated differential signal at the peak of the THz field. In this way, only the real part of the photoconductivity, i.e. the photoinduced change in absorption, which is proportional to the charge density, is measured at a frequency of approximately 0.6 THz. The complex THz photoconductivity spectra were measured by recording the transmitted THz electric field $E(t)$ through the unexcited sample and the photomodulated differential THz field $\Delta E(t)$ and subsequently using a thin-film approximation in the frequency domain with the respective Fourier-transforms of the time-domain electric fields [205].

3.3 Results and discussion

Figure 3.3 shows the time evolution of the real part of the photoconductivity at 0.6 THz after exciting Sample 1 with photon energies of 4.6 eV (266 nm) and fluences of $9.5 * 10^{11} cm^{-2}$ at an angle of 45° in p-polarization (excitation E-field parallel to wires) and s-polarization (field perpendicular to wires). The sample consisted of NWs with an average diameter of 25 nm. The black graph shows the measured photoconductivity when exciting the sample on the backside also at 45° incidence, i.e. directly injecting carriers into the silicon substrate. As expected for an indirect semiconductor, for which recombination is slow, the conductivity increases quasi-instantaneously at pump-probe delay $\tau_p = 0$, to remain constant within the 400 ps time window. The signal is larger for p-polarized light since the reflection is smaller and thus more light is absorbed in the substrate. When the NW layer is excited, the initial signals are smaller due to the much reduced THz conductivity of carriers in the NWs (see model below). For NW excitation, the conductivity shows an instantaneous component, attributed to light directly reaching the substrate, and a slow rise of the photoconductivity, attributed to carriers reaching the bulk phase from the NWs. Interestingly, s-polarized light generates a larger initial response than p-polarized light, conversely to the substrate excitation, while the degree of increase is more pronounced for p-polarized light. The final photoconductivity after 400 ps is larger for both pump polarizations as compared to the substrate excitation. The

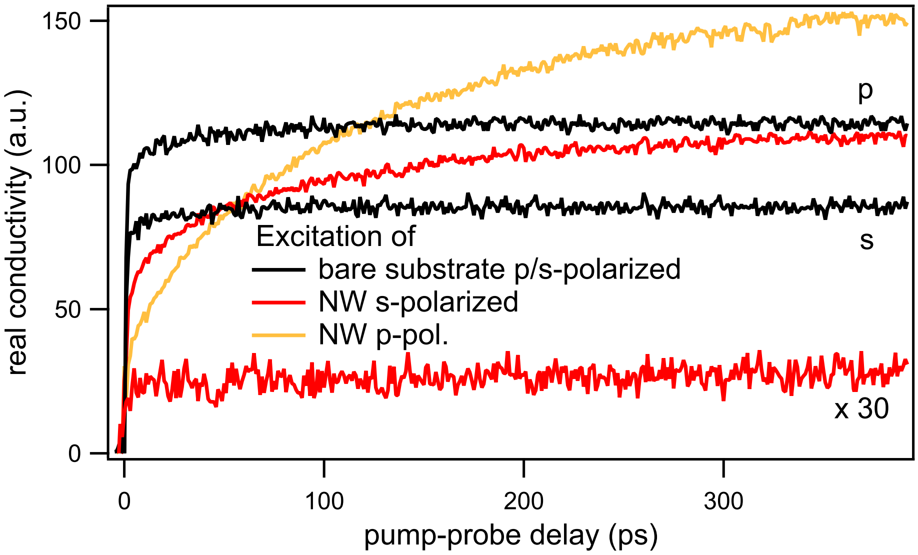

Figure 3.3: Dynamics of the THz real conductivity of silicon nanowires on bulk silicon after excitation with 266nm light at an angle of 45ř and a photon flux of $9.5 * 10^{11}\mathrm{cm}^{-2}$. Black graphs show excitation of the bare substrate for p and s polarization, whereas red and yellow graphs show nanowire excitation for s and p polarization, respectively. The lower red graph is rescaled by factor 30.

lower red graph shows the rescaled real conductivity for a fluence of $2.9 * 10^{10}\mathrm{cm}^{-2}$, where no increase is present, pointing to only direct bulk excitation. This change in the dynamics can be understood by noting that trapping of charge carriers occurs in the NWs, which, in particular at low excitation densities, prevents carriers generated in the wires to reach the bulk. At higher excitation densities the traps get saturated, and carriers can reach the bulk phase on ~100 ps timescales.

In order to gain more insight into these intricate dynamics through assessing the NW and substrate contribution to the measured signal, it is useful to look at the frequency-resolved complex photoconductivities provided by the broad THz probe spectrum. The frequency dependence of the conductivity for charge carriers in bulk and nanowires is expected to be different and the discrimination of both thus possible [205].

The bulk penetration depth for 266nm light is around 5 nm and the length of the NW layer along the optical pathway is 700 nm for 45° excitation. Hence, since the excitation layer is smaller than $1\mu\mathrm{m}$, i.e. many orders of magnitude smaller than the THz wavelength, we can use the thin-film approximation to extract the complex conductivity $\hat{\sigma}_{tot}(\omega)$ at various pump-probe delays τ_p :

$$\hat{\sigma}_{tot}(\omega,\tau_p) = -\frac{2c\epsilon_0 n}{l}\frac{\Delta E(\omega,\tau_p)}{E(\omega)} \tag{3.1}$$

Here, c is the speed of light, l the length of the excitation layer, ϵ_0 the free space permittivity and n the refractive index of silicon at THz frequencies (=3.4).

The overall conductivity $\hat{\sigma}_{tot}$ will be composed of contributions from charge carriers in the nanowires $\hat{\sigma}_{nw}(\omega)$ and those in the underlying bulk substrate $\hat{\sigma}_{bulk}(\omega)$:

$$\hat{\sigma}_{tot}(\omega) = \hat{\sigma}_{bulk}(\omega) + \hat{\sigma}_{nw}(\omega) \tag{3.2}$$

For charge carriers in the bare substrate the conductivity $\hat{\sigma}_{bulk}(\omega)$ can be described well using the Drude model [39]:

$$\hat{\sigma}_{bulk}(\omega) = \frac{N_s e^2/\epsilon_0 m^*}{1 - i\omega\tau_s} \tag{3.3}$$

Here, N_s is the charge carrier density, e the electric charge, m* the carrier effective mass (=0.27m$_0$ for the electron) and τ_s the carrier scattering time. The extracted scattering time is somewhat reduced for higher charge densities due to increased likelihood of electron-hole scattering events [74]. From experiments where the substrate is directly excited, we find values between 150 fs for the highest excitation densities and 210 fs for the lowest ones used in the experiments.

Charge carriers in nanowires respond differently to the THz probe than in bulk. In such a confined geometry carriers experience a restoring force which results in a shift of the conductivity response (centered at zero for the Drude response) to higher frequencies. Depending on the exact conditions and the consequential physical origin of this restoring force, one can describe this situation by either plasmon resonances [160, 166, 195], embedding the Drude model in an effective medium [77], applying a generalized version such as the Drude-Smith model [189], or even use Monte-Carlo simulations [157]. For all these models a Lorentzian oscillator provides a good approximation of the NW charge response in the THz probe window:

$$\hat{\sigma}_{nw}(\omega) = \frac{a}{1 - i\tau_{nw}\omega(1 - \omega_r^2/\omega^2)} \tag{3.4}$$

Here, a denotes the magnitude of the NW contribution, τ_{nw} the carrier scattering time in the nanowires and ω_r the resonance frequency.

In our description of $\hat{\sigma}_{tot}(\omega)$, we obtain the initial substrate charge density N_s from the magnitude of the instantaneous (near 0 ps) conductivity. The bulk scattering time τ_s corresponding to the inferred value of N_s is determined independently from calibration measurements exciting the substrate at varying charge densities. In this manner the contribution of $\hat{\sigma}_{bulk}(\omega)$ can be determined independently, and the parameters determining $\hat{\sigma}_{nw}(\omega)$ can be readily determined from the data.

Figure 3.4 a) shows an exemplary fit to data obtained exciting the nanowires using s-polarized light, for a pump-probe delay time of 10 ps, for which $\tau_s = 170\text{fs}$. The Drude contribution is clearly dominating the signal, with only the low-frequency tail of the NW contribution appearing in the THz probe window. Figure 3.4 b)

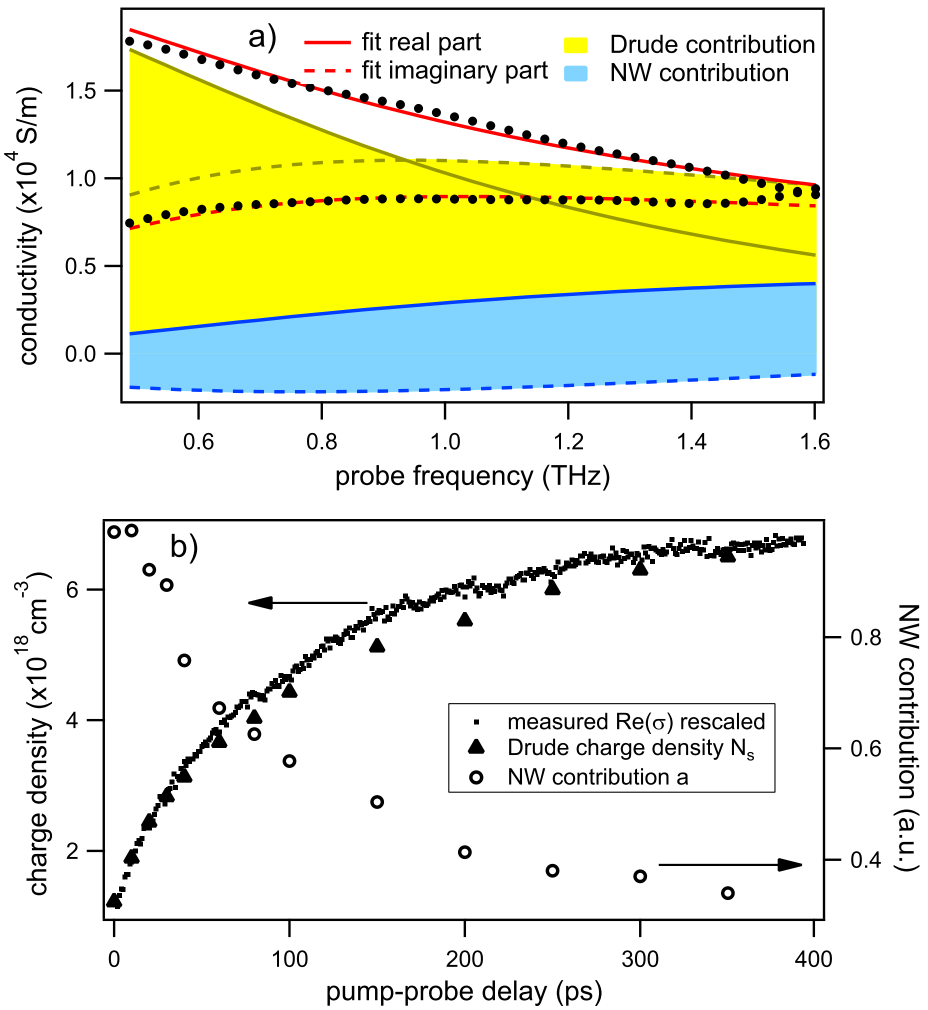

Figure 3.4: a) Complex THz photoconductivity for nanowire excitation at a pump-probe delay of 10 ps (black dots). Red lines show the fit to the two-component model and the yellow and blue shaded areas the Drude and NW contribution, respectively; b) shows the corresponding real-conductivity dynamics (black dots) and the extracted model parameters: filled triangle=substrate charge density N_s; open circles NW contribution α.

shows the extracted Drude charge densities N_s and NW magnitude α at various pump-probe delays for the THz dynamics depicted by the black dots, which were rescaled to match N_s for clarity. As can be seen, the increase in the real conductivity originates from an increase in the charge density in the substrate. At the same time, α is decreasing, indicating depletion of carriers in the nanowires. It is apparent that the observed THz conductivity increase observed in Figure 3.3 when exciting the NWs are due to diffusion of charge carriers from the nanowires into the bulk, where the carriers exhibit a larger response in our frequency window. Figure 3.4 further

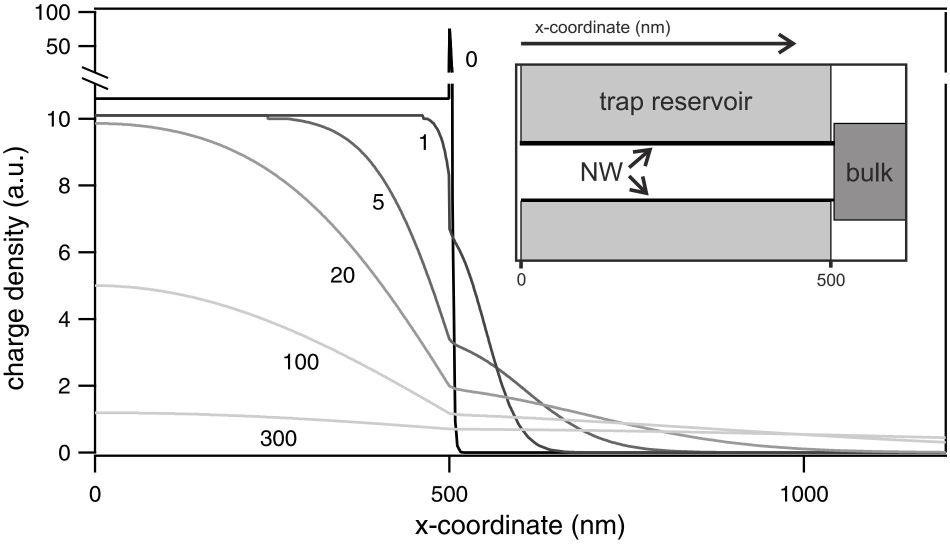

Figure 3.5: Simulated time evolution of the charge density for various pump-probe delays in picoseconds, indicated by the numbers next to the graphs. Nanowires are located in the range $0 < x < 500nm$ and bulk Si for $x > 500nm$. The inset sketches the geometry used for the simulations. Two nanowires are attached to the substrate and one trap reservoir to each nanowire in which charge carriers are trapped.

suggests that the signal in the dynamics as measured in Figure 3.3, which is the real conductivity at 0.6 THz, is dominated by the Drude response of the substrate carriers. Hence, we can thus use this type of measurement as a means to infer the time-dependent charge density in the substrate, a quantity which is governed by diffusion and trapping.

The difference in response observed between s- and p- polarized excitation of the nanowires (Figure 3.3) shows that the optical extinction coefficient of the Si NW layer is anisotropic with respect to the polarization of the excitation light. In particular, more light reaches the substrate when the excitation pulse is s-polarized than for p-polarized light, resulting in a larger initial bulk charge density. At the same time, more carriers are injected into the substrate for p-polarized light, indicating that more excitation light was absorbed in the nanowires. Quantifying this behavior provides a good starting point to extract the optical extinction coefficient of the NW layer as a function of several parameters. As we will show in a following publication based on more extensive THz measurements, the extinction coefficient not only depends on the polarization, but also on the excitation angle, the NW diameter (i.e. filling fraction) and the sample orientation. Using extinction coefficients of single silicon nanowires obtained from Mie-scattering calculations, which are embedded in an effective-medium model, we are able to explain this behavior quantitatively.

In order to quantify the diffusion and trapping dynamics we constructed a time-dependent diffusion model in COMSOL which considers the sample geometry and the charge density profile that is generated by the excitation beam as the starting condition. In the model, the excitation photon flux Φ_0 can be adjusted and the relative amount of excitation light that is absorbed in the NWs r_{nw}. For $r_{nw} = 1$ all light is absorbed in the NW layer; for $r_{nw} = 0$ the absorption is limited to the bulk substrate. In the experiments this parameter can be modified by exciting the front or back of the sample, and, for front excitation, by rotating the pump polarization. The initial density of photoexcited carriers in the NWs (N_{nw}) and the substrate (N_{sub}) are derived from Φ_0 and r_{nw}. The reflection of the pump beam at the NW-substrate interface is also taken into account. The refractive index of bulk silicon at 266nm is 2.45 and effective-medium calculations show that, due to the SiO_2 filling between the wires, the refractive index of the NW layer is 1.53 for p-polarization and 1.71 for s-polarization. Hence, we use 1% reflection for p-polarized light and 8% for s-polarized light. The small reflective losses explain the large long-time signal in Fig. 3.3. The NW trap density N_t and the diffusion constant D enter as simulation parameters. The inclusion of N_t is necessary given the observation that for low N_{nw} less carriers are injected from the NWs into the substrate, until below a certain density no more injection occurs (Fig. 3.3). Trapping centers are identified as midgap states at the NW surface.

The inset of Figure 3.5 shows the geometry used for the simulation. Two nanowires with the appropriate dimensions are attached to the bulk substrate. Both nanowires have a trap reservoir attached to them in which a controlled amount of carriers can diffuse into, thereby getting trapped. At $\tau_p = 0$ the initial charge density profile is created, as shown in the main window of Figure 3.5. It shows the charge density distribution along the x-axis in nanowires and bulk (interface at $x = 500\text{nm}$) for a number of pump-probe delays. The numbers next to the graphs indicate the pump-probe delay in picoseconds. The total charge density is split and assigned to the nanowires and the substrate by considering the reflection at the NW-substrate interface and r_{nw}. We assume that trapping occurs quickly on the timescale of diffusion into the bulk, and allow a charge density corresponding to N_t to be withdrawn from the nanowires into the trap reservoir within the first picosecond. This results in a homogeneous reduction of N_{nw} along the nanowire. In the depicted case, 3.8% of N_{nw} was subtracted. We note that recent ultrafast transient absorption measurements on silicon nanowires have shown that trapping occurs within about 10 ps [104]. The inclusion of a longer trapping time in our model merely leads to a slight speedup of the diffusion process on the timescale of the trapping process but does not affect the value of N_t. As time progresses, charges diffuse into the substrate until an equilibrium between the two material components is reached. For every calculated time step the charge density in the bulk is spatially integrated, which serves as the analogue to the measured THz signal.

In order to quantify the magnitude of charge carrier transfer from the nanowires into the bulk, we define the quantity A as $A = 1 - \mathrm{Re}[\hat{\sigma}(\tau_p = 0\text{ps})]/\mathrm{Re}[\hat{\sigma}(\tau_p = 400\text{ps})]$. It quantifies the fraction of charge carriers in the bulk at late pump-probe delays that originate from the nanowires. For initial nanowire carrier densities N_{nw} much larger than the trap density N_t, the diffusion dynamics are unaffected by the trapping process and A only depends on r_{nw}, which provides a way to estimate the latter parameter. Values of r_{nw} close to one, which emerge for p-polarized excitation, result in values for A approaching one. S-polarized excitation gives A around 0.55 and $r_{nw} \approx 0.6$; for p-polarized excitation $A \approx 0.8$ and $r_{nw} \approx 0.87$. When N_{nw} is lowered by decreasing Φ_0 and becomes comparable to N_t, A decreases and eventually reaches values of zero when most carriers in the wires have been trapped and hence no injection from the wires into the bulk occurs. Sweeping Φ_0 through this regime in the experiment thus provides a means to estimate N_t.

Figure 3.6 shows data and the matching simulations for exactly this procedure. Φ_0 was changed by a factor of about 30 from the lowest to the highest THz trace. The upper panel is s-polarized excitation where $r_{nw} = 0.6$ and the lower panel p-polarized excitation for which $r_{nw} = 0.87$. Note that no adjustments were made for Φ_0 in the simulations with respect to the experimental pump fluence. The deviations for some traces concerning the magnitude of the real conductivity are therefore due to experimental uncertainties in the determined fluence.

For the highest excitation density, $N_{nw} >> N_t$, trapping is negligible. For the s-polarized excitation case only 3.8% of the generated carriers in the NW are trapped. The injection time is to a first approximation constant and depends in the model only on the diffusion constant which was found to be $(12 \pm 2)\mathrm{cm}^2/\mathrm{s}$. This is about a factor three lower than the bulk diffusion constant, which we calculate to be around 30 cm^2/s for electrons by taking the measured bulk Drude scattering time of 170 fs and using the Einstein diffusion relation $D = kT\tau_s/m^*$, where k is the Boltzmann constant and T room temperature. The reduction of diffusivity is expected when going from bulk to an essentially one-dimensional diffusion mechanism where carrier scattering with the NW boundary becomes more dominant. The inset of Figure 3.6 a) shows a magnified view of the three lowest photon fluxes. One can see that A is decreasing for decreasing Φ_0, reaching zero for $2.9 * 10^{10}\mathrm{cm}^{-2}$ and s-polarized excitation, corresponding to 100% trapped carriers in the simulation. We note that for this lowest photon flux on average only one to two carriers are excited per nanowire. We obtain a trap density of $N_t = (4.5 \pm 1.5) * 10^9\mathrm{cm}^{-2}$, which in turn indeed corresponds to the presence of only one to two active traps per NW on average.

We also measured a sample (Sample 2) with the same NW diameters, however treated with a forming-gas anneal step, which is supposed to improve the surface passivation. For the lowest photon flux of $2.9 * 10^{10}\mathrm{cm}^{-2}$ at s-polarized excitation we observed a decrease in A but it did not reach zero like in the previous sample. We estimate a trap density of $N_t = (2.0 \pm 1.0) * 10^9\mathrm{cm}^{-2}$, thus about a two-fold decrease in N_t as compared to the other sample. It is worth mentioning that we neglect the influence of excitation light scattering. The length of the nanowires is on the order of the excitation wavelength, and nonresonant scattering is therefore likely to occur. Part of the scattered light can be "lost", i.e. neither absorbed in the nanowires nor in the substrate. In that case we would overestimate N_{nw} and in turn underestimate

N_t. We estimate that less than 20% of the excitation light is lost in that way, which places the resulting variance within the error of our values.

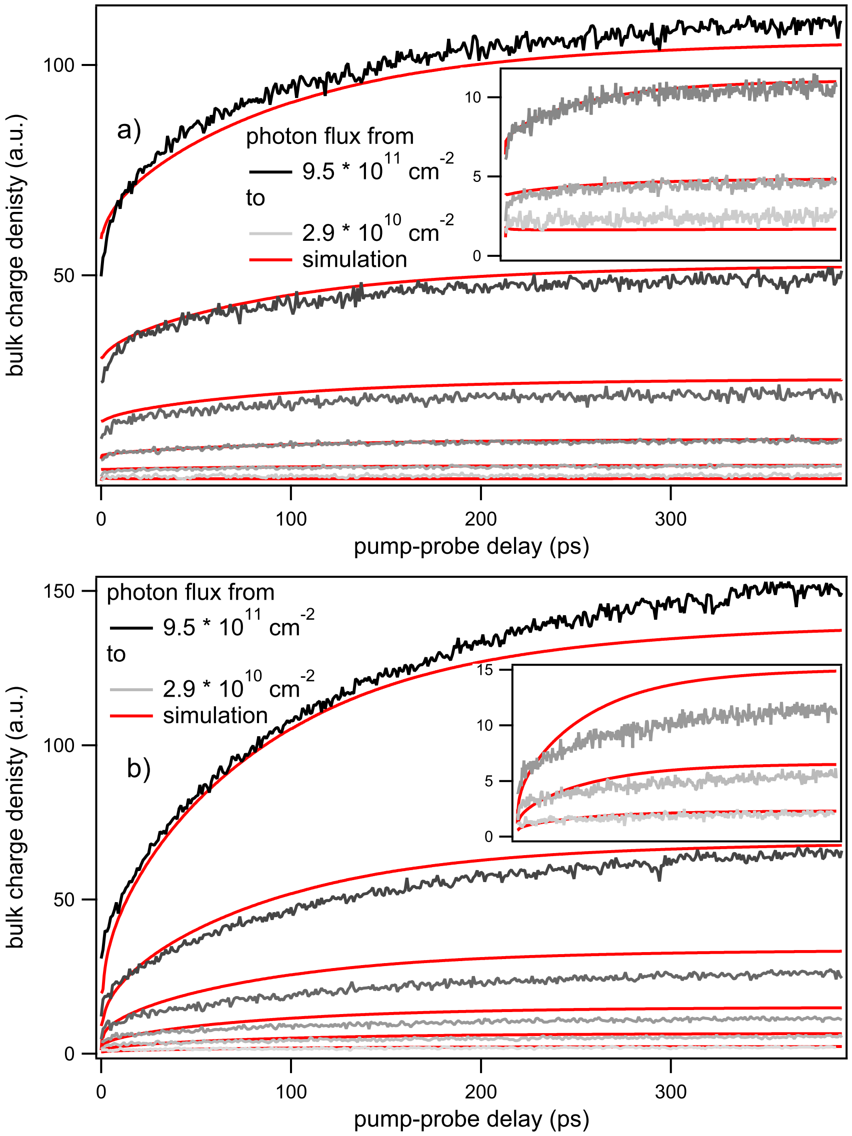

Figure 3.6: Time-resolved substrate charge density for various photon fluxes Φ_0; a) s-polarized excitation and b) p-polarized excitation. Red lines depict the results of the diffusion model. The inset shows a magnified view of the three lowest Φ_0.

The values of our trap densities are comparable to previously published results on similarly passivated silicon NWs [33], which might however be coincidental. The authors inferred the trap density from measurements of the photoluminescence decay rate of photoexcited electron-hole liquid (EHL) droplets, which was on the order of 100ns, as a function of NW diameter, and used literature room-temperature capture cross sections (CCS) to eventually obtain the trap density. The experimental conditions the authors used were however different to ours: firstly, the sample was held at a temperature of 10K, which can already alter the CCS and thus the inferred trap density. Also, even though no exact statements were given on the pump fluence and on the photogenerated charge density, they were presumably orders of magnitude larger than our values, for such magnitudes are required in order to reach the EHL phase [198]. Furthermore, a pulsed laser with nanosecond pulse duration was used. Given previously reported trapping times of around 10 ps [104], these excitation conditions, i.e. high pump fluences over nanosecond timescales, will give rise to trap filling already during the excitation process. That would mean that the measured recombination dynamics will be convoluted with the timescale of the occupied traps returning to their equilibrium state, thus increasing the EHL recombination time. We would like to stress that our measurements probe the trapping process in a more direct fashion. The femtosecond excitation process is quasi-instantaneous with respect to trap-filling times and non-trapped carriers are directly "counted" through their THz photoconductivity after injection into the bulk.

Interestingly, the inferred trap density is much lower than the density of midgap states, which originate from unpassivated silicon dangling bonds, and which are the most probable source for trapping. Some of us have previously performed ESR measurements on similarly passivated NWs with a mean diameter of 10nm [95], which yielded a defect density of about $1 * 10^{12}\mathrm{cm}^{-2}$, i.e. about two orders of magnitude larger than the trap density inferred here. The defect density of the 25 nm NWs investigated here is presumably lower but likely to be on the same order of magnitude: smaller diameter NWs possess a higher curvature and thus more strained Si-O bonds, leading possibly to more dangling bonds. The large discrepancy between trap density and surface defect density indicates that not all midgap states act as carrier traps. Indeed, a previous study using pulsed photoluminescence has already shown that silicon dangling bonds of unstrained reconstructed bulk silicon surfaces are not recombination-active [36]. A similar situation might occur here for some defects, although the large strain in the nanowires presumably creates unsaturated silicon bonds beneath the surface whose dangling bonds in turn form active recombination centers [36].

On the other hand, our measurements are only sensitive to trapping occurring on picosecond timescales, which is a reasonable timeframe with respect to commonly accepted defect CCSs and recent ultrafast measurements on carrier-defect recombination in bulk and nanostructured semiconductors [183, 204, 91]. It is however conceivable that the apparent low trap density originates from a dramatic decrease in the CCS. Interface effects such as the Coulomb blockade screening mechanism, which is known to occur at the Si-SiO$_2$ interface and which has been well-studied in short-channel bulk silicon [147] and silicon NW field-effect transistors [225], can lead to a dramatic reduction of the CCS, particularly at the extremely low charge densities present here [148]. On that account, the specification of a trap density is somewhat meaningless without knowledge of the CCS and vice versa. We thus cannot fully conclude on whether all midgap states are electrically active, albeit with a reduced CCS, or whether only some of them are active possessing large CCSs.

Irrespective of the actual trapping mechanism, the possible existence of traps that are not accessible with our measurement approach or other effects that could inhibit diffusion, the minimum charge density as measured here from which diffusion occurs constitutes a key figure of merit since it will determine the potential of using the NWs as active material in devices (e.g. solar cells) that rely on diffusion. In order to extract a photocurrent from the NWs, it must be possible to collect the majority of generated carriers. Our measurements however suggest that when the fluence is reduced, all carriers generated in the NWs are trapped within the first few picoseconds. For the lowest pump fluence in our measurements (30 nJ/cm^2) all carriers that were generated in the wires, which is on average only one to two carriers per NW, are trapped and no significant amount of carriers is injected into the bulk. It is therefore evident that many carriers need to be present in a single NW simultaneously for traps to be passivated; otherwise no photocurrent will be collected from a solar cell with thin silicon NWs as the active material. If one assumes a trapping time of 10 ps, the fluence of 30 nJ/cm^2 translates to a minimum power density of 3 kW/cm^2 that is required to fill traps in order to inject the remaining carriers into the bulk. This is orders of magnitude larger than the 100 mW/cm^2 power from the AM1.5 spectrum.

This conclusion might seem in variance with recently published results on silicon NW solar cells for which good efficiencies were demonstrated [110, 200]. These devices however relied on appreciably thicker NWs with diameters of about $1\,\mu\mathrm{m}$, where the influence of surface defects is greatly reduced [200], or NWs of about 200 nm diameter with a coaxial p-i-n structure which reduces the diffusion length of minority carriers and screens them from surface defects [200]. Devices that would rely on much thinner silicon NWs such as the ones investigated here, for instance in order to exploit quantum confinement effects, will require greatly reducing the impact of trapping. It is likely that NWs made of different semiconductors but comparable diameters will face similar challenges.

3.4 Conclusion

We have measured the diffusion dynamics of photogenerated charge carriers in an ordered silicon NW array on bulk silicon. We observe that charge carriers, which are excited in the NWs by a femtosecond UV pulse, diffuse into the bulk on 10's to 100's picosecond timescales. For sufficiently low excitation fluences this diffusion process stalls because the majority of charge carriers become trapped at NW surface defects. Using a model that simulates the diffusion process we extracted parameters such as the diffusion constant and the NW trap density. The trap density was found to be two orders of magnitude smaller than the density of surface defects that are commonly identified as carrier traps. This suggests that either only a small part of surface defects can actually scavenge charge carriers or that screening mechanisms reduce the capture cross section. Irrespective of the mechanism, the charge density at which diffusion stalls is orders of magnitude larger than what would be generated by sunlight. Hence, in order to collect photoexcited charge carriers using these thin silicon NWs as active material in a solar cell, surface defect passivation must be dramatically improved.

4

Loosening electronic quantum confinement in colloidal nanoparticles

We report on the gradual evolution of the conductivity of spherical CdTe nanocrystals of increasing size from the regime of strong quantum confinement, with truly discrete energy levels, to the regime of intermediate confinement with closely-spaced hole states. We use the high-frequency (terahertz) conductivities of optically injected carriers in the nanocrystals to report on the degree of quantum confinement. For the smaller CdTe nanocrystals (3 nm < radius < 5 nm), the complex THz conductivity is purely imaginary. For nanocrystals with radii larger than 5 nm we observe the onset of real conductivity, which is attributed to the increasingly smaller separation between the valence hole states. Remarkably, this onset occurs for a nanocrystal radius significantly smaller than the bulk exciton Bohr radius $a_B \sim 7nm$, and cannot be explained by purely electronic transitions between hole states, as they are computed by tight-binding calculations. The real conductivity observed in the larger nanocrystals can be qualitatively explained by the emergence of polaron states due to the resonant coupling between hole transitions and optical phonon modes. These polaron states possess larger oscillator strengths and broader absorption, and thereby give rise to enhanced real conductivity within the nanocrystals.

4.1 Introduction

Downsizing semiconductor structures into the nanometer regime is an important trend in electronic research and manufacturing, not only for the resulting increase in performance and compactness of electronic devices. Electronic quantum confinement occurring in materials possessing dimensions smaller than the charge carrier wavefunction provides a unique means for tailoring electronic properties. Among zero-dimensional nanostructures, i.e. quantum dots, colloidal nanocrystals have proven to be particularly useful in optoelectronic devices such as displays and solar cells, largely due to the tunability of the bandgap by size [191] in conjunction with simple solution processing and ready control over surface functionality.

The degree of electronic confinement is commonly determined by the ratio between crystal radius R and bulk exciton Bohr radius a_B, and materials are classified accordingly into the strong ($R/a_B < 1$), intermediate ($R/a_B \sim 1$) or weak ($R/a_B \gg 1$) confinement regime [43]. Colloidal nanocrystals are typically manufactured to be in the strong confinement regime. Such nanocrystals are characterized by the occurrence of discrete, "atom-like" electronic states as a result of the spatial quantum confinement of electron and hole wavefunctions. The electronic properties are fundamentally different from their larger-sized (or bulk) counterparts where electronic states form continuous bands. Electronic conduction in the classical sense is absent in these nanocrystals due to the lack of closely spaced electronic levels into which carriers can scatter and consequently gain a directional net momentum when an electric field is applied. Indeed, the complex conductivity of charge carriers in quantum dots has been shown to have a finite imaginary, but zero real, component, since no current can flow [208]. The imaginary conductivity arises from the polarizability of electrons and holes within the nanocrystals: the extended wavefunctions are highly polarizable under the influence of external electric fields [45].

A relevant and fundamental question arises in the transition region, where the crystal size starts to exceed the exciton Bohr radius, i.e. in the intermediate regime between the limits of weak and strong confinement. Various theoretical and experimental efforts have shown that the electronic structure remains significantly altered, even for material sizes several times the exciton Bohr radius [42]. The question that arises is how and when conductivity emerges upon loosening of the quantum confinement in quantum dots.

Here, we report on the onset of real conductivity upon loosening the electronic quantum confinement in colloidal CdTe nanocrystals through increasing their size. The conductivity transition is probed by measuring the terahertz response of excitons that are optically excited in the quantum dots. The THz probe spectrum is broad and on the low-energy side, ranging from ~ 1 meV (~ 300GHz) to a few meV. THz spectroscopy allows for contact-free conductivity measurements with very high (subpicosecond) time resolution [205]. We find evidence for the appearance of real conductivity already for radii exceeding 5.3 nm. This is significantly smaller than the bulk exciton Bohr radius a_B of around 7 nm, which is defined through $a_B = \epsilon_{np}\hbar^2/\mu e^2$, where ϵ_{np} is the dielectric constant ($\epsilon_{np} = 10.6$), $\hbar$ the reduced Planck's constant, μ the reduced exciton mass and e the electric charge.

4.2 Methods

4.2.1 Synthesis and characterization of the nanocrystals

Colloidal CdTe nanocrystals with radii ranging from 3 to 8 nm were prepared by a modified SILAR procedure using smaller CdTe nanocrystals (3.5 - 5 nm diameter) as seeds [37]. The nanocrystal samples were characterized by optical spectroscopy (absorption and photoluminescence) and transmission electron microscopy (TEM). To remove excess surfactants and unreacted precursors the samples for THz spectroscopy were purified by dissolving the crude reaction mixture in toluene and subsequently precipitating the nanocrystals by methanol addition. The details:

CdTe nanocrystal seeds with 3.5 nm diameter

Chemicals: Dimethylcadmium (99.9%) was purchased from ARC Technologies. Tellurium (99.999%, < 250 μm) was purchased from Heraeus. Dodecylamine (DDA, 98%), Tri-octylphosphine (TOP, 90%), methanol and chloroform were purchased from Aldrich. Before use, DDA was degassed and dried under vacuum at 100°C for several hours.

Synthesis of DDA capped CdTe QDs [216]: In a three necked flask 10 g of dry DDA and 7 mL of TOP were heated to 50°C. To this solution 0.22 g (1.54 mmol) Cd(Me)2 in 7 mL of TOP and 0.16 g (1.25 mmol) Te powder were added. The reaction mixture was heated to 200°C under vigorous stirring and kept at this temperature for 4 h.

CdTe nanocrystal seeds with 10 nm diameter

Chemicals: Octadecylamine (ODA, >90%) was purchased from Fluka. Tributylphosphine (TBP, 99%) and Tetradecylphosphonic acid (TDPA, min 97%) were purchased from Bunschwig and STREM Chemicals, respectively. 1-Octadecene (ODE, tech. grade, 90%) and trioctylphosphine (TOP, tech. grade > 90%) were purchased from Aldrich. Cadmium acetate dihydrate ($Cd(Ac)_2 2H_2O$, 99.99+%) and tellurium powder (99.999%, ≤250 micron) were purchased from Chempur. Anhydrous toluene, anhydrous hexane, anhydrous methanol, and anhydrous acetone were purchased from Sigma-Aldrich. All reagents were used as purchased with the exception of ODE and ODA. Before use, ODE and ODA were dried and degassed under vacuum (3 h at 120°C).

Stock solutions: A stock solution of Cd-TDPA precursor was made by heating a mixture containing 1.76 g (7.08 mmol) $Cd(Ac)_2 2H_2O$, 4.34 g TDPA and 10.61 mL (8.37 g) of ODE to 300°C under N_2 atmosphere. After completion of the reaction (colorless solution was obtained) the temperature was lowered to ~170°C and the solution was degassed under vacuum. Finally, 12.9 mL (10.18 g) ODE and 2 mL (1.66 g) TOP were added. The stock solution of the Te precursor was made by dissolving 0.31 g (2.41

mmol) Te in 5.70 g (7.04 mL) TBP in a glove-box under nitrogen (< 5 ppm O2 and H2O).

Synthesis of TDPA capped CdTe QDs [222]: The synthesis was performed in a glove-box under nitrogen (< 5 ppm O_2 and H_2O). 0.4 g of Cd-TDPA stock solution and 3.6 g ODE were loaded in a reaction flask and heated to 300°C. At this temperature a mixture of 0.5 g Te-Stock and 1.5 g (1.9 mL) ODE was swiftly injected under stirring. The temperature was allowed to cool to ~270°C and kept constant. A 1 mL aliquot (sample 1, ~1mL) was taken 10 min after the Te injection. The synthesis was continued 12 min after the injection of Te by alternate dropwise additions of Cd-TDPA and Te stock, which are referred to as addition cycles. Every addition cycle took about 3 min, and was started by 10 drops of Cd-TDPA precursor solution, followed by alternate additions of Cd-TDPA and Te stock (10 drops at a time) until the total intended volume had been added. The precursors were allowed to react for 12 min after each addition cycle. In the first four addition cycles 0.26 g Te stock, and a mixture of 0.31 g Cd-TDPA stock and 0.35 g ODE were added. From addition cycle five to eight 0.5 g Te stock, and a mixture of 0.43 g Cd-TDPA stock and 0.17 g ODE were added. In the final addition cycle 1 g Te stock, and 0.36 g Cd-TDPA stock were added. The mixture of Cd-TDPA stock solution and ODE was pre-heated to 250°C and added as a hot solution, whereas the Te-TBP stock was kept at ambient temperature. Aliquots of ~1mL were taken from the reaction mixture 3 min before the start of every addition cycle. The synthesis temperature was lowered to 250°C after the second addition cycle. The synthesis was stopped by removing the heating mantle 18 min after completion of the final addition cycle.

Purification of the crude reaction mixture consisted of a hexane/methanol extraction in order to remove unreacted Cd precursors: Extraction was performed by mixing a solution of the crude reaction mixture in anhydrous hexane, and anhydrous methanol (1:1:1 volume ratio). The colored top layer containing the nanocrystals was removed and the nanocrystals were precipitated by adding anhydrous acetone (1:1 volume ratio). The sediment was isolated by centrifugation (3000 rpm, 15 min), and redissolved in anhydrous toluene (or in ODE if they were to be used as seeds).

Preparation of CdTe nanocrystals with radius smaller than 5 nm from 3.5 nm diameter seeds [37]

Briefly, the CdTe nanocrystal seeds were purified once by adding methanol to the crude reaction mixture (3:1 volume ratio), followed by centrifugation and redispersion of the precipitate in a mixture of ODE and octadecylamine (ODA) (4 mL ODE; 1.5 g ODA, and 0.1 mol seeds). Subsequently, pre-calculated volumes of a precursor solution (0.1 M Cd oleate in ODE and 0.1 M Trioctylphosphine-Te in ODE) were slowly added (1 monolayer of Cd or Te at a time), while keeping the temperature constant at 220°C. Each monolayer was allowed to grow for 10-15 minutes before the next precursor solution was added.

Preparation of CdTe nanocrystals with radius larger than 5 nm from 10 nm diameter seeds

Chemicals: Cadmium acetate dihydrate (Cd(Ac)2xH2O, 99.99+%), octadecene (ODE, tech. grade 90%), and oleic acid (tech. grade 90%) were purchased from Sigma-Aldrich. Trioctylphosphine (TOP, tech. grade > 90%) and octadecylamine (ODA, >90%) were purchased from Fluka. Tellurium powder (99.999%, $\leq$250 micron) was purchased from Hereaus. Anhydrous toluene, anhydrous hexane, anhydrous methanol, and anhydrous acetone were all purchased from Sigma-Aldrich.

Stock solutions: Stock solution of 0.093 M Cd-Oleate in ODE was made by heating 0.926 g $Cd(Ac)_2 2H_2O$ with 2.92 mL oleic acid in 37.05 mL ODE to 100°C under N2 atmosphere for 1h. Subsequently this Cd-stock solution was dried and degassed under vacuum (2 h at 100°C). A stock solution of 0.1M Te in TOP and ODE (TOP:ODE, 1:9 volume ratio) was prepared by dissolving 0.514 g Te powder in 4 mL TOP and 36 mL ODE under N2 atmosphere.

Synthesis: The synthesis was performed in a glove-box under nitrogen (< 5 ppm O_2 and H_2O). ODA (0.81 g), ODE (1.5 mL), and 1.3 mL of CdTe nanocrystal stock solution in ODE (37.5Œ10^{-9} mol of CdTe nanocrystal seeds) were loaded in a reaction flask and heated to 230°C. The amount of Cd and Te needed for an additional layers was calculated based on CdTe wurtzite structure in which the average thickness of one monolayer is 0.375 nm. During the synthesis alternate additions of Cd and Te stock solutions were performed (each during ~2 min). Before every Cd stock solution addition, aliquots (0.5 mL) from the reaction mixture were taken. The synthesis was started by the addition of Cd stock solution of the first monolayer. Each monolayer was allowed to grow for 30 minutes before the next precursor solution was added. After the third monolayer the waiting time was increased to 45 min. The synthesis was finished after the addition of fourteen monolayers.

Purification and size selection procedure: The purification procedure consisted of precipitating the nanocrystals from a solution of the crude reaction mixture in toluene (1:1 volume ratio) by adding anhydrous methanol. The sediment was isolated by centrifugation (3000 rpm, 15 min) and redissolved in anhydrous toluene. By using post-preparative size selective precipitation, ensembles of monodisperse (5 - 7% standard deviation) spherical CdTe nanocrystals ranging from 10.5 to 15.7 nm diameter were isolated from the reaction mixture.

Characterization

Absorption spectra were measured on a double beam Perkin-Elmer Lambda 16 UV/Vis spectrometer (scan rate: 1 nm/s). Emission spectra were recorded by using a Princeton Instrument Liquid N2-cooled CCD-detector and a 0.25 m Acton Research monochromator (150 lines/mm grating blazed at 550 nm). The excitation wavelength was selected from a 450 W Xe lamp by a double-grating monochromator (0.22 m, SPEX 1680). All measurements were performed at room temperature under N_2 atmosphere. Samples for optical measurements were prepared by directly dissolving the crude reaction mixture in anhydrous toluene under nitrogen. All measurements were carried out on samples with a low optical density (0.2 at 300 nm). Transmission electron microscopy was performed on a Tecnai20F (FEI) microscope equipped with a Field Emission Gun, a Gatan 694 CCD camera and an EDAX spectrometer. The microscope was operated at 200kV. Samples for TEM imaging were prepared by dipping a carbon coated polymer film copper grid (300 mesh) into a toluene solution of purified nanocrystals. The excess liquid was removed by blotting with filter paper.

For the THz measurements colloidal suspensions were contained in fused silica cuvettes that have an optical path length of 1mm. The absorbance at the pump wavelength of 400nm was determined with a spectrometer and kept below an OD of 0.5. The corresponding particle densities were sufficiently low to avoid particle agglomeration that could potentially perturb the results (interparticle electron transport). Furthermore, the excitation profile can be approximated to be constant over the whole cuvette length.

4.2.2 Exciton polarizability: theory including excitonic effects

The objective is to calculate the change in the polarizability of a QD after a single excitation. Since experiments are performed at room temperature, it is not sufficient to consider that the QD is in its lowest energy exciton states, many exciton states must be considered.

Principle of the calculation

The excitonic states of the QD are calculated using a Configuration Interaction (CI) method as described below. The excitonic states of energy E_i are denoted Ψ^i_{exc} (the zero of energy corresponding to the QD is its ground states, i.e., without exciton). Assuming that the external electric field is a small perturbation, the polarizabilty of the exciton is given by:

$$\hat{\alpha}(h\nu) = -e^2F^2 \sum_{i,j} \left| \left\langle \Psi^i_{exc} \right| \sum_n \mathbf{e}.\mathbf{r}_n \left| \Psi^j_{exc} \right\rangle \right|^2 \times \frac{f_i - f_j}{h\nu - (E_j - E_i) + i\eta}$$

where $h\nu$ is the photon energy, **e** is the polarization vector, F is the local-field factor, $\mathbf{r}_n$ represents the position of the electron n, f_i is the thermal occupancy of the exciton state Ψ^i_{exc}, and η is the broadening which accounts for the coupling to phonons (or eventually other mechanisms). $\sum_n$ is a sum over all the electrons of the system, $\left\langle \Psi^i_{exc} \right| \sum_n \mathbf{e}.\mathbf{r}_n \left| \Psi^j_{exc} \right\rangle$ is the dipolar matrix element between two excitonic states.

Configuration Interaction

The ground state $|O>$ of the QD corresponds to filled valence states and empty conduction states. We consider a basis of electron-hole pair (eh) states $\psi_{\nu c}$ corresponding to the excitation of an electron from a valence state ν to a conduction state c. In a basis of single-particle states (those obtained in tight-binding), each eh state is a Slater determinant. With respect to the Slater determinant $|O>$, the single-particle state ν has been replaced by the single-particle state c.

In CI, the excitonic states are defined as linear combinations of the eh states:

$$\Psi^{i}_{exc} = \sum_{\nu c} a^{i}_{c\nu}\psi_{\nu c}. \tag{4.1}$$

To solve the problem, we must write the matrix of the Hamiltonian in the basis of the eh states and we must diagonalize it. The energies E_i are the eigenvalues. The matrix element between two eh states $\psi_{\nu c}$ and $\psi_{\nu' c'}$ are

$$\begin{aligned}\langle\psi_{\nu c}|H|\psi_{\nu' c'}\rangle &= ([\varepsilon_c + \Sigma_c] - [\varepsilon_\nu + \Sigma_\nu])\delta_{cc'}\delta_{\nu\nu'} \\ &- \int c^*(\mathbf{x}_1)\nu^*(\mathbf{x}_2)V_{coul}(\mathbf{r}_1,\mathbf{r}_2)c'(\mathbf{x}_1)\nu'(\mathbf{x}_2)d\mathbf{x}_1 d\mathbf{x}_2 \\ &+ \int c^*(\mathbf{x}_1)\nu^*(\mathbf{x}_2)V_{exch}(\mathbf{r}_1,\mathbf{r}_2)\nu'(\mathbf{x}_1)c'(\mathbf{x}_2)d\mathbf{x}_1 d\mathbf{x}_2 \end{aligned} \tag{4.2}$$

where $\mathbf{x}_1 \equiv (\mathbf{r}_1, \xi_1)$ in which ξ_1 represents the spin variable of the particle 1. The second line is the Coulomb term, the third one is the exchange one. $V_{coul}(\mathbf{r}_1, \mathbf{r}_2)$ describes the energy potential of a charge $+e$ at $\mathbf{r}_1$ induced by a charge $+e$ at $\mathbf{r}_2$:

$$V_{coul}(\mathbf{r}_1,\mathbf{r}_2) = \int \epsilon^{-1}(\mathbf{r}_1,\mathbf{r})\frac{e^2}{|\mathbf{r}-\mathbf{r}_2|}d\mathbf{r} \tag{4.3}$$

in which $\epsilon^{-1}(\mathbf{r}_1, \mathbf{r}_2)$ is the generalized dielectric constant (here taken in the static limit). We assume that $V_{exch} = V_{coul}$.

The term Σ_c (Σ_ν) represents the self-energy of the electron (hole) coming from the interaction of the electron with the polarization charges induced at the dielectric interfaces (or surfaces) by its own presence:

$$\Sigma_c = \frac{1}{2}\int |c(\mathbf{r}_1)|^2 \lim_{\mathbf{r}_2\to\mathbf{r}_1}\left(V_{coul}(\mathbf{r}_1,\mathbf{r}_2) - \frac{e^2}{\epsilon_{in}|\mathbf{r}_1-\mathbf{r}_2|}\right)d\mathbf{r}_1 \tag{4.4}$$

where ϵ_{in} is the dielectric constant of the material at the position $\mathbf{r}_1$. In the case of a spherical QD, V_{coul} is easily obtained assuming a dielectric sphere of dielectric constant ϵ_{in} in a medium of dielectric constant ϵ_{out} (the solvent for example).

Optical matrix elements in CI

The optical matrix elements in CI are given by:

$$\left\langle \Psi^{i}_{exc} \middle| \sum_{n} \mathbf{e}.\mathbf{r}_n \middle| \Psi^{j}_{exc} \right\rangle = \sum_{\nu, c \neq c'} a^{*}_{\nu c'} a_{\nu c} < c' | \mathbf{e}.\mathbf{r} | c > + \sum_{c, \nu \neq \nu'} a^{*}_{\nu' c} a_{\nu c} < \nu | \mathbf{e}.\mathbf{r} | \nu' > \quad (4.5)$$

The single-particle dipolar matrix elements $< c' | \mathbf{e}.\mathbf{r} | c >$ and $< \nu | \mathbf{e}.\mathbf{r} | \nu' >$ are easily calculated in tight-binding.

4.3 Results

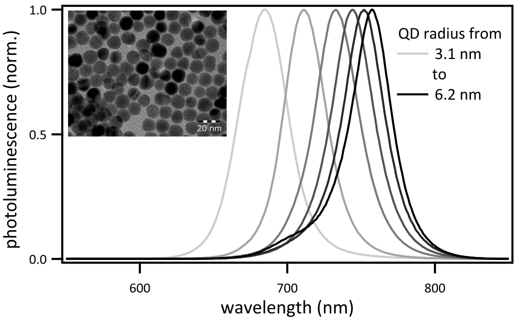

Figure 4.1: Redshift of the photoluminescence peak with nanocrystal size for particles ranging from 3.1 to 6.2 nm radius. The inset shows a TEM image of a batch with mean particle radius of 7 nm.

The bandgap energies of nanocrystals of different diameter were determined using photoluminescence measurements. Fig. 4.1 shows the photoluminescence peaks for a set of CdTe nanocrystal batches ranging in radius from 3.1 to 6.2 nm. The redshift of the bandgap with increasing size is clearly visible, converging towards the bulk value of ~ 1.48 eV (840 nm). The inset shows a TEM image of nanocrystals with a mean radius of 7 nm. Analysis of the TEM results reveals that the nanocrystals are facetted but nearly spherical with a standard deviation in radius of about 7 - 10 %.

We extract the exciton-induced change in the THz probe response of the nanocrystals suspension following the method described in [75] and express it in terms of the complex conductivity $\hat{\sigma}(\omega)$. The pump fluence was chosen sufficiently low that the probability of bi-exciton generation was less than 5%. Fig. 4.2 shows two exemplary measured complex conductivities $\hat{\sigma}(\omega)$ for batches with a mean radius of a) 4.25 nm and b) 7.5 nm. The real part of $\hat{\sigma}(\omega)$ is related to absorption, whereas the imaginary part indicates the phase response of the THz probe. For sufficiently small quantum dots (Fig. 4.2 a) the real part of $\hat{\sigma}(\omega)$ is zero (no THz absorption), while significant real conductivity is observed for larger particles (Fig. 4.2 b). The appearance of real conductivity, i.e. absorption, for the large particles indicates the existence of low-energy transitions that are resonant with the THz probe pulse.

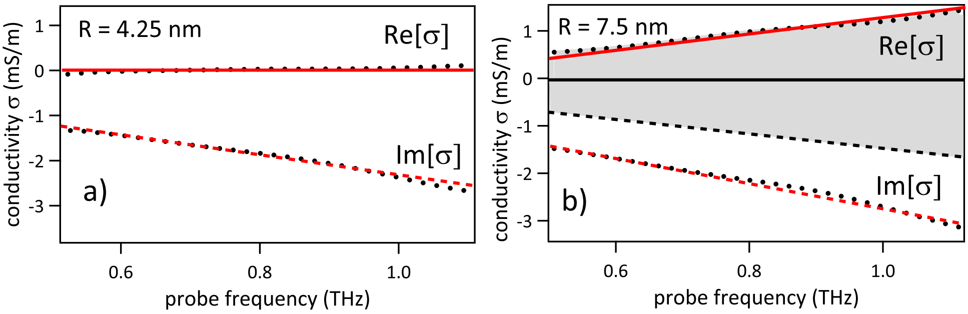

Figure 4.2: Exemplary THz conductivity spectra (black dots) for CdTe nanocrystal samples showing a) no real conductivity and b) finite real conductivity. Red solid (real part) and dashed (imaginary part) lines are the results of models for the exciton polarizability described in the text. The black lines in b) show the electron contribution to the total exciton polarizability for this radius, and the grey-shaded area the hole contribution.

Surprisingly, considering the Bohr radius of 7 nm, the largest size for which we see no real conductivity is 4.4 nm. This observation is illustrated by Fig. 4.3 a), which shows a summary of the THz spectra for all measured sizes. Plotted is the spectrally integrated real part of $\hat{\sigma}(\omega)$ divided by the excitation density N_{ex}, which was determined experimentally from the absorption coefficient at the excitation wavelength of 400 nm.

Fig. 4.3 a) reveals a clear division in the response at a particle radius of 5 nm. Below this size, no real conductivity is observed; for all larger particles the real conductivity is finite. We note that, while the low measured signal amplitudes cause significant scatter in the *magnitude* of the measured conductivities, the *presence* of real conductivity was always observed for $R > 5nm$, while the measured real conductivity was never significantly larger than zero for $R \leq 4.4nm$. Remarkably, the real conductivity sets in already for sizes significantly smaller than a_B, which we attribute to the emergence of low-lying, quasi-continuous distribution of energy levels for $R > 5nm$. Considering that the valence hole levels are more densely spaced than the conduction electron levels (see below) we ascribe these levels to hole states.

For the smaller nanocrystal sizes, the conductivity is purely imaginary and negative, increasing linearly with frequency. This is due to the real polarizability $Re(\hat{\alpha}) = \alpha^{'}$ of the excitons within the QDs [208], which is proportional to $Im[\hat{\sigma}(\omega)]$, according to [28]:

$$\hat{\sigma}^{''}(\omega) = -\omega N_{ex} \frac{36\pi\epsilon_s^2}{(\epsilon_{np} + 2\epsilon_s)^2} \hat{\alpha}^{'} \quad \boxed{4.6}$$

Here, ϵ_s is the dielectric constant of the solvent and ϵ_{np} that of the nanocrystal. A fit to this model is shown by the red lines in Fig. 4.2 a). Fig. 4.3 b) summarizes the extracted values for the spectrally integrated $Im[\hat{\sigma}(\omega)]$, divided by the sheet excitation density N_{ex}. Previous measurements of the THz conductivity of carriers in nanocrystals [208, 28, 169, 9] have mostly been performed for relatively small particles ($R < 3.5nm$), for which generally zero real conductivity was observed. Previously, real conductivity was reported for small and large CdSe QDs [9], but it has since been established that the real conductivity for small particles is zero, with the imaginary conductivity being determined by the exciton polarizability [208, 28, 169].

Size-dependent polarizability measurements of carriers in semiconductor nanocrystals have previously revealed scaling laws of $Im[\hat{\sigma}(\omega)] \sim \alpha \sim R^{3.6}$ for CdSe [208, 28] and $Im[\hat{\sigma}(\omega)] \sim R^4$ for InAs [169]. Our data can be well described by $Im[\hat{\sigma}(\omega)] \sim R^{3.6}$ scaling for sizes up to 5 nm, as indicated by the black solid line, in analogy to CdSe which is very similar regarding its band structure and electronic parameters such as electron and hole effective mass. Above 5 nm, the data deviates from this trend, in agreement with the appearance of the real conductivity shown in Fig. 4.2 a). For $R > 5nm$ the imaginary conductivity is no longer solely defined by the polarizability of strongly confined carriers but also by the response of carriers experiencing weakened confinement approaching bulk-like states.

4.4 Discussion

In the following, we discuss the observation of real conductivity for CdTe nanocrystals with radii larger than 5 nm. This behavior is directly linked to the loosening of electronic quantum confinement, which in turn decreases the level spacing between intraexcitonic states. One should bear in mind that several distinct physical mechanisms play a role in the confinement, such as confinement effects on the single-particle (electron and hole) levels, electron-hole correlations and dielectric polarization effects. The confinement regime investigated here is particularly intricate as, in contrast to the limiting cases of strong and weak confinement, approximations with respect to the confinement energy cannot be applied. In the strong confinement regime, electrons and holes are largely uncorrelated and their confinement can thus be treated separately, with electron-hole correlations treated as a perturbation. On the other hand, in the weak confinement regime the excitonic contribution to the total confinement energy prevails. We therefore performed tight-binding calculations that fully include all confinement contributions. They allow computing the electronic energy levels and, based on that, to calculate the complex exciton polarizability in the THz spectral range (see 4.2.2). The polarizability $\hat{\alpha}$ at the energy $\hbar\omega$ is written as

$$\hat{\alpha}(\omega) = -e^2F^2 \sum_{n,m} \frac{|\langle n \| m \rangle|^2 (f_n - f_m)}{\hbar\omega - (E_m - E_n) + i\eta} \tag{4.7}$$

where $|n\rangle$ is a state of the system with energy E_n and thermal occupancy f_n, $\langle n \| m \rangle$ is the dipolar matrix element between states n and m, and F is the local-field factor.

The factor η may account for the broadening of the transitions, in particular due to coupling to phonons. We performed two types of calculations in which the states $|n\rangle$

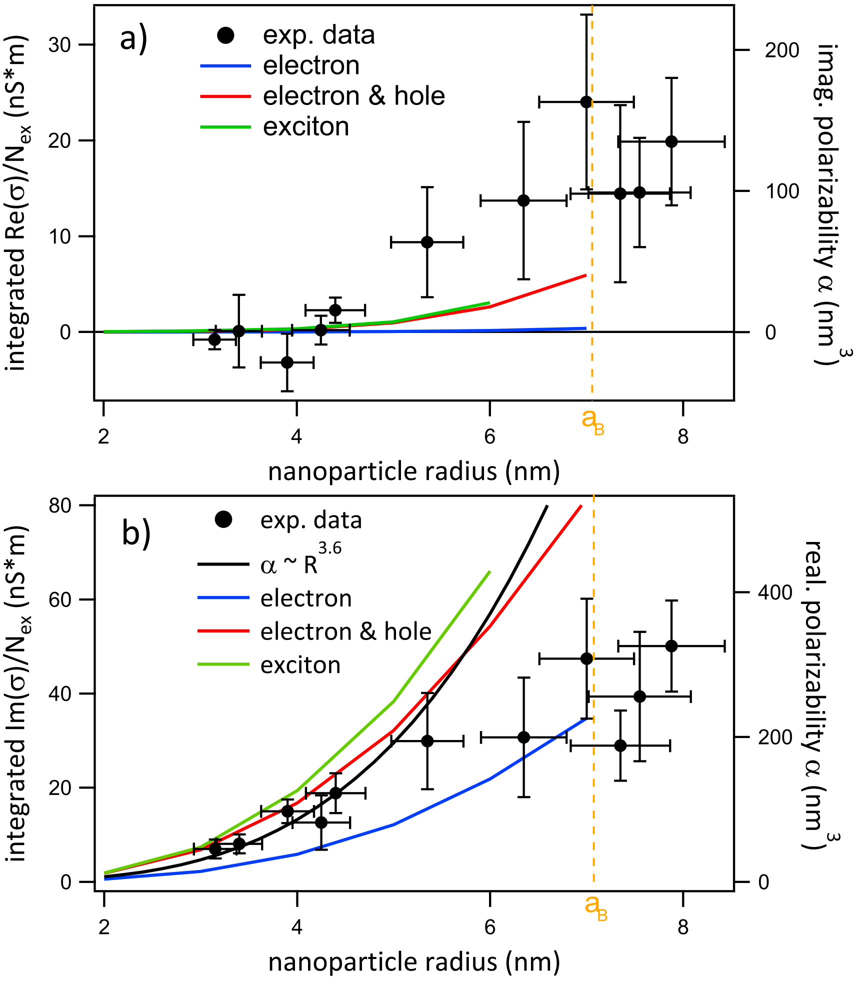

Figure 4.3: Spectrally integrated a) real conductivity and b) imaginary conductivity, divided by the excitation density N_{ex}. On the right axis: imaginary polarizability (a) and real polarizability (b). Black dots represent the experimental data. The vertical error bars were obtained from the standard deviation of the values extracted from various measurements on the same batch. The horizontal error bars are determined by the standard deviation of the particle size distribution which is 7%. The black solid line in b) sketches the $R^{3.6}$ dependence that was observed in previous publications for the exciton polarizability in the strong confinement regime. Colored solid lines are the results of the TB calculations ($\eta = 5meV$): single electron in QD (blue) electron and hole without considering Coulomb interactions (red), electron and hole including Coulomb interactions (green). The yellow dashed line indicates the bulk exciton Bohr radius $a_B = 7nm$.

are either single-particle TB states or excitonic states built from the TB states using a full configuration-interaction approach. The comparison between the two calculations sheds light on the effect of the electron-hole interaction on the polarizability.

Figure 4.3 displays the results of the calculations together with the experimental values. The colored solid lines show the calculated polarizabilities for a single electron in the QD (blue), an electron and hole without considering Coulomb interactions (red), and finally electron and hole including Coulomb interactions (green). The difference between the red and green curves is small. It is thus apparent that, as expected, the influence of Coulomb interactions is minor, particularly for smaller sizes. Electrons and holes contribute approximately equally to the real polarizability. The imaginary part (and thus the real conductivity) is however solely due to the hole, which starts to increase appreciably for sizes above 5 nm, in agreement with the experimental observation. This increase originates from the redshift of the hole transitions for increasing particle sizes whose resonances are approaching the THz probe window, a direct manifestation of weakening confinement (see Fig. 4.4 a)). The observation of an emerging imaginary part for $R > 5nm$ is thus qualitatively explained. The actual values however do not match.

Above 5nm, where we observe the transition to finite THz absorption, the computed complex conductivities start to deviate from the experimental values. The calculated imaginary parts are about a factor two larger than the experimental values, whereas the real parts are approximately three times lower. The observed variance points to a type of light-matter coupling mechanism that is not accounted for in our calculations.

The discrepancy may be traced to the fact that the complex polarizability as computed here only considers "vertical" optical transitions between electronic states. The effects resulting from carrier-phonon coupling enter only through a simple broadening η of the transition lines. The calculations used $\eta = 5meV$ but further broadening did not appreciably alter the polarizabilities. We also performed additional calculations to probe the pertubative influence of the THz electric field induced quasi-static lattice polarization on the selection rules of the electronic transitions, and thus possibly their oscillator strengths. The effect turned out to be negligible: the oscillator strengths of the transitions remained small and did not increase the imaginary polarizability. A plausible and likely scenario that explains the present deviation, and which is not accounted for in the TB calculations, is that at $R > 5nm$ electronic transitions become resonant with optical phonon modes and the resulting coupling creates mixed polaron states. In that case, one can expect additional transitions to emerge, for the polaron allows coupling of THz probe photons to optical phonon modes [64]. To illustrate this scenario, it is instructive to first inspect the computed size-dependent electronic energy levels.

The calculations reveal that the energy spacing between electron levels is always larger than those between hole levels. Even for the R = 6 nm particles the transition energy between the electron ground state and the next-highest state is still larger than 60 meV. This is expected: due to its lower effective mass the electron wavefunction is more spread out than the hole wavefunction and thus confinement effects are stronger. The electron transition energies are therefore too high to be relevant for phonon coupling; hence only hole levels are relevant for our discussion. The calculated confinement energy of the hole levels, i.e., their transition energy with respect to the ground state, is plotted for several sizes in Fig. 4.4 a). The lengths of the bars

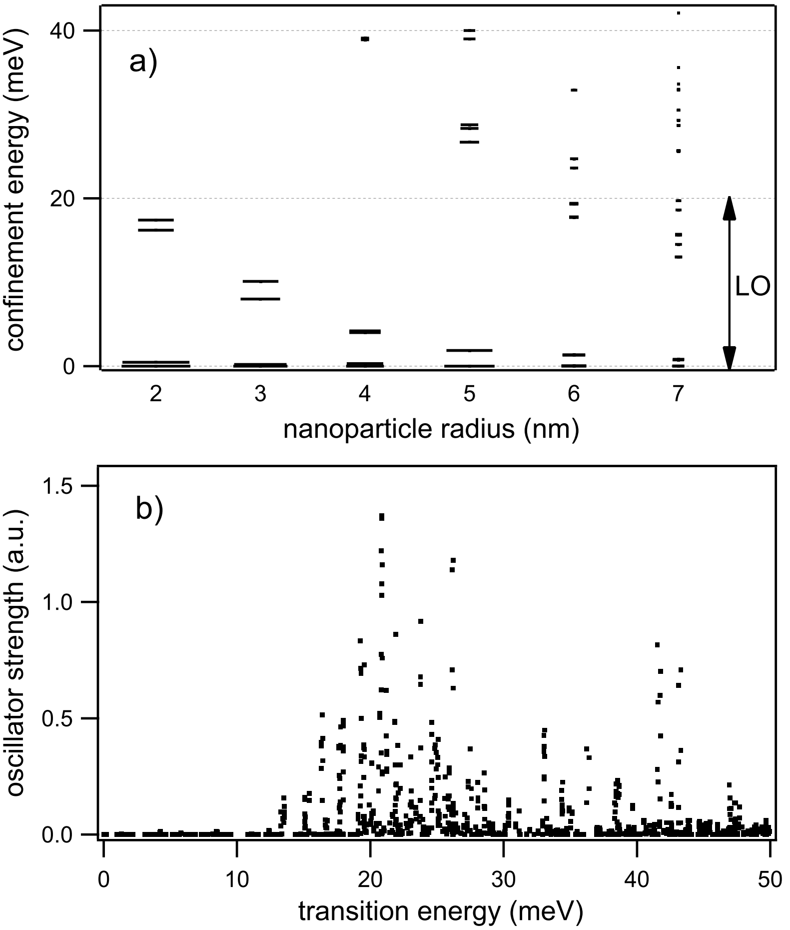

Figure 4.4: a) calculated hole states as a function of the CdTe nanoparticle radius. The length of the bar indicates the relative thermal occupation probability at room temperature and the double arrow the LO phonon energy of 21 meV; b) oscillator strengths of all possible hole transitions, multiplied by the relative thermal occupation of the initial state, for nanocrystals of R=6nm.

that indicate the energy levels correspond to the relative thermal occupation probability at room temperature. It is evident that several energy levels are significantly populated.

The lowest hole states are composed of multiplets with splittings in the sub-to-few-meV range for the largest sizes. Due to symmetry reasons the oscillator strength for transitions between these multiplets is practically zero. This is shown in Fig. 4.4 b) which plots the oscillator strengths of all possible hole transitions, multiplied by the relative thermal occupation of the initial state, for nanocrystals of R=6nm. The oscillator strength is zero for all transitions below 10 meV. The longitudinal optical (LO) phonon energy in CdTe is 21 meV and is largely unaffected by confinement effects

[35]. For radii approaching 6 nm the energy between the two lowest states and the next-higher ones falls below 20 meV, which matches the LO phonon frequency (indicated by the arrow labeled LO in Fig. 4.4 a). Other transitions become resonant with the LO phonon frequency, too. In fact, a summation over the oscillator strengths for all transitions of thermally populated hole states shows a large enhancement of the total oscillator strength around 20 meV when going from 5 nm to 6 nm size (see Fig. 4.4 b). It has been shown before that such a situation, in which electronic transitions in quantum dots become resonant with LO phonon modes, can lead to the formation of mixed carrier-phonon, i.e. polaron, states [64]. The coupling through Fröhlich interaction can be described by an entangled two-level system with wavefunction $|\Psi_i\rangle$ which is comprised of the uncoupled excited hole state $|h_{i,exc}\rangle\,|0_{LO}\rangle$ and the hole ground state, which is coupled to the one-LO-phonon mode $|h_{i,g}\rangle\,|1_{LO}\rangle$ [64]:

$$|\Psi_i\rangle = x\,|h_{i,exc}\rangle\,|0_{LO}\rangle \pm \sqrt{1-x^2}\,|h_{i,g}\rangle\,|1_{LO}\rangle \tag{4.8}$$

At room temperature a large number of polaron states is populated (hence the subscript i in $|\Psi_i\rangle$), with presumably each of them possessing different coupling strengths to the probe light. The polaron state essentially permits coupling of the THz probe light to optical phonons by exciting the phonon part of the polaron wavefunction $|\Psi_i\rangle$, which would give rise to new absorption features associated with the phonon excitation when the polaron eventually relaxes via its LO phonon component through anharmonic coupling into a continuum of multiphonon states.

In order to isolate the anticipated hole polaron THz response from the measured THz spectra, we subtract the electron contribution from the imaginary part of the measured conductivities by reducing it by a factor of two, for the TB calculations showed that the electron contributes about half to the total imaginary conductivity. The resulting hole response can be described well by an overdamped Lorentzian oscillator with a center frequency of (18.5 ± 5.2) meV and width of (38.2 ± 10.6) meV. A fit to this model is shown in Fig. 4.2 b), where the red lines depict the total polarizability and the black lines the electron contribution. The error to the values are derived from the standard deviation of the fitted parameters extracted from approximately fifty measurements. The center frequency of 18.5 meV is close to the LO phonon energy of 21 meV, corroborating our picture that polaron states are the main source of the emerging real conductivities at R > 5nm.

4.5 Conclusions

In conclusion, we have investigated the THz response of photogenerated excitons in CdTe nanocrystals of radius between 3 and 8 nm, ranging in size from the strong to the intermediate quantum confinement regime. For nanocrystal radii below 5 nm we only measure an imaginary conductivity originating from the polarizability of strongly confined excitons, in agreement with previous publications. Above 5 nm we observe the onset of real conductivity, which we attribute to THz transitions between closely-spaced polaron states.

Bibliography

[1] E. Abrahams, P. W. Anderson, D. C. Licciardello, and T. V. Ramakrishnan. Scaling theory of localization: Absence of quantum diffusion in two dimensions. *Physical Review Letters*, 42(10):673, 1979.

[2] Vinay Ambegaokar, B. I. Halperin, and J. S. Langer. Hopping conductivity in disordered systems. *Physical Review B*, 4(8):2612, 1971.

[3] P. W. Anderson. Absence of diffusion in certain random lattices. *Physical Review*, 109(5):1492, 1958.

[4] M. R. Armstrong, E. J. Reed, K. Y. Kim, J. H. Glownia, W. M. Howard, E. L. Piner, and J. C. Roberts. Observation of terahertz radiation coherently generated by acoustic waves. *Nature Physics*, 5(4):285–288, 2009.

[5] DH Auston. *Picosecond photoconductors, physical properties and applications*. Picosecond Optoelectronic Devices. Academic Press, New York, 1983.

[6] R. D. Averitt and A. J. Taylor. Ultrafast optical and far-infrared quasiparticle dynamics in correlated electron materials. *Journal Of Physics-Condensed Matter*, 14(50):R1357–R1390, 2002.

[7] T. Bartel, P. Gaal, K. Reimann, M. Woerner, and T. Elsaesser. Generation of single-cycle thz transients with high electric-field amplitudes. *Optics Letters*, 30(20):2805–2807, 2005.

[8] M. C. Beard, G. M. Turner, and C. A. Schmuttenmaer. Transient photoconductivity in gaas as measured by time-resolved terahertz spectroscopy. *Physical Review B*, 62(23):15764–15777, 2000.

[9] M. C. Beard, G. M. Turner, and C. A. Schmuttenmaer. Size-dependent photoconductivity in cdse nanoparticles as measured by time-resolved terahertz spectroscopy. *Nano Letters*, 2(9):983–987, 2002.

[10] M. C. Beard, G. M. Turner, and C. A. Schmuttenmaer. Terahertz spectroscopy. *Journal Of Physical Chemistry B*, 106(29):7146–7159, 2002.

[11] P. K. Benicewicz, J. P. Roberts, and A. J. Taylor. Scaling of terahertz radiation from large-aperture biased photoconductors. *Journal of the Optical Society of America B-Optical Physics*, 11(12):2533–2546, 1994.

[12] S. C. Benjamin, B. W. Lovett, and J. M. Smith. Prospects for measurement-based quantum computing with solid state spins. *Laser and Photonics Reviews*, 3(6):556–574, 2009.

[13] J. R. Birch, C. C. Bradley, and M. F. Kimmitt. Absorption and refraction in germanium at 293Âřk in the range 12-50 cm-1. *Infrared Physics*, 14(3):189–197, 1974.

[14] F. C. Bos and D. M. Burland. Hole transport in polyvinylcarbazole: The vital importance of excitation-light intensity. *Physical Review Letters*, 58(2):152, 1987.

[15] P. R. Briddon. *Mater. Sci. Forum*, (83):457, 1992.

[16] M. Brinza, J. Willekens, M. L. Benkhedir, E. V. Emelianova, and G. J. Adriaenssens. Photoconductivity methods in materials research. *Journal of Materials Science-Materials in Electronics*, 16(11-12):703–713, 2005.

[17] M. Brucherseifer, P. H. Bolivar, and H. Kurz. Combined optical and spatial modulation thz-spectroscopy for the analysis of thin-layered systems. *Applied Physics Letters*, 81(10):1791–1793, 2002.

[18] AG Bruggemann. *Annalen der Physik*, 24:636, 1935.

[19] KJ Button. *Infrared and millimeter waves, vol. 1 (Sources of radiation)*. New York, Academic Press, 1980.

[20] Y. Cai, I. Brener, J. Lopata, J. Wynn, L. Pfeiffer, J. B. Stark, Q. Wu, X. C. Zhang, and J. F. Federici. Coherent terahertz radiation detection: Direct comparison between free-space electro-optic sampling and antenna detection. *Applied Physics Letters*, 73(4):444–446, 1998.

[21] H. Cao, T. F. Heinz, and A. Nahata. Electro-optic detection of femtosecond electromagnetic pulses by use of poled polymers. *Optics Letters*, 27(9):775–777, 2002.

[22] G. Q. Chang, C. J. Divin, C. H. Liu, S. L. Williamson, A. Galvanauskas, and T. B. Norris. Power scalable compact thz system based on an ultrafast yb-doped fiber amplifier. *Optics Express*, 14(17):7909–7913, 2006.

[23] Y. Q. Chen, M. Yamaguchi, M. F. Wang, and X. C. Zhang. Terahertz pulse generation from noble gases. *Applied Physics Letters*, 91(25):251116, 2007.

[24] R.A. Cheville. *Terahertz time-domain spectroscopy with photoconductive antennas*. Terahertz Spectroscopy: Principles and Applications. CRC Press, Boca Raton, 2008.

[25] TC Choy. *Effective medium theory: principles and applications*. International series of monographs on physics. Clarenton Press, 1999.

[26] A. T. Collins, P. J. Woad, G. S. Woods, and H. Kanda. Localised vibrational modes in diamonds grown from mixed carbon isotopes. *Diamond and Related Materials*, 2(2-4):136–141, 1993.

[27] D. J. Cook and R. M. Hochstrasser. Intense terahertz pulses by four-wave rectification in air. *Optics Letters*, 25(16):1210–1212, 2000.

[28] G. L. Dakovski, S. Lan, C. Xia, and J. Shan. Terahertz electric polarizability of excitons in pbse and cdse quantum dots. *Journal of Physical Chemistry C*, 111(16):5904–5908, 2007.

[29] J. T. Darrow, X. C. Zhang, and D. H. Auston. Power scaling of large-aperture photoconducting antennas. *Applied Physics Letters*, 58(1):25–27, 1991.

[30] J.H. Davies. *The Physics of Low-dimensional Semiconductors: An Introduction*. Cambridge University Press, 1997.

[31] F. De Weerdt and J. Van Royen. Defects in coloured natural diamonds. *Diamond and Related Materials*, 10(3-7):474–479, 2001.

[32] T. Dekorsy, H. Auer, H. J. Bakker, H. G. Roskos, and H. Kurz. Thz electromagnetic emission by coherent infrared-active phonons. *Physical Review B*, 53(7):4005–4014, 1996.

[33] O. Demichel, V. Calvo, A. Besson, P. Noe, B. Salem, N. Pauc, F. Oehler, P. Gentile, and N. Magnea. Surface recombination velocity measurements of efficiently passivated gold-catalyzed silicon nanowires by a new optical method. *Nano Letters*, 10(7):2323–2329, 2010.

[34] J.T. Devreese and F. Peeters. *Polarons and Excitons in Polar Semiconductors and Ionic Crystals*. Springer, 1984.

[35] Stoichko D. Dimitrov, Chad J. Dooley, Anton A. Trifonov, and Torsten Fiebig. Femtosecond probing of optical phonon dynamics in quantum-confined cdte nanocrystals. *Journal of Physical Chemistry C*, 113(10):4198–4201, 2009.

[36] T. Dittrich, T. Bitzer, T. Rada, V. Y. Timoshenko, and J. Rappich. Non-radiative recombination at reconstructed si surfaces. *Solid-State Electronics*, 46(11):1863–1872, 2002.

[37] Celso de Mello Donega and Rolf Koole. Size dependence of the spontaneous emission rate and absorption cross section of cdse and cdte quantum dots. *Journal of Physical Chemistry C*, 113(16):6511–6520, 2009.

[38] M. Dressel and M. Scheffler. Verifying the drude response. *Annalen Der Physik*, 15(7-8):535–544, 2006.

[39] P. Drude. Zur elektronentheorie der metalle; ii. teil. galvanomagnetische und thermomagnetische effecte. *Annalen der Physik*, 308(11):369–402, 1900.

[40] L. Duvillaret, F. Garet, and J. L. Coutaz. A reliable method for extraction of material parameters in terahertz time-domain spectroscopy. *Ieee Journal of Selected Topics in Quantum Electronics*, 2(3):739–746, 1996.

[41] J. C. Dyre and T. B. Schroder. Universality of ac conduction in disordered solids. *Reviews of Modern Physics*, 72(3):873–892, 2000.

[42] A. L. Efros and M. Rosen. The electronic structure of semiconductor nanocrystals. *Annual Review of Materials Science*, 30:475–521, 2000.

[43] Al. L. Efros and A. L. Efros. Interband light absorption in a semiconductor sphere. *Semiconductors*, 16:1209–1214, 1982.

[44] T. Elsaesser. Femtosecond mid-infrared spectroscopy of low-energy excitations in solids. *Applied Physics A-Materials Science and Processing*, 79(7):1627–1634, 2004.

[45] S. A. Empedocles and M. G. Bawendi. Quantum-confined stark effect in single cdse nanocrystallite quantum dots. *Science*, 278(5346):2114–2117, 1997.

[46] Cavid Erginsoy. Neutral impurity scattering in semiconductors. *Physical Review*, 79(6):1013, 1950.

[47] J. Faist, L. Ajili, G. Scalari, M. Giovannini, M. Beck, M. Rochat, H. Beere, A. G. Davies, E. H. Linfield, and D. Ritchie. Terahertz quantum cascade lasers. *Philosophical Transactions of the Royal Society of London Series a-Mathematical Physical and Engineering Sciences*, 362(1815):215–229, 2004.

[48] U. Fano. Effects of configuration interaction on intensities and phase shifts. *Physical Review*, 124(6):1866, 1961.

[49] R. G. Farrer. On the substitutional nitrogen donor in diamond. *Solid State Communications*, 7(9):685–688, 1969.

[50] M. E. Fermann and I. Hartl. Ultrafast fiber laser technology. *Ieee Journal of Selected Topics in Quantum Electronics*, 15(1):191–206, 2009.

[51] RP Feynman. *Feynman Lectures on Physics*, volume 2. Addison Wesley Longman, 1970. Chapter 32, section 3.

[52] H. Frohlich, H. Pelzer, and S. Zienau. *Phil. Mag.*, (41):221, 1950.

[53] SA Furman. *Basics of Optics of Multilayer Systems*. World Scientific Publishing, 1996.

[54] I. Galbraith, R. Chari, S. Pellegrini, P. J. Phillips, C. J. Dent, A. F. G. van der Meer, D. G. Clarke, A. K. Kar, G. S. Buller, C. R. Pidgeon, B. N. Murdin, J. Allam, and G. Strasser. Excitonic signatures in the photolumineseence and terahertz absorption of a gaas/alxga1-xas multiple quantum well. *Physical Review B*, 71(7):073302, 2005.

[55] V. F. Gantmakher and Y. B. Levinson. *Carrier Scattering in Metals and Semiconductors*. Elsevier Science Ltd, Amsterdam, 1987.

[56] S.V. Gaponenko. *Optical Properties of Semiconductor Nanocrystals*. Cambridge University Press, 1998.

[57] E. C. Garnett, M. L. Brongersma, Y. Cui, and M. D. McGehee. *Nanowire Solar Cells*, volume 41 of *Annual Review of Materials Research, Vol 41*. -, 2011.

[58] Erik Garnett and Peidong Yang. Light trapping in silicon nanowire solar cells. *Nano Letters*, 10(3):1082–1087, 2010.

[59] J. C. Maxwell Garnett. *Trans. R. Soc. London, Ser. A*, 203:385, 1904.

[60] J. I. Gittleman and B. Abeles. Comparison of the effective medium and the maxwell-garnett predictions for the dielectric constants of granular metals. *Physical Review B*, 15(6):3273, 1977.

[61] J. P. Goss, P. R. Briddon, R. Jones, and S. Sque. Donor and acceptor states in diamond. *Diamond and Related Materials*, 13(4-8):684–690, 2004.

[62] J. P. Goss, R. Jones, and P. R. Briddon. Stress tensors and dilatation of interstitial defects in diamond. *Physical Review B*, 65(3):035203, 2001.

[63] J. P. Goss, M. J. Shaw, and P. R. Briddon. *Theory of Defects in Semiconductors*, volume 104 of *Topics in Applied Physics*. Springer, Berlin/Heidelberg, 2007.

[64] T. Grange, R. Ferreira, and G. Bastard. Polaron relaxation in self-assembled quantum dots: Breakdown of the semiclassical model. *Physical Review B*, 76(24):241304, 2007.

[65] C. G. Granqvist and O. Hunderi. Optical properties of ag-sio2 cermet films: A comparison of effective-medium theories. *Physical Review B*, 18(6):2897, 1978.

[66] D Grischkowsky. *Nonlinear generation of subpicosecond pulses of THz electromagnetic radiation by optoelectronics - applications to time-domain spectroscopy*. Frontiers in Nonlinear Optics. Institute of physics, Bristol and Philadelphia, 1993.

[67] D. Grischkowsky, S. Keiding, M. Vanexter, and C. Fattinger. Far-infrared time-domain spectroscopy with terahertz beams of dielectrics and semiconductors. *Journal of the Optical Society of America B-Optical Physics*, 7(10):2006–2015, 1990.

[68] P. Y. Han and X. C. Zhang. Free-space coherent broadband terahertz time-domain spectroscopy. *Measurement Science and Technology*, 12(11):1747–1756, 2001.

[69] P. Harrison. *Quantum Wells, Wires and Dots: Theoretical and Computational Physics of Semiconductor Nanostructures*. John Wiley and Sons, 2002.

[70] C. Hartwigsen, S. Goedecker, and J. Hutter. Relativistic separable dual-space gaussian pseudopotentials from h to rn. *Physical Review B*, 58(7):3641–3662, 1998.

[71] H. Haug. *Quantum Theory of the Optical and Electronic Properties of Semiconductors*. World Scientific Publishing Company, 1994.

[72] E. Hendry, M. Koeberg, and M. Bonn. Exciton and electron-hole plasma formation dynamics in zno. *Physical Review B*, 76(4):045214, 2007.

[73] E. Hendry, M. Koeberg, B. O'Regan, and M. Bonn. Local field effects on electron transport in nanostructured tio2 revealed by terahertz spectroscopy. *Nano Letters*, 6(4):755–759, 2006.

[74] E. Hendry, M. Koeberg, J. Pijpers, and M. Bonn. Reduction of carrier mobility in semiconductors caused by charge-charge interactions. *Physical Review B*, 75(23):233202, 2007.

[75] E. Hendry, M. Koeberg, J. M. Schins, H. K. Nienhuys, V. Sundstrom, L. D. A. Siebbeles, and M. Bonn. Interchain effects in the ultrafast photophysics of a semiconducting polymer: Thz time-domain spectroscopy of thin films and isolated chains in solution. *Physical Review B*, 71(12):125201, 2005.

[76] E. Hendry, M. Koeberg, J. M. Schins, L. D. A. Siebbeles, and M. Bonn. Free carrier photogeneration in polythiophene versus poly(phenylene vinylene) studied with thz spectroscopy. *Chemical Physics Letters*, 432(4-6):441–445, 2006.

[77] E. Hendry, M. Koeberg, F. Wang, H. Zhang, C. D. Donega, D. Vanmaekelbergh, and M. Bonn. Direct observation of electron-to-hole energy transfer in cdse quantum dots. *Physical Review Letters*, 96(5):057408, 2006.

[78] E. Hendry, F. Wang, J. Shan, T. F. Heinz, and M. Bonn. Electron transport in tio2 probed by thz time-domain spectroscopy. *Physical Review B*, 69(8):081101, 2004.

[79] C. H. Henry and D. V. Lang. Nonradiative capture and recombination by multiphonon emission in gaas and gap. *Physical Review B*, 15(2):989, 1977.

[80] F. J. Heremans, G. D. Fuchs, C. F. Wang, R. Hanson, and D. D. Awschalom. Generation and transport of photoexcited electrons in single-crystal diamond. *Applied Physics Letters*, 94(15), 2009.

[81] B.J. Hickey, G.J. Morgan, and M.A. Howson. *Basic Electron Transport*. Springer, 2001.

[82] A. Houard, Y. Liu, B. Prade, and A. Mysyrowicz. Polarization analysis of terahertz radiation generated by four-wave mixing in air. *Optics Letters*, 33(11):1195–1197, 2008.

[83] R. Huber, A. Brodschelm, F. Tauser, and A. Leitenstorfer. Generation and field-resolved detection of femtosecond electromagnetic pulses tunable up to 41 thz. *Applied Physics Letters*, 76(22):3191–3193, 2000.

[84] T. H. Isaac, W. L. Barnes, and E. Hendry. Determining the terahertz optical properties of subwavelength films using semiconductor surface plasmons. *Applied Physics Letters*, 93(24):241115, 2008.

[85] T. H. Isaac, J. G. Rivas, J. R. Sambles, W. L. Barnes, and E. Hendry. Surface plasmon mediated transmission of subwavelength slits at thz frequencies. *Physical Review B*, 77(11):113411, 2008.

[86] J. Isberg, J. Hammersberg, E. Johansson, T. Wikstrom, D. J. Twitchen, A. J. Whitehead, S. E. Coe, and G. A. Scarsbrook. High carrier mobility in single-crystal plasma-deposited diamond. *Science*, 297(5587):1670–1672, 2002.

[87] F. Jelezko and J. Wrachtrup. Single defect centres in diamond: A review. *Physica Status Solidi a-Applications and Materials Science*, 203(13):3207–3225, 2006.

[88] T. I. Jeon and D. Grischkowsky. Nature of conduction in doped silicon. *Physical Review Letters*, 78(6):1106–1109, 1997.

[89] T. I. Jeon and D. Grischkowsky. Observation of a cole-davidson type complex conductivity in the limit of very low carrier densities in doped silicon. *Applied Physics Letters*, 72(18):2259–2261, 1998.

[90] P. U. Jepsen, D. G. Cooke, and M. Koch. Terahertz spectroscopy and imaging - modern techniques and applications. *Laser and Photonics Reviews*, 5(1):124–166, 2011.

[91] P. U. Jepsen, W. Schairer, I. H. Libon, U. Lemmer, N. E. Hecker, M. Birkholz, K. Lips, and M. Schall. Ultrafast carrier trapping in microcrystalline silicon observed in optical pump-terahertz probe measurements. *Applied Physics Letters*, 79(9):1291–1293, 2001.

[92] Z. P. Jiang, M. Li, and X. C. Zhang. Dielectric constant measurement of thin films by differential time-domain spectroscopy. *Applied Physics Letters*, 76(22):3221–3223, 2000.

[93] Z. P. Jiang and X. C. Zhang. Electro-optic measurement of thz field pulses with a chirped optical beam. *Applied Physics Letters*, 72(16):1945–1947, 1998.

[94] Zhiping Jiang, F. G. Sun, Q. Chen, and X. C. Zhang. Electro-optic sampling near zero optical transmission point. *Applied Physics Letters*, 74(9):1191–1193, 1999.

[95] M. Jivanescu, A. Stesmans, R. Kurstjens, and F. Dross. Interface nature of oxidized single-crystal arrays of etched si nanowires on (100)si. *Applied Physics Letters*, 100(8):082110–4, 2012.

[96] C. J. Johnson, G. H. Sherman, and R. Weil. Far infrared measurement of the dielectric properties of gaas and cdte at 300 k and 8 k. *Appl. Opt.*, 8(8):1667–1671, 1969.

[97] Marcus Jones, Shun S. Lo, and Gregory D. Scholes. Signatures of exciton dynamics and carrier trapping in the time-resolved photoluminescence of colloidal cdse nanocrystals. *Journal of Physical Chemistry C*, 113(43):18632–18642, 2009.

[98] R. Jones and P. R. Briddon. *Identification of defects in semiconductors, Vol. 51A of Semiconductors and Semimetals*, volume 51A. Academic Press, Boston, 1998.

[99] Yutaka Kadoya and Kazuhiko Hirakawa. *Terahertz Radiation from Bulk and Quantum Semiconductor Structures*, volume 97 of *Topics in Applied Physics*, pages 117–156. Springer Berlin / Heidelberg, 2005.

[100] R. A. Kaindl, M. A. Carnahan, D. Hagele, R. Lovenich, and D. S. Chemla. Ultrafast terahertz probes of transient conducting and insulating phases in an electron-hole gas. *Nature*, 423(6941):734–738, 2003.

[101] R. A. Kaindl, F. Eickemeyer, M. Woerner, and T. Elsaesser. Broadband phase-matched difference frequency mixing of femtosecond pulses in gase: Experiment and theory. *Applied Physics Letters*, 75(8):1060–1062, 1999.

[102] R. A. Kaindl, D. Hagele, M. A. Carnahan, and D. S. Chemla. Transient terahertz spectroscopy of excitons and unbound carriers in quasi-two-dimensional electron-hole gases. *Physical Review B*, 79(4):045320, 2009.

[103] R. A. Kaindl, R. Huber, B. A. Schmid, M. A. Carnahan, D. Hagele, and D. S. Chemla. Ultrafast thz spectroscopy of correlated electrons: from excitons to cooper pairs. *Physica Status Solidi B-Basic Solid State Physics*, 243(10):2414–2422, 2006.

[104] Ayan Kar, Prashanth C. Upadhya, Shadi A. Dayeh, S. Tom Picraux, Antoinette J. Taylor, and Rohit P. Prasankumar. Probing ultrafast carrier dynamics in silicon nanowires. *Ieee Journal of Selected Topics in Quantum Electronics*, 17(4):889–895, 2011.

[105] N. Karpowicz, X. F. Lu, and X. C. Zhang. Terahertz gas photonics. *Journal of Modern Optics*, 56(10):1137–1150, 2009.

[106] I. Katayama, R. Akai, M. Bito, H. Shimosato, K. Miyamoto, H. Ito, and M. Ashida. Ultrabroadband terahertz generation using 4-n,n-dimethylamino-4 ′-n ′-methyl-stilbazolium tosylate single crystals. *Applied Physics Letters*, 97(2):021105, 2010.

[107] N. Katzenellenbogen and D. Grischkowsky. Electrical characterization to 4 thz of n-type and p-type gaas using thz time-domain spectroscopy. *Applied Physics Letters*, 61(7):840–842, 1992.

[108] Y. Kawada, T. Yasuda, H. Takahashi, and S. I. Aoshima. Real-time measurement of temporal waveforms of a terahertz pulse using a probe pulse with a tilted pulse front. *Optics Letters*, 33(2):180–182, 2008.

[109] B. M. Kayes, H. A. Atwater, and N. S. Lewis. Comparison of the device physics principles of planar and radial p-n junction nanorod solar cells. *Journal of Applied Physics*, 97(11), 2005.

[110] Michael D. Kelzenberg, Shannon W. Boettcher, Jan A. Petykiewicz, Daniel B. Turner-Evans, Morgan C. Putnam, Emily L. Warren, Joshua M. Spurgeon, Ryan M. Briggs, Nathan S. Lewis, and Harry A. Atwater. Enhanced absorption and carrier collection in si wire arrays for photovoltaic applications. *Nature Materials*, 9(3):239–244, 2010.

[111] D. S. Kim and D. S. Citrin. Coulomb and radiation screening in photoconductive terahertz sources. *Applied Physics Letters*, 88(16):161117, 2006.

[112] K. Y. Kim, A. J. Taylor, J. H. Glownia, and G. Rodriguez. Coherent control of terahertz supercontinuum generation in ultrafast laser-gas interactions. *Nature Photonics*, 2(10):605–609, 2008.

[113] K. Y. Kim, B. Yellampalle, A. J. Taylor, G. Rodriguez, and J. H. Glownia. Single-shot terahertz pulse characterization via two-dimensional electro-optic imaging with dual echelons. *Optics Letters*, 32(14):1968–1970, 2007.

[114] J. T. Kindt and C. A. Schmuttenmaer. Theory for determination of the low-frequency time-dependent response function in liquids using time-resolved terahertz pulse spectroscopy. *Journal of Chemical Physics*, 110(17):8589–8596, 1999.

[115] M. Kira, W. Hoyer, and S. W. Koch. Terahertz signatures of the exciton formation dynamics in non-resonantly excited semiconductors. *Solid State Communications*, 129(11):733–736, 2004.

[116] M. Kira, W. Hoyer, T. Stroucken, and S. W. Koch. Exciton formation in semiconductors and the influence of a photonic environment. *Physical Review Letters*, 8717(17):176401, 2001.

[117] M. Kira, F. Jahnke, and S. W. Koch. Microscopic theory of excitonic signatures in semiconductor photoluminescence. *Physical Review Letters*, 81(15):3263–3266, 1998.

[118] C. Kittel. *Introduction to Solid State Physics*. Wiley, 1995. Page 276.

[119] V. I. Klimov. Spectral and dynamical properties of multilexcitons in semiconductor nanocrystals. *Annual Review of Physical Chemistry*, 58:635–673, 2007.

[120] C.F. Klingshirn. *Semiconductor Optics*. Springer, 2006.

[121] E. Knoesel, M. Bonn, J. Shan, F. Wang, and T. F. Heinz. Conductivity of solvated electrons in hexane investigated with terahertz time-domain spectroscopy. *Journal of Chemical Physics*, 121(1):394–404, 2004.

[122] S. W. Koch, M. Kira, G. Khitrova, and H. M. Gibbs. Semiconductor excitons in new light. *Nature Materials*, 5(7):523–531, 2006.

[123] S. Koizumi and M. Suzuki. n-type doping of diamond. *Physica Status Solidi a-Applications and Materials Science*, 203(13):3358–3366, 2006.

[124] R. Konenkamp, G. Priebe, and B. Pietzak. Carrier mobilities and influence of oxygen in c-60 films. *Physical Review B*, 60(16):11804–11808, 1999.

[125] E. Kretschmann. The angular dependence and the polarisation of light emitted by surface plasmons on metals due to roughness. *Optics Communications*, 5(5):331–336, 1972.

[126] A. Krotkus and J. L. Coutaz. Non-stoichiometric semiconductor materials for terahertz optoelectronics applications. *Semiconductor Science and Technology*, 20(7):S142–S150, 2005.

[127] R. Kubo. Statistical-mechanical theory of irreversible processes. i. general theory and simple applications to magnetic and conduction problems. *J. Phys. Soc. Jpn.*, 12:570–586, 1957.

[128] R. Kurstjens, I. Vos, F. Dross, J. Poortmans, and R. Mertens. Thermal oxidation of a densely packed array of vertical si nanowires. *Journal of the Electrochemical Society*, 159(3):H300–H306, 2012.

[129] H. A. V. Laarhoven, C. F. J. Flipse, M. Koeberg, M. Bonn, E. Hendry, G. Orlandi, O. D. Jurchescu, T. T. M. Palstra, and A. Troisi. On the mechanism of charge transport in pentacene. *Journal of Chemical Physics*, 129(4):044704, 2008.

[130] P.T. Landsberg. *Recombination in semiconductors*. Cambridge University Press, 2003.

[131] D. V. Lang and C. H. Henry. Nonradiative recombination at deep levels in gaas and gap by lattice-relaxation multiphonon emission. *Physical Review Letters*, 35(22):1525, 1975.

[132] S. C. Lawson, D. Fisher, D. C. Hunt, and M. E. Newton. On the existence of positively charged single-substitutional nitrogen in diamond. *Journal of Physics-Condensed Matter*, 10(27):6171–6180, 1998.

[133] C. H. Lee, G. Yu, D. Moses, and A. J. Heeger. Picosecond transient photoconductivity in poly(p-phenylenevinylene). *Physical Review B*, 49(4):2396–2407, 1994.

[134] YS Lee. *Principles of Terahertz Science and Technology (Lecture Notes in Physics)*. Springer, 2009.

[135] D. A. Liberman. Slater transition-state band-structure calculations. *Physical Review B*, 62(11):6851–6853, 2000.

[136] X. F. Lu, N. Karpowicz, Y. Q. Chen, and X. C. Zhang. Systematic study of broadband terahertz gas sensor. *Applied Physics Letters*, 93(26):261106, 2008.

[137] T. Malinauskas, K. Jarasiunas, E. Ivakin, V. Ralchenko, A. Gontar, and S. Ivakhnenko. Optical evaluation of carrier lifetime and diffusion length in synthetic diamonds. *Diamond and Related Materials*, 17(7-10):1212–1215, 2008.

[138] T. Malinauskas, K. Jarasiunas, E. Ivakin, N. Tranchant, and M. Nesladek. Determination of carrier diffusion coefficient and lifetime in single crystalline cvd diamonds by light-induced transient grating technique. *Physica Status Solidi a-Applications and Materials Science*, 207(9):2058–2063, 2010.

[139] D. Mayou. Generalized drude formula for the optical conductivity of quasicrystals. *Physical Review Letters*, 85(6):1290–1293, 2000.

[140] K. A. McIntosh, E. R. Brown, K. B. Nichols, O. B. McMahon, W. F. DiNatale, and T. M. Lyszczarz. Terahertz photomixing with diode lasers in low-temperature-grown gaas. *Applied Physics Letters*, 67(26):3844–3846, 1995.

[141] S. P. Mickan, K. S. Lee, T. M. Lu, J. Munch, D. Abbott, and X. C. Zhang. Double modulated differential thz-tds for thin film dielectric characterization. *Microelectronics Journal*, 33(12):1033–1042, 2002.

[142] M. Mikulics, E. A. Michael, M. Marso, M. Lepsa, A. van der Hart, H. Luth, A. Dewald, S. Stancek, M. Mozolik, and P. Kordos. Traveling-wave photomixers fabricated on high energy nitrogen-ion-implanted gaas. *Applied Physics Letters*, 89(7):071103, 2006.

[143] Hendrik J. Monkhorst and James D. Pack. Special points for brillouin-zone integrations. *Physical Review B*, 13(12):5188, 1976.

[144] D. Moses, D. Comoretto, C. H. Lee, and A. J. Heeger. Fast transient "photoconductivity" in semiconducting polymers: Free carrier photocurrent or displacement current generated by electric-field-induced polarization of bound excitons? *Synthetic Metals*, 84(1-3):559–562, 1997.

[145] N. F. Mott. Conduction in glasses containing transition metal ions. *Journal of Non-Crystalline Solids*, 1(1):1–17, 1968.

[146] N. F. Mott. Conduction in non-crystalline materials – iii. localized states in a pseudogap and near extremities of conduction and valence bands. *Philosophical Magazine*, 19(160):835 – 852, 1969.

[147] H. H. Mueller and M. Schulz. Individual interface traps at the si-sio2 interface. *Journal of Materials Science-Materials in Electronics*, 6(2):65–74, 1995.

[148] H. H. Mueller, D. Worle, and M. Schulz. Evaluation of the coulomb energy for single-electron interface trapping in sub-mu-m metal-oxide-semiconductor field-effect transistors. *Journal of Applied Physics*, 75(6):2970–2979, 1994.

[149] B. N. Murdin. Far-infrared free-electron lasers and their applications. *Contemporary Physics*, 50(2):391–406, 2009.

[150] W. A. Murray and W. L. Barnes. Plasmonic materials. *Advanced Materials*, 19(22):3771–3782, 2007.

[151] A. Nahata, D. H. Auston, T. F. Heinz, and C. J. Wu. Coherent detection of freely propagating terahertz radiation by electro-optic sampling. *Applied Physics Letters*, 68(2):150–152, 1996.

[152] A. Nahata, A. S. Weling, and T. F. Heinz. A wideband coherent terahertz spectroscopy system using optical rectification and electro-optic sampling. *Applied Physics Letters*, 69(16):2321–2323, 1996.

[153] F. Nava, C. Canali, C. Jacoboni, L. Reggiani, and S. F. Kozlov. Electron effective masses and lattice scattering in natural diamond. *Solid State Communications*, 33(4):475–477, 1980.

[154] H. Nemec, F. Kadlec, C. Kadlec, P. Kuzel, and P. Jungwirth. Ultrafast far-infrared dynamics probed by terahertz pulses: A frequency-domain approach. ii. applications. *Journal Of Chemical Physics*, 122(10), 2005.

[155] H. Nemec, F. Kadlec, and P. Kuzel. Methodology of an optical pump-terahertz probe experiment: An analytical frequency-domain approach. *Journal of Chemical Physics*, 117(18):8454–8466, 2002.

[156] H. Nemec, F. Kadlec, S. Surendran, P. Kuzel, and P. Jungwirth. Ultrafast far-infrared dynamics probed by terahertz pulses: A frequency domain approach. i. model systems. *Journal Of Chemical Physics*, 122(10):104503, 2005.

[157] H. Nemec, P. Kuzel, and V. Sundstrom. Far-infrared response of free charge carriers localized in semiconductor nanoparticles. *Physical Review B*, 79(11), 2009.

[158] H. Nemec, J. Rochford, O. Taratula, E. Galoppini, P. Kuzel, T. Polivka, A. Yartsev, and V. Sundstrom. Influence of the electron-cation interaction on electron mobility in dye-sensitized zno and tio2 nanocrystals: A study using ultrafast terahertz spectroscopy. *Physical Review Letters*, 104(19):197401, 2010.

[159] Hynek Nemec, Petr Kuzel, and Villy Sundstrom. Charge transport in nanostructured materials for solar energy conversion studied by time-resolved terahertz spectroscopy. *Journal of Photochemistry and Photobiology A: Chemistry*, 215(2-3):123–139, 2010.

[160] H. K. Nienhuys and V. Sundstrom. Influence of plasmons on terahertz conductivity measurements. *Applied Physics Letters*, 87(1):012101, 2005.

[161] H. K. Nienhuys and V. Sundstrom. Intrinsic complications in the analysis of optical-pump, terahertz probe experiments. *Physical Review B*, 71(23):235110, 2005.

[162] B. Oregan and M. Gratzel. A low-cost, high-efficiency solar-cell based on dye-sensitized colloidal tio2 films. *Nature*, 353(6346):737–740, 1991.

[163] J. Orenstein and M. A. Kastner. Thermalization and recombination in amorphous semiconductors. *Solid State Communications*, 40(1):85–89, 1981.

[164] V. Pacebutas, A. Biciunas, S. Balakauskas, A. Krotkus, G. Andriukaitis, D. Lorenc, A. Pugzlys, and A. Baltuska. Terahertz time-domain-spectroscopy system based on femtosecond yb:fiber laser and gabias photoconducting components. *Applied Physics Letters*, 97(3):031111, 2010.

[165] P. Parkinson, H. J. Joyce, Q. Gao, H. H. Tan, X. Zhang, J. Zou, C. Jagadish, L. M. Herz, and M. B. Johnston. Carrier lifetime and mobility enhancement in nearly defect-free core-shell nanowires measured using time-resolved terahertz spectroscopy. *Nano Letters*, 9(9):3349–3353, 2009.

[166] P. Parkinson, J. Lloyd-Hughes, Q. Gao, H. H. Tan, C. Jagadish, M. B. Johnston, and L. M. Herz. Transient terahertz conductivity of gaas nanowires. *Nano Letters*, 7(7):2162–2165, 2007.

[167] J. P. Perdew and Y. Wang. Accurate and simple analytic representation of the electron-gas correlation-energy. *Physical Review B*, 45(23):13244–13249, 1992.

[168] John P. Perdew, Kieron Burke, and Matthias Ernzerhof. Generalized gradient approximation made simple. *Physical Review Letters*, 77(18):3865, 1996.

[169] J. J. H. Pijpers, M. T. W. Milder, C. Delerue, and M. Bonn. (multi)exciton dynamics and exciton polarizability in colloidal inas quantum dots. *Journal of Physical Chemistry C*, 114(14):6318–6324, 2010.

[170] J. J. H. Pijpers, R. Ulbricht, K. J. Tielrooij, A. Osherov, Y. Golan, C. Delerue, G. Allan, and M. Bonn. Assessment of carrier-multiplication efficiency in bulk pbse and pbs. *Nature Physics*, 5(11):811–814, 2009.

[171] R. P. Prasankumar, P. C. Upadhya, and A. J. Taylor. Ultrafast carrier dynamics in semiconductor nanowires. *Physica Status Solidi B-Basic Solid State Physics*, 246(9):1973–1995, 2009.

[172] M. J. Rayson and P. R. Briddon. Rapid iterative method for electronic-structure eigenproblems using localised basis functions. *Computer Physics Communications*, 178(2):128–134, 2008.

[173] Alfred G. Redfield. Electronic hall effect in diamond. *Physical Review*, 94(3):526, 1954.

[174] K. Reimann. Table-top sources of ultrashort thz pulses. *Reports On Progress In Physics*, 70(10):1597–1632, 2007.

[175] Sampsa Riikonen, Isabel Romero, and F. J. GarcÃ■a de Abajo. Plasmon tunability in metallodielectric metamaterials. *Physical Review B*, 71(23):235104, 2005.

[176] R. H. Ritchie. Plasma losses by fast electrons in thin films. *Physical Review*, 106(5):874, 1957.

[177] K Sakai. *Terahertz Optoelectronics*. Springer-Verlag, Berlin, 2005.

[178] G. Scalari, C. Walther, M. Fischer, R. Terazzi, H. Beere, D. Ritchie, and J. Faist. Thz and sub-thz quantum cascade lasers. *Laser and Photonics Reviews*, 3(1-2):45–66, 2009.

[179] Harvey Scher and Elliott W. Montroll. Anomalous transit-time dispersion in amorphous solids. *Physical Review B*, 12(6):2455, 1975.

[180] C. A. Schmuttenmaer. Exploring dynamics in the far-infrared with terahertz spectroscopy. *Chemical Reviews*, 104(4):1759–1779, 2004.

[181] A. Sell, A. Leitenstorfer, and R. Huber. Phase-locked generation and field-resolved detection of widely tunable terahertz pulses with amplitudes exceeding 100 mv/cm. *Optics Letters*, 33(23):2767–2769, 2008.

[182] A. Sell, R. Scheu, A. Leitenstorfer, and R. Huber. Field-resolved detection of phase-locked infrared transients from a compact er:fiber system tunable between 55 and 107 thz. *Applied Physics Letters*, 93(25):251107, 2008.

[183] M. A. Seo, S. A. Dayeh, P. C. Upadhya, J. A. Martinez, B. S. Swartzentruber, S. T. Picraux, A. J. Taylor, and R. P. Prasankumar. Understanding ultrafast carrier dynamics in single quasi-one-dimensional si nanowires. *Applied Physics Letters*, 100(7), 2012.

[184] J. Shan and T. F. Heinz. *Terahertz radiation from semiconductors*, volume 92 of *Topics in Applied Physics*, pages 1–56. Springer Berlin / Heidelberg, 2004.

[185] J. Shan, F. Wang, E. Knoesel, M. Bonn, and T. F. Heinz. Measurement of the frequency-dependent conductivity in sapphire. *Physical Review Letters*, 90(24), 2003.

[186] Jie Shan, Aniruddha S. Weling, Ernst Knoesel, Ludwig Bartels, Mischa Bonn, Ajay Nahata, Georg A. Reider, and Tony F. Heinz. Single-shot measurement of terahertz electromagnetic pulses by use of electro-optic sampling. *Opt. Lett.*, 25(6):426–428, 2000.

[187] Y. C. Shen, P. C. Upadhya, H. E. Beere, E. H. Linfield, A. G. Davies, I. S. Gregory, C. Baker, W. R. Tribe, and M. J. Evans. Generation and detection,of ultrabroadband terahertz radiation using photoconductive emitters and receivers. *Applied Physics Letters*, 85(2):164–166, 2004.

[188] Abbott Smith and David Dutton. Behavior of lead sulfide photocells in the ultraviolet. *J. Opt. Soc. Am.*, 48(12):1007–1009, 1958.

[189] N. V. Smith. Classical generalization of the drude formula for the optical conductivity. *Physical Review B*, 6415(15):155106, 2001.

[190] P. R. Smith, D. H. Auston, and M. C. Nuss. Subpicosecond photoconducting dipole antennas. *Ieee Journal of Quantum Electronics*, 24(2):255–260, 1988.

[191] Julie A. Smyder and Todd D. Krauss. Coming attractions for semiconductor quantum dots. *Materials Today*, 14(9):382–387, 2011.

[192] S. A. Solin and A. K. Ramdas. Raman spectrum of diamond. *Physical Review B*, 1(4):1687–, 1970.

[193] Jonathan E. Spanier and Irving P. Herman. Use of hybrid phenomenological and statistical effective-medium theories of dielectric functions to model the infrared reflectance of porous sic films. *Physical Review B*, 61(15):10437, 2000.

[194] Sanjay K. Srivastava, Dinesh Kumar, P. K. Singh, M. Kar, Vikram Kumar, and M. Husain. Excellent antireflection properties of vertical silicon nanowire arrays. *Solar Energy Materials and Solar Cells*, 94(9):1506–1511, 2010.

[195] J. H. Strait, P. A. George, M. Levendorf, M. Blood-Forsythe, F. Rana, and J. Park. Measurements of the carrier dynamics and terahertz response of oriented germanium nanowires using optical-pump terahertz-probe spectroscopy. *Nano Letters*, 9(8):2967–2972, 2009.

[196] D. Stroud. Generalized effective-medium approach to the conductivity of an inhomogeneous material. *Physical Review B*, 12(8):3368, 1975.

[197] M. Suzuki, H. Yoshida, N. Sakuma, T. Ono, T. Sakai, M. Ogura, H. Okushi, and S. Koizumi. Electrical properties of b-related acceptor in b-doped homoepitaxial diamond layers grown by microwave plasma cvd. *Diamond and Related Materials*, 13(1):198–202, 2004.

[198] T. Suzuki and R. Shimano. Time-resolved formation of excitons and electron-hole droplets in si studied using terahertz spectroscopy. *Physical Review Letters*, 103(5):057401, 2009.

[199] M. D. Thomson, M. Kress, T. Loffler, and H. G. Roskos. Broadband thz emission from gas plasmas induced by femtosecond optical pulses: From fundamentals to applications. *Laser and Photonics Reviews*, 1(4):349–368, 2007.

[200] B. Tian, X. Zheng, T. J. Kempa, Y. Fang, N. Yu, G. Yu, J. Huang, and C. M. Lieber. Coaxial silicon nanowires as solar cells and nanoelectronic power sources. *Nature*, 449(7164):885–9, 2007.

[201] N. Tranchant, M. Nesladek, D. Tromson, Z. Remes, A. Bogdan, and P. Bergonzo. Time of flight study of high performance cvd diamond detector devices. *Physica Status Solidi a-Applications and Materials Science*, 204(9):3023–3029, 2007.

[202] K. Tsukioka and H. Okushi. Hall mobility and scattering mechanism of holes in boron-doped homoepitaxial chemical vapor deposition diamond thin films. *Japanese Journal of Applied Physics Part 1-Regular Papers Brief Communications and Review Papers*, 45(11):8571–8577, 2006.

[203] G. M. Turner, M. C. Beard, and C. A. Schmuttenmaer. Carrier localization and cooling in dye-sensitized nanocrystalline titanium dioxide. *Journal Of Physical Chemistry B*, 106(45):11716–11719, 2002.

[204] R. Ulbricht, S. T. van der Post, J. P. Goss, P. R. Briddon, R. Jones, R. U. A. Khan, and M. Bonn. Single substitutional nitrogen defects revealed as electron acceptor states in diamond using ultrafast spectroscopy. *Physical Review B*, 84(16), 2011.

[205] Ronald Ulbricht, Euan Hendry, Jie Shan, Tony F. Heinz, and Mischa Bonn. Carrier dynamics in semiconductors studied with time-resolved terahertz spectroscopy. *Reviews of Modern Physics*, 83(2):543, 2011.

[206] M. Vanexter and D. Grischkowsky. Carrier dynamics of electrons and holes in moderately doped silicon. *Physical Review B*, 41(17):12140–12149, 1990.

[207] F. Wang, G. Dukovic, L. E. Brus, and T. F. Heinz. The optical resonances in carbon nanotubes arise from excitons. *Science*, 308(5723):838–841, 2005.

[208] F. Wang, J. Shan, M. A. Islam, I. P. Herman, M. Bonn, and T. F. Heinz. Exciton polarizability in semiconductor nanocrystals. *Nature Materials*, 5(11):861–864, 2006.

[209] G. P. Williams. High-power terahertz synchrotron sources. *Philosophical Transactions of the Royal Society a-Mathematical Physical and Engineering Sciences*, 362(1815):403–413, 2004.

[210] G. P. Williams. Filling the thz gap - high power sources and applications. *Reports on Progress in Physics*, 69(2):301–326, 2006.

[211] U. Woggon. *Optical Properties of Semiconductor Quantum Dots*. Springer, 1997.

[212] DJ Woolard, WR Loerop, and MS Shur. *Terahertz Sensing Technology: Vol. 1 (Electronic devices and advanced systems technology)*. World Scientific, New Jersey, 2003.

[213] C. J. H. Wort and R. S. Balmer. Diamond as an electronic material. *Materials Today*, 11(1-2):22–28, 2008.

[214] Q. Wu and X. C. Zhang. Free-space electro-optic sampling of terahertz beams. *Applied Physics Letters*, 67(24):3523–3525, 1995.

[215] Q. Wu and X. C. Zhang. 7 terahertz broadband gap electro-optic sensor. *Applied Physics Letters*, 70(14):1784–1786, 1997.

[216] S. F. Wuister, C. D. M. Donega, and A. Meijerink. Luminescence temperature antiquenching of water-soluble cdte quantum dots: Role of the solvent. *Journal of the American Chemical Society*, 126(33):10397–10402, 2004.

[217] K. Wynne and J. J. Carey. An integrated description of terahertz generation through optical rectification, charge transfer, and current surge. *Optics Communications*, 256(4-6):400–413, 2005.

[218] X. Xie, J. M. Dai, and X. C. Zhang. Coherent control of thz wave generation in ambient air. *Physical Review Letters*, 96(7):075005, 2006.

[219] B. Yellampalle, K. Y. Kim, G. Rodriguez, J. H. Glownia, and A. J. Taylor. Algorithm for high-resolution single-shot thz measurement using in-line spectral interferometry with chirped pulses. *Applied Physics Letters*, 87(21):211109, 2005.

[220] Heayoung P. Yoon, Yu A. Yuwen, Chito E. Kendrick, Greg D. Barber, Nikolas J. Podraza, Joan M. Redwing, Thomas E. Mallouk, Christopher R. Wronski, and Theresa S. Mayer. Enhanced conversion efficiencies for pillar array solar cells fabricated from crystalline silicon with short minority carrier diffusion lengths. *Applied Physics Letters*, 96(21), 2010.

[221] D. You, R. R. Jones, P. H. Bucksbaum, and D. R. Dykaar. Generation of high-power sub-single-cycle 500-fs electromagnetic pulses. *Optics Letters*, 18(4):290–292, 1993.

[222] W. W. Yu, Y. A. Wang, and X. G. Peng. Formation and stability of size-, shape-, and structure-controlled cdte nanocrystals: Ligand effects on monomers and nanocrystals. *Chemistry of Materials*, 15(22):4300–4308, 2003.

[223] J. H. Zheng, H. S. Tan, and S. C. Ng. Theory of nonradiative capture of carriers by multiphonon processes for deep centers in semiconductors. *Journal of Physics-Condensed Matter*, 6(9):1695–1706, 1994.

[224] X. M. Zheng, C. V. McLaughlin, P. Cunningham, and L. M. Hayden. Organic broadband terahertz sources and sensors. *Journal of Nanoelectronics and Optoelectronics*, 2(1):58–76, 2007.

[225] Jing Zhuge, Liangliang Zhang, Runsheng Wang, Ru Huang, Dong-Won Kim, Donggun Park, and Yangyuan Wang. Random telegraph signal noise in gate-all-around silicon nanowire transistors featuring coulomb-blockade characteristics. *Applied Physics Letters*, 94(8):083503–3, 2009.

Summary

Charge carriers in semiconductors provide the basis for a variety of important electronic devices, such as computers, semiconductor lasers and light emitting devices. The continuing wish to reduce the physical size of next-generation electronics requires increasingly smaller building blocks. Nanostructures with sizes well below 100 nm, such as semiconductor nanocrystals and nanowires, can provide these building blocks. Charge carriers can have very different properties in semiconductors and in semiconductor nanostructures, depending on morphology, size, temperature and material properties, such as the crystal structure, bandgap, dielectric function and electron-phonon coupling strength.

The common characteristic of charge carriers is that they all exhibit a characteristic response in the low-frequency range of the electromagnetic spectrum. Exciton binding energies - and exciton transitions, for both bulk and nanostructured materials, are typically in the meV range and are optically active. The response of mobile carriers is dictated by the interaction of carriers with their environment, leading to randomization of the carrier momentum that typically occurs on (sub-)picosecond time scales, giving rise to dispersion in the dielectric response on meV-energy scales. Restoring forces that act on charge carriers, such as potential barriers or space charge fields, can further have an influence on the low-energy dispersion, as well as quantum phenomena like the appearance of discrete energy levels following Bohr's hydrogen model in the case of exciton formation or the particle-in-a-box problem for quantum confinement. The ability to probe charge carriers in the meV energy range or, equivalently, terahertz (THz) frequency range, provides a way to achieve a detailed characterization of charge carriers through their distinct spectral signatures in the terahertz range.

THz time-domain spectroscopy (THz TDS) constitutes an all-optical and thus contact-free probe of the frequency-dependent terahertz conductivity. This technique makes use of sub-picosecond pulses of freely propagating electromagnetic radiation in the terahertz range. THz radiation (1 THz = 10^{12} Hz) is characterized by low photon energies (33.3 cm^{-1} or 4.2 meV at 1 THz) and sub-mm wavelengths (300 μm for 1 THz in vacuum). THz pulses are readily generated by frequency down-conversion of femtosecond optical laser pulses to the THz range and detected coherently in the time-domain. By using a femtosecond pump pulse to generate charge carriers (for instance through interband excitation or defect excitation), time-resolved experiments are possible, allowing to monitor carrier equilibration dynamics, e.g. carrier recombination processes, with sub-picosecond time-resolution.

The topics treated in this thesis cover phenomena in bulk semiconductors and semiconductor nanostructures related to carrier trapping and diffusion, and electronic quantum confinement, which were studied using time-resolved THz TDS.

The first chapter is an introduction to THz TDS, covering experimental techniques, analytical methods and an overview of typical THz responses. The work presented in the second chapter is an investigation of the trapping dynamics of photoexcited electrons in nitrogen-doped synthetic diamond. Synthetic diamond is a promising candidate for electronic devices where a bandgap much larger than silicon (~ five times) or other properties (e.g. mechanical and dielectric strength) are needed. Single substitutional nitrogen, which is the most common impurity in diamond, creates localized electron-donor states in the electronic bandgap. It was found that after excitation of electrons from nitrogen defects into the conduction band, the electron mobility is dominated by defect scattering, and recombination takes place on picosecond timescales. The dependence of the electron recombination time on defect concentration and photoexcited electron density suggested that most electrons relax into neutral nitrogen defects rather than their original states, which implies that negatively charged nitrogen defects are created during the relaxation process. The existence of such negatively charged nitrogen impurities was verified by complementary pump-probe spectroscopic measurements on similar timescales that probe in the infrared part of the spectrum. Nitrogen defects exhibit sharp IR-active resonances of their localized vibrational modes (LVM) in the mid-infrared, and their resonance frequency depends on the charge state. In these transient IR measurements, after all photoexcited electrons had recombined from the conduction band, a hitherto undiscovered resonance was identified at 1349 cm^{-1} and assigned to the LVM of negatively charged nitrogen defects, thus confirming their existence. Density-functional theory calculations on the LVM frequency of this defect were found to be in good agreement with the experimental value.

The work in chapter three is also an investigation of the influence of traps on charge transport, however this time on thin silicon nanowires. Thin nanowires of various materials have recently been proposed as building blocks of optoelectronic devices such as tandem solar cells. Due to their high surface-to-volume ratio, carrier traps in these quasi-one-dimensional systems are mainly located at the surface, where defects originating from strained silicon bonds create localized mid-gap states. In the experiment, a UV pump pulse creates mobile charge carriers in the nanowires which diffuse from the nanowires into the silicon substrate on picosecond timescales. This process is monitored by the THz probe pulse which is mainly sensitive to the charge carriers in the substrate. Below a critical photoexcited-charge density the diffusion process stalls and no carriers are injected into the bulk. This happens as a consequence of the capture of charge carriers into surface defects before they can reach the substrate. This critical charge density was found to be orders of magnitude larger than what would be generated by sunlight, casting doubts on the usability of thin nanowires for devices that rely on diffusive charge transport, at least with currently available passivation techniques for surface defects .

The final chapter is an investigation of how the THz conductivity of excitons in colloidal CdTe nanocrystals (quantum dots) depends on the nanocrystal size. Electronic quantum confinement effects in these zero-dimensional nanostructures modify the electronic structure, with the degree of modification strongly depending on the size of the nanocrystal. For small sizes of a few nanometers, the electronic bands that are typical for bulk semiconductors, and which are comprised of a continuum of states, are transformed into discrete, "atom-like" electronic states, with energy spacings in the tens to hundreds of meV. The THz conductivity in such systems is purely imaginary, i.e. devoid of absorption, due to the fact that none of the transitions are probed resonantly. When loosening the influence of quantum confinement by increasing the nanocrystal size, the electronic transition energies decrease. Already for quantum-dot radii larger than 5 nm but still smaller than the exciton Bohr radius (7 nm), real THz conductivity (absorption) emerges as a consequence of hole transitions resonantly move moving into the THz-probe window. The magnitude of the absorption is however significantly smaller than theoretically predicted by tight-binding calculations that compute the size-dependent electronic energy levels. The difference can qualitatively be explained by assuming the emergence of polaron states, i.e. strongly coupled hole-phonon states, that possess larger THz absorption larger than transitions between pure hole states.

Samenvatting

Ladingsdragers in halfgeleiders vormen de basis voor een verscheidenheid aan belangrijke elektronische applicaties. De voortdurende wens om de fysieke grootte van vernieuwende elektronica te verminderen vraagt om steeds kleinere elektronische bouwstenen. Nanostructuren met afmetingen ruim onder 100 nm zoals halfgeleidende nanokristallen en nanodraden kunnen in deze wens voorzien. Ladingsdragers kunnen uiteenlopende eigenschappen hebben in halfgeleiders en halfgeleidende nanostructuren, afhankelijk van morfologie, grootte, temperatuur en materiaaleigenschappen zoals de kristalstructuur, bandgap, diëlektrische functie en elektron-phonon koppelingsterkte.

De gemeenschappelijke eigenschap van ladingsdragers, die kunnen bestaan in elk van de hierboven beschreven vormen, is dat ze allen een duidelijk responssignaal geven in het laagfrequente gebied van het elektromagnetisch spectrum: exciton bindingsenergieën en exciton transities zijn, zowel voor bulk-en nanogestructureerde materialen, typisch in het bereik van meV en optisch actief. De respons van mobiele ladingsdragers wordt gedicteerd door drager-phonon interacties die leiden tot randomisatie van de impuls van de drager, typisch op (sub-) picoseconde tijdschaal. Dit geeft aanleiding tot spreiding in de diëlektrische respons op meV-energieschalen. Bijkomende hestellende krachten zoals potentiaalbarrières of ruimteladingen kunnen verder invloed hebben op de dispersie bij lage energieën, evenals kwantumverschijnselen zoals het verschijnen van discrete energieniveaus volgens het waterstofmodel van Bohr in het geval van excitonvorming, of het deeltje-in-een-doos probleem voor kwantumopsluiting. De mogelijkheid om ladingsdragers met meV energieën - ofwel in het terahertz frequentiebereik - te onderzoeken maakt het dus mogelijk ze gedetailleerd te karakteriseren aan de hand van de verschillende spectrale handtekeningen in het terahertz-bereik.

Teraherz tijd-domein spectroscopie (THz TDS) vormt een geheel optische en dus contactvrije onderzoeksmethode van de frequentieafhankelijke geleidbaarheid. Het maakt gebruik van sub-pico-seconde pulsen van zich vrij voortbewegende elektromagnetische straling in het terahertz-bereik. THz-straling (1 THz = 10 ^{12} Hz) wordt gekenmerkt door een lage fotonenergie (33,3 cm^{-1} of 4,2 meV op 1 THz) en submm golflengtes (300 $\mu\mathrm{m}$ voor 1 THz in vacuüm). THz-impulsen worden gemakkelijk opgewekt door frequentieconversie van femtoseconde optische pulsen en coherent gedetecteerd in het tijddomein. Door het gebruik van een femtoseconde pomppuls om ladingsdragers te genereren (door bijvoorbeeld interband-excitatie of defectexcitatie) worden tijdsopgeloste experimenten mogelijk. Zo kunnen de dynamische processen van de dragers, zoals dragerrecombinatie in processen als trapping, op sub-picoseconde tijdschaal worden vastgelegd.

Het in dit proefschrift samengevatte onderzoek behandelde de verschillende verschijnselen in bulk halfgeleiders en nanostructuren van halfgeleidend materiaal met betrekking tot trapping van ladingsdragers, diffusie en kwantumopsluiting met THz-

TDS.

Na een introductie van THz-TDS beschreef het tweede hoofdstuk de dynamiek van trapping van fotogeëxciteerde elektronen in stikstofgedoteerde synthetische diamant. Synthetische diamant is een veelbelovende kandidaat voor elektronische apparaten waar een bandgap veel groter dan silicium (~ vijf keer) of andere eigenschappen zoals mechanische en diëlektrische kracht zijn vereist. Enkelvoudig vervangende stikstof is de meest voorkomende onzuiverheid in diamant, en creëert gelokaliseerde donorniveaus in de bandgap. Na excitatie van elektronen van stikstof in de geleidingsband werd waargenomen dat de beweeglijkheid van de elektronen gedomineerd werd door verstrooiing vanaf de defecten; recombinatie vond plaats op een tijdschaal van picoseconden. De afhankelijkheid van de elektronrecombinatietijden op de defectconcentratie en de fotogeëxciteerde elektronendichtheid suggereert dat elektronen eerder relaxeren naar neutrale stikstofdefecten dan naar de oorspronkelijke staat, wat impliceert dat er negatief geladen defecten ontstaan. Het bestaan van dergelijke negatief geladen onzuiverheden van stikstof werd aangetoond door complementaire pomp-probe spectroscopie op dezelfde tijdschaal, maar nu in het infrarode deel van het spectrum: stikstofgebreken vertonen scherpe resonanties in het IR-gebied voortkomend uit hun lokale vibrationele toestanden (local vibrational modes, LVM) in het midden-infrarood, waarvan de resonantiefrequentie afhankelijk is van de lading. In deze tijdsopgeloste IR-metingen werd, nadat alle fotogeëxciteerde elektronen waren gerecombineerd vanuit de geleidingsband, een tot dan toe onontdekte piek vastgesteld op 1349 cm $^{-1}$ en toegewezen aan de LVM van negatief geladen stikstof-onzuiverheden, zodoende hun bestaan bevestigend. Dichtheid-functionele berekeningen van de LVM-frequentie van dit defect bleken in goede overeenstemming te zijn met de experimentele waarde.

Het daaropvolgende hoofdstuk behandelde ook de invloed van elektrische dragervallen op ladingstransport, maar dit keer toegepast op dunne silicium nanodraden. Dunne nanodraden, niet enkel die gemaakt van silicium, zijn onlangs voorgesteld als bouwstenen voor opto-elektronische apparaten, zoals tandem zonnecellen. Door hun hoge oppervlakte-volumeverhouding zijn dragervallen in deze quasi-eendimensionale systemen hoofdzakelijk aan het oppervlak gelegen, waar gebreken uit overspannen siliciumbindingen gelokaliseerde midgap-toestanden creëren. In dit experiment genereert een UV pomppuls mobiele ladingsdragers in de nanodraden die op hun beurt vanuit de nanodraden diffunderen naar het siliciumsubstraat op een tijdschaal van enkele picoseconden. Dit proces kan gevolgd worden door de THz probe-puls die hoofdzakelijk gevoelig is voor de ladingdragers in het substraat. Beneden een kritieke fotogeëxciteerde ladingsdichtheid stagneert het diffusieproces en worden er geen dragers meer geïnjecteerd in de bulk, wat een gevolg is van de opname van ladingsdragers in de gebreken aan het oppervlak van de draden voordat ze het substraat kunnen bereiken. De kritieke ladingsdichtheid bleek ordes van grootte groter te zijn dan die gegenereerd door zonlicht, wat de bruikbaarheid van nanodraden voor toepassingen die afhankelijk zijn van diffuus ladingstransport in twijfel trekt, in ieder geval met de huidig beschikbare passivatietechnieken voor oppervlaktedefecten.

Het laatste hoofdstuk onderzoekt de grootteafhankelijkheid van de THz geleiding van fotogegenereerde excitonen in colloïdale CdTe nanokristallen (kwantum punten). In tegenstelling tot in de hiervoor genoemde materialen wijzigen de effecten van elektronische kwantumopsluiting de elektronische structuur in deze nuldimensionale nanostructuren, waarbij de mate hiervan sterk afhankelijk is van de grootte van deze nanokristallen. Voor kleine afmetingen van een paar nanometer veranderen de elektronische banden die typisch zijn voor bulk halfgeleiders en die bestaan uit een continuüm van toestanden, in discrete, "atoom-achtige" elektronische toestanden, met energieverschillen in de tientallen tot honderden meV. De THz geleidbaarheid in dergelijke systemen is puur imaginair, dat wil zeggen zonder absorptie, aangezien geen van de overgangen resonant wordt geëxciteerd. Bij het verminderen van de invloed van de kwantumopsluiting door het vergroten van de nanokristallen nemen de energieverschillen van de elektronische overgangen af. Al voor afmetingen (R> 5nm) kleiner dan de exciton Bohr-straal (7nm), ontstaat er reële THz-geleding (absorptie) wanneer gat-overgangen resonant binnen het bereik van de THz probe worden geplaatst. De omvang van de absorptie is echter veel kleiner dan theoretisch wordt voorspeld in tight-binding modellen die de grootteafhankelijke elektronische niveaus berekenen. Deze afwijking kan kwalitatief worden verklaard door het onstaan van polarons, sterk gekoppelde gat-phonon toestanden, die een grotere THz absorptie bezitten.

Acknowledgements

When it was about time to write this last, yet generally considered most important, part of this booklet, I realized that the list of names that enter here is going to be long. During the course of my PhD we moved labs and offices twice, and many people have joined and left the group, albeit more of the former. When I started, the group consisted of perhaps eight people or so. Now that I am leaving it is probably five times more and growing. This is of course, for the most part, the merit of my promoter Herr Direktor Prof. Dr. Bonn, who I want to thank first. It was inspiring to see a 'young and promising' (quote himself ;) scientist making its way up to become a director of a Max-Planck Institute, and to experience the accompanying changes in the group dynamics. I certainly learned a lot from you, not only scientifically.

For the biggest part of my time in the group, Joep and Klaas were my 'comrades' on the THz front and I think the (self-proclaimed) socialist approach in terms of managing our little troop and supporting each other worked out pretty well. Highlight was of course the road trip along the West coast of the US. Even though not officially part of the THz group, I would also count Han-Kwang in it. I learned a great deal from our discussions when building the FAT DAVE setup and in certain ways you were probably my actual supervisor during the first year or so. Since then a number of people have been or still are part of the AMOLF THz crew, and it was great to work with them: Domenico, Søren, Enrique, Simon, Puck, Hai and Sen. May there always be a fresh sample on hand!

One intriguing part of my work was that every project not only involved a rather different aspect of semiconductor physics, but also different people to work with. The Utrecht group was there from the very start, providing the materials in the 'neverending' nanoparticle story, which pretty much lasted the whole course of my PhD. Thanks to Rolf, who provided the first samples, and Esther, who was always there when I suddenly needed a new batch of particles. Daniël and Celso, the many meetings we had, not only on the nanoparticle results, were always of great benefit. Also a big thanks to Christophe and Guy: your calculations have provided us with a great deal of understanding of our experimental results.

Thanks to Riz for introducing me to the world of 'synthetic bling-bling' and the diamond conferences we have been to. It was good that we stayed in contact after being your 'pupil' in Zurich. Thanks to Bob, Jon and Patrick for the DFT calculations. Rufi, it was great to have such well-defined samples to measure and our discussions were always very useful. Good luck with the final part of your PhD. For my understanding of the excitation light coupling in the nanowire measurements it was good to talk to Grzegorz and Jaime. Thanks!

Things can become rather technical when building optical setups, and I learned to appreciate the extensive support that AMOLF offers. On the electronic and software side I want to thank Henk, Duncan, Idsard and Marco for their support in building

the BB DAVE setup, Ilja for the design of the cryostat suspension and Wiebe for general computer assistance. It is sometimes amazing how many things can go wrong in the lab every day. On that account, it was great to have people around that helped fixing these ’issues’: Hinco, always offering a quick solution, and Ad and Ernst. Marc-Jan, thanks for the several ’tomorrow-would-be-good’ mechanical pieces you made.

A big part of getting the motivation to endure the PhD was the friendly and relaxed atmosphere in the Bonn group to which so many people have contributed. At the risk of forgetting some, here they are: long-term office-mate and flat-mate Dr. Ghosh, Sjors, Euan, Mattijs, Maria, Maaike, Johannes, Kramer, Susumu, Martin, Jens, Jan, Cho-Shuen, Steffen, Zhen, Gianluca, Katrin, James, Alex, Maarten and Megan. Special thanks to Rüben for the Dutch summary en de gezelligheid, hoor! Also thanks to Huib and his group, who were always somehow related to our group, and there particularly to Sietse and Ellen for their support with the transient-IR measurements. To the other people at AMOLF I was hanging out with, Ivana, Gijs, Jochen, Jean, and my Spiegelkwartier neighbors Bergin and Marko: it was great having you around. Thanks for the countless blurry night-outs. Thanks to Alberto for the awesome cover, and also to Yasmin Sibai for the nanoparticle image that was used in it. A big hug to Adriana for all the support during the sometimes hectic last bits of finishing this thesis. Und zu guter Letzt auch großen Dank an meine Familie zu Hause für die jahrelange Unterstützung.